Efficient frequency conversion towards ultrashort VUV pulses using coherent control and multi-photon resonances

Effiziente Frequenzkonversion von ultrakurzen Laserpulsen in den VUV Spektralbereich, unterstützt durch kohärente Kontrolle und Mehrphotonen-Resonanzen

Dissertation von Patric Ackermann, Januar 2019

TECHNISCHE UNIVERSITÄT DARMSTADT

Fachbereich Physik
Institut für Angewandte Physik
Nichtlineare Optik und Quantenoptik

Efficient frequency conversion towards ultrashort VUV pulses using coherent control and multi-photon resonances

Vom Fachbereich Physik
der Technischen Universität Darmstadt

zur Erlangung des Grades
eines Doktors der Naturwissenschaften
(Dr. rer. nat.)

genehmigte Dissertation
von M.Sc. Patric Ackermann
aus Darmstadt

Referent: Prof. Dr. Thomas Halfmann
Korreferent: Prof. Dr. Thomas Walther

Tag der Einreichung: 22. 1. 2019
Tag der Prüfung: 18. 2. 2019

Darmstadt 2019
D17

Ackermann, Patric: Efficient frequency conversion towards ultrashort VUV pulses using coherent control and multi-photon resonances
Darmstadt, Technische Universität Darmstadt.
Tag der mündlichen Prüfung: 18.02.2019
Jahr der Veröffentlichung der Dissertation auf TUprints: 2019

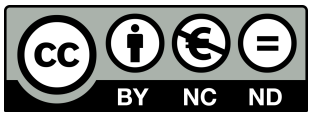

Die Veröffentlichung steht unter folgender Creative Commons Lizenz: Namensnennung - Keine kommerzielle Nutzung - Keine Bearbeitung 4.0 International
https://creativecommons.org/licenses/by-nc-nd/4.0/

Contents

Introduction **1**

1 Basic theory of harmonic generation in atomic gases **4**
1.1 Nonlinear wave equation 4
1.2 The atomic polarizability 7
1.2.1 The linear polarizability of noble gas atoms 7
1.2.2 The linear refractive index 8
1.2.3 The nonlinear polarizability of noble gas atoms 10
1.3 Phase matching 13
1.3.1 Phase matching for a plane wave 13
1.3.2 Phase matching of focused Gaussian beams 14
1.4 Dynamic shift of energy levels 16

2 Basic experimental setup and methodology **18**
2.1 Laser system 18
2.1.1 Laser pulse generation and manipulation 18
2.1.2 Amplification and spatial filtering 19
2.1.3 Pulse characterization 21
2.2 Conclusion 23

3 Resonantly enhanced higher harmonic generation in a jet of argon atoms **24**
3.1 Introduction 24
3.2 Coupling scheme and experimental setup 25
3.3 Experimental results 26
3.3.1 Intensity dependence of the resonance enhancement for FHG 27
3.3.2 Effect of the five-photon resonance on higher harmonics . . . 28
3.4 Conclusion 30

4 Coherent control of frequency up-conversion towards short vacuum-ultraviolet radiation pulses **31**
4.1 Introduction 31
4.2 Coupling scheme 32
4.2.1 Quantum interference in frequency conversion 33
4.2.2 Quantum interference in excited state population 34
4.2.3 Conditions for maximal control 34
4.3 Experimental Setup 35
4.4 Spectroscopy 39

4.5 Results . . . 41
4.5.1 Effect of resonance detuning . . . 42
4.5.2 Variation of interference traces with laser intensities . . . 43
4.5.3 Variation of interference traces with the laser wavelength . . . 45
4.5.4 Variation of the interference visibility with pulse delay . . . 47
4.5.5 Simultaneous interference measurements of excited state population and frequency conversion . . . 49
4.6 Conclusion . . . 50

5 Phase matched harmonic generation near a multi-photon resonance 51
5.1 Introduction . . . 51
5.2 Phase matched harmonic generation in a waveguide . . . 52
5.2.1 Propagation of light in hollow core waveguides . . . 52
5.2.2 Input coupling . . . 53
5.2.3 Harmonic generation inside the waveguide . . . 54
5.2.4 Calculation of the refractive index of argon . . . 56
5.2.5 Phase matching conditions for harmonic generation in argon 58
5.2.6 Numerical simulation . . . 60
5.3 Waveguide preparation and characterization . . . 60
5.4 Experimental setup . . . 62
5.5 Experimental results . . . 65
5.5.1 Pressure and intensity dependence of harmonic generation . 65
5.5.2 Contributions of higher waveguide modes to the harmonic yield . . . 66
5.5.3 Wavelength dependence of the harmonic yield . . . 70
5.5.4 Buffer gas admixture . . . 75
5.5.5 Comparison with gas jet and absolute efficiency . . . 75
5.6 Conclusion . . . 77

Conclusions and future work 78

Zusammenfassung 81

A Appendix 84
A.1 FROG signal deformations by the nonlinear medium . . . 84
A.2 Signal detection . . . 85
A.2.1 The vacuum monochromator . . . 85
A.2.2 The electron multiplier tube . . . 86
A.3 Model for harmonic generation in a waveguide . . . 88
A.3.1 Calculation of the nonlinear polarization . . . 88
A.3.2 Calculation of the nonlinear polarizability . . . 89
A.3.3 Harmonic generation from a single fundamental mode . . . 90
A.3.4 Pulse propagation effects . . . 91
A.3.5 Rarefied gas flow in a microchannel . . . 92

Bibliography 95

Publications and contribution to conferences **106**

Supervisions and contributions to teaching **107**

Acknowledgments **109**

Introduction

Coherent radiation in the vacuum ultraviolet (VUV) with a wavelength of ($10 \leq \lambda < 200$) nm and extreme ultraviolet (EUV ($10 \leq \lambda < 121$)nm [1]) is of high value for research as well as for technical applications. With photons of this spectral regime, photo-ionization and photo-dissociation of virtually all molecules can be achieved with a single quantum. Therefore spectroscopic investigations in this regime can unveil information about ionic excited levels and other photochemical processes [2–4]. Also at the high frequencies of EUV light, enough bandwidth to synthesize a coherent light pulse of attosecond duration is available, disclosing the capture of electron dynamics in atoms and molecules [5]. In a technical application of coherent EUV light, the high photon energy paired with the low diffraction limit at this small wavelengths can be used for high-resolution nanostructuring and surface analysis. This reduces the feature size not only in electronic chips [6] but also improves optical imaging by conventional and diffractive techniques [7, 8].

While incoherent EUV light can be directly generated by high voltage gas discharges and laser plasma, the direct generation of coherent light of high brilliance is only possible in specially designed free electron lasers [9]. Those facilities are capable of delivering micro-joules of pulse energy, but have the limitation of neither being small nor inexpensive. For most of the above noted applications however, a low amount of photons at moderate repetition rates in the Hertz or Kilohertz regime are sufficient. A more compact way to generate short or ultrashort coherent pulses of EUV light is nonlinear frequency up-conversion of modern "table-top" pulsed laser sources. The transmission cutoff wavelengths λ_c of nonlinear crystals ($\lambda_c \gtrsim 121$ nm [10, 11]) and window materials ($\lambda_c \approx 105$ nm, LiF) require interaction with a suitable nonlinear medium directly inside the evacuated experiment chamber. Here the EUV light is generated in gaseous media or metal vapor, at interfaces [12] or inside plasma plumes [13]. Most commonly a jet of noble gas atoms is used as a nonlinear medium. The gas is expanded through a nozzle inside the vacuum setup, where it is intersected by the intense laser beam. This particular approach is suitable to implement a small and easy to operate setup [9]. All noble gases exhibit a rather high ($W_I > 10$ eV) ionization threshold and a big energetic gap between the ground state and the first excited state of 8.3 eV (xenon) up to 19.8 eV (helium). This renders them transparent and leads to low dispersion for a wide spectrum of possible driving lasers, which is ideal for frequency up-conversion of (ultra-)short pulses. On the downside, the low achievable particle densities in the range of $N = 10^{17} - 10^{18}$ atoms per cubic centimeter limit the conversion efficiency to $\leq 10^{-5}$ in special cases, but often $\ll 10^{-6}$ [14].

To gain high conversion efficiencies, several approaches are possible: On the atomic scale, the source of the harmonic generation process in form of the nonlin-

ear polarizability can be drastically enhanced by tuning the driving laser frequency ω_1 to a n photon resonance with an atomic transition frequency ($\omega = n\omega_1$). Two photon and three photon resonances between the ground state and an excited state in noble gases have been exploited in harmonic generation of narrowband (ns) pulses towards the EUV regime [15]. This technique, especially in form of a two-photon resonant sum frequency mixing, up to date serves to generate tunable, narrowband EUV radiation down to 60 nm wavelength at efficiencies of $10^{-5} - 10^{-4}$ [16] at moderate fundamental intensity. With modern ultra-fast laser systems, at an intensity in excess of 10 TW/cm² the simultaneous generation of multiple higher ($n > 3$) harmonics of similar relative intensity is possible. An atomic n-photon resonance, in this case, could enhance the generation of harmonics of order n and higher. However, it is not obvious, that resonance-enhancement also works for (higher) harmonic generation, driven by such high intensity. The interaction of the atom with a strong electric field gives rise to AC Stark shifts of the excited states of the order of several 10 THz (i.e. up to 10% of the driving laser frequency). Additionally, the electric field perturbs the coulomb field of the atom quite drastically, possibly destroying any resonance effect in conversion processes. To still observe multi-photon resonances, operation in the regime of "multi-photon ionization" with a semi-classical tunneling time much larger than the inverse laser frequency ω_1 is required. In the opposite case "tunneling ionization" dominates the atomic response, suppressing resonance effects [17, 18]. Theoretical treatments unveil resonance enhancement of several harmonics in the multi-photon regime as well as in high harmonic generation [19–22]. Also, experimental evidence of resonance enhancement by a dynamically shifted resonance is reported, but mostly limited to a single harmonic or not clearly dedicated to a specific atomic resonance [23–26]. A second approach is to use a multi-color field, to actively control the generated nonlinear polarization inside the medium. When two indistinguishable (multi-photon) excitation pathways towards an intermediate level are driven simultaneously by multi-color laser fields, destructive and constructive interference for the excitation probability is possible, depending on the relative phase of the driving laser fields. The concept of "coherent control" has seen numerous demonstrations in physics and chemistry [27]. Yet, there are only a few proof of concept applications in control of optical frequency conversion processes [28–30]. These experiments with rather long, (ns) pulses exhibited a limited control strength $< 75\,\%$, even lower in the experiment with shorter (ps) pulses at high intensity of 30 TW/cm² ($< 25\,\%$). All experiments yielded wavelengths in the vacuum-ultraviolet spectral regime between 200 nm and 105 nm. Yet we are not aware of an implementation of coherent control with high control strength in frequency conversion towards the EUV spectral regime. A third, macroscopic approach towards higher efficiency is to increase the $N \cdot L$ product of interaction length L and particle density N, to gain a stronger interaction of light and medium. However, this only is possible by tight confinement of medium and laser beam inside a hollow core waveguide, overcoming the limit in interaction length imposed by the finite Rayleigh length of a focused Gaussian beam. Simultaneously, phase matching is possible by balancing the gas dispersion with the waveguide dispersion of an appropriate mode [31, 32]. Hollow waveguides have

been applied for frequency conversion of narrowband (ns) pulses, as well as for generation of multiple harmonics from ultra-short pulses [33]. Despite the great prevalence of hollow core waveguides, even in form of a commercial system[1], we are not aware of a systematic study exploring the possibility of resonantly enhanced harmonic generation inside a waveguide, especially at intensities in excess of 1 TW/cm^2.

In this work, we investigate the idea of efficient, harmonic generation in a noble gas medium. In chapter 1, we derive the basic theory for resonance-enhanced harmonic generation. Due to the similarity between the level schemes of all noble gases, we pick argon as an example, to identify promising spectral regions for frequency conversion from the transmission and dispersion characteristics of the gas. For a systematic study of resonance effects, a tunable laser system generating laser pulses with a frequency bandwidth small enough to properly address isolated atomic resonances is required. From the frequency dependent nonlinear polarizability, in particular for a five photon resonance in argon, we derive the requirements for our laser system to resolve the multi-photon resonance as well as the tuning range to cover the expected AC Stark shift of the excited level at several TW/cm^2 laser intensity. In chapter 2, we present the (ps) laser system capable of delivering mJ of pulse energy tunable in the visible regime. In chapter 3, we investigate the feasibility to enhance multiple harmonics by an intermediate resonance. First, we track the enhancement line shape of the fifth harmonic as the five-photon resonance is shifted further and further towards higher energy when the laser intensity is increased. In tuning the laser to the maximum of the recorded line shapes, we then achieve enhancement of multiple harmonics within the EUV regime at 17 and 50 TW/cm^2 fundamental intensity. With proof of the importance of intermediate resonances also for higher harmonics in chapter 4, we implement coherent control in frequency up-conversion towards a wavelength of 102 nm. We systematically investigate and optimize all relevant parameters to reach strong control of the harmonic yield, either enhancing the yield or suppressing it by appropriate choice of the relative phase between two fundamental laser beams of different frequency. In particular, we explore the preconditions for strong coherent control that arise from the short pulse length as well as dispersion at the ultraviolet fundamental wavelength. Finally in chapter 5, we combine the atomic effect of resonance enhancement with the macroscopic approach of waveguiding to yield phase matched fifth-harmonic generation in the vicinity of the five photon resonance already investigated in chapter 3, but at roughly a factor of 1000 higher $N \cdot L$, yielding more than a factor of 800 higher efficiency compared to the atomic jet. We determine the dependence of the VUV pulse energy with respect to gas pressure and resonance detuning, yielding maximum efficiency in the vicinity of the Stark shifted resonance. By comparison with a numerical model, including the Stark shift as well as multi-color, multi-mode harmonic generation, we explain the modified enhancement lineshape in resonantly enhanced, phase matched harmonic generation and reveal a significant enhancement of the conversion efficiency by quasi phase-matching inside the waveguide.

[1] KMLabs XUUS (eXtreme Ultraviolet Ultrafast Source)

Chapter 1

Basic theory of harmonic generation in atomic gases

In this chapter an introduction to the basics of frequency conversion is given. Starting from the general case of the nonlinear wave equation, we specialize on the frequency up-conversion in noble gases at high intensity. From the governed, specialized differential equations, we identify and derive all linear and nonlinear parameters. These parameters are calculated and presented for the special case of argon to motivate the requirements for the experiment and enable the interpretation of the experimental data gained with this medium.

1.1 Nonlinear wave equation

Frequency conversion relies on nonlinear interaction of (laser) light with matter. To efficiently convert visible laser radiation towards higher frequencies we utilize resonances of the medium for phase matching and to enhance the nonlinearity, hence increasing the conversion efficiency.

In this chapter we first introduce the linear response in form of the linear susceptibility and the nonlinear response in form of the nonlinear susceptibility. Thereafter we discuss the effect of intense laser radiation on the atomic levels of the atom and its consequences for resonance enhancement.

When an electromagnetic wave is incident on a nonmagnetic medium, the atoms get polarized by the electromagnetic field, contributing a polarization $\widetilde{\boldsymbol{P}}$ to the wave equation[1] [34]

$$\nabla^2 \widetilde{\boldsymbol{E}} - \frac{1}{c^2}\frac{\partial^2}{\partial t^2}\widetilde{\boldsymbol{E}} = \frac{1}{\epsilon_0 c^2}\frac{\partial^2}{\partial t^2}\widetilde{\boldsymbol{P}}. \tag{1.1}$$

Here $\widetilde{\boldsymbol{E}}$ is the electric component of the plane electromagnetic light wave oscillating at angular frequency ω, c is the speed of light in vacuum and ϵ_0 is the vacuum permittivity. The polarization also oscillates at frequency ω. In general, the electromagnetic field as well as the polarization are vectorial quantities that can have arbitrary orientation with respect to each other. For an atomic, point symmetric medium however, the polarization vector is parallel to the electric field vector. For further simplification throughout this work we assume the wave with

[1] We state here the wave equation commonly used in nonlinear optics [34], neglecting $(\triangle \cdot \widetilde{\boldsymbol{E}})$ and assuming no free charges.

the electric field magnitude $\widetilde{E} = \frac{1}{2}E\cdot(e^{-i(\omega t - k_0 z)} + c.c)$ to travel in positive z-direction with the propagation constant in vacuum $k_0 = \omega/c$. The electric field is a vertically polarized plane wave or mildly focused beam so that the first and second derivative of the (complex) spatial envelope $E(x, y, z)$ in the transversal coordinates x, y are much smaller than the respective derivatives in propagation direction z. Because of the centrosymmetry of our nonlinear medium, we can reduce the wave equation to the scalar form

$$\frac{\partial^2}{\partial z^2}\widetilde{E} - \frac{1}{c^2}\frac{\partial^2}{\partial t^2}\widetilde{E} = \frac{1}{\epsilon_0 c^2}\frac{\partial^2}{\partial t^2}\widetilde{P}. \tag{1.2}$$

For a single driving field, much smaller than the electric field between nucleus and electrons of the atom ($\approx 5 \cdot 10^{11}$ V/m for hydrogen) we can treat the incident electromagnetic field as a perturbation and expand the polarization as a Taylor series in E:

$$\widetilde{P} = \epsilon_0 \sum_{l=1}^{\infty} \chi^{(l)}\widetilde{E}^{(l)} \tag{1.3}$$

We define the polarization of order l

$$\widetilde{P}^{(l)} = \epsilon_0 \chi^{(l)}\widetilde{E}^{(l)} = \epsilon_0 \chi^{(l)}(E \cdot e^{-i(\omega t - k_0 z)} + c.c.)^l \tag{1.4}$$

From this equation we see that the polarization of order l has terms oscillating at $l \cdot \omega$ that can be a source of an electromagnetic field at frequency $l \cdot \omega$.

The polarization of order $l = 1$ oscillates with the same frequency as the incident field. When substituted back into equation 1.2, this polarization gives rise to the complex refractive index n, that modifies the propagation of the incident wave (see chapter 1.2.2). We can then rewrite equation 1.2 accounting for the refractive index:

$$\frac{\partial^2}{\partial z^2}\widetilde{E} - \frac{n^2}{c^2}\frac{\partial^2}{\partial t^2}\widetilde{E} = \frac{1}{\epsilon_0 c^2}\frac{\partial^2}{\partial t^2}\widetilde{P}^{NL} \tag{1.5}$$

By absorbing the linear polarization inside the wave equation, the right hand side of equation 1.5 is reduced to the nonlinear polarization $\widetilde{P}^{NL} = \epsilon_0 \sum_{l=2}^{\infty} \chi^{(l)}\widetilde{E}^{(l)}$. In order to examine the growth of electric fields at higher harmonic frequencies $\omega_j = j\omega_1$, we now rewrite the equation in terms of the electric field

$$\widetilde{E}_j = E_j \cdot e^{-i(\omega_j t - \int_0^z k(z')_j \, \mathrm{d}z')} + c.c. \tag{1.6}$$

with the propagation constant $k_j(z) = n_j(z)\omega_j/c$ inside a medium of refractive index n(z). We allow for a inhomogenity of the refractive index in z-direction, to cover the actual situation in our experiments. This changes the kz term in the exponential to the integral form [35] $\int_0^z k(z')\,dz'$. We first examine the wave equation for a linearly responding medium ($\tilde{P}_{NL} = 0$):

$$\left[\frac{\partial^2}{\partial z^2}E_j + 2i \cdot k_j \frac{\partial}{\partial z}E_j + i\frac{\partial k}{\partial z}E_j\right] e^{-i(\omega_j t - \int_0^z k(z')_j \mathrm{d}z')} + c.c. = 0. \tag{1.7}$$

On the left hand side in addition to derivatives of the electric field, also a derivative of the propagation constant k arises. The solution [35] of this source free wave equation, assuming a smooth change in the refractive index $n(z)$, simply shows a decrease in $E_j \propto \sqrt{n(z)}^{-1}$. When the solution is inserted into the Maxwell equations $\nabla \times H = \frac{\partial}{\partial t}\epsilon_0 \tilde{E} + \tilde{P}^{(1)} + \tilde{J}$ in a dielectric medium[2], the dependence of the magnetic field shows an increase $B_j \propto \sqrt{n(z)}$. Hence the average transmitted power $\frac{1}{2}\tilde{E} \times \tilde{H}^*$is constant. As a consequence, after a medium of symmetric refractive index profile (and linear response) in vacuum, the magnitude of the electric fields is restored to the initial value after the medium. In our dilute atomic media, the spatial change of the refractive index n will typically not exceed 10^{-4}. This the change of the electric fields during the interaction will be $\ll 1‰$. We simply neglect the term $i\frac{\partial k}{\partial z}E_j$ and calculate the generated power after the medium only. The resulting wave equation including the nonlinearity then reads:

$$\left[\frac{\partial^2}{\partial z^2}E_j + 2i \cdot k_j \frac{\partial}{\partial z}E_j\right] e^{-i(\omega_j t - \int_0^z k(z')_j \mathrm{d}z')} + c.c. = \frac{\omega_j^2}{\epsilon_0 c^2} P^{NL}(\omega_j) \cdot e^{-i(\omega_j t - j \cdot \int_0^z k_1(z')\mathrm{d}z')} + c.c. \tag{1.8}$$

On the right hand side only those terms of the nonlinear polarization $\widetilde{P}^{NL}$, that oscillate with the same frequency ω_j can act as a source. Here $P^{NL}(\omega_j)$ is the (time independent) Fourier amplitude of the component of $\widetilde{P}^{NL}$, that is oscillating at frequency ω_j. A further simplification is possible, assuming that the change in electric field envelope E_j at $\omega_j = j\omega$ is small compared to the propagation constant $k_j = n(\omega) \cdot \omega_j / c$ inside the medium ($\frac{\partial^2}{\partial^2 z}E_j \ll k_j \frac{\partial}{\partial z}E_j$, slowly varying envelope approximation SVEA). We then can neglect the second derivative with respect to z and get a first order differential equation for the amplitude of the j^{th} harmonic [34]:

$$\frac{\partial}{\partial z}E_j = \frac{i}{2k_j}\frac{\omega_j^2}{\epsilon_0 c^2} P^{NL}(\omega_j) \cdot e^{i(\int_0^z j \cdot k_1(z') - k_j(z'))\,\mathrm{d}z'} \tag{1.9}$$

Starting from this equation the electric field at frequency ω_j can be derived by solving the system of coupled equations generated for the E_j by equation 1.5.

Assuming an undepleted pump field E_1, the yield of the harmonics can in good approximation be calculated by integration in z:

$$E_j(L) = \int_{-L/2}^{L/2} \frac{i}{2k_j}\frac{\omega_j^2}{\epsilon_0 c^2} P_{NL}(\omega_j) \cdot e^{i\int_0^z (j \cdot k_1(z') - k_j(z'))\,dz'}\,dz \tag{1.10}$$

A necessary condition for efficient harmonic generation is, that the exponential $e^{i\int_0^z (j \cdot k_1(z') - k_j(z'))\,dz'}$stays close to unity, so the accumulated phase mismatch $\Delta\Phi^{(j)} = \int_0^z (j \cdot k_1(z') - k_j(z'))\,dz'$ between harmonic and fundamental is small.

[2]again with vanishing free current density$\tilde{J} = 0$, and $B = \mu_0 H$

In the simple case of a homogeneous medium at vanishing wave vector mismatch $\Delta k = j \cdot k_1 - k_j$, this condition is met, so for the harmonic intensity I_5 we yield the proportionality

$$I_j \propto |P_{NL}|^2 \cdot L^2 \propto (N \cdot L)^2 \cdot |\alpha^{(j)}|^2 \cdot I^j. \tag{1.11}$$

Hence the harmonic intensity can be increased by increasing the fundamental intensity I_1, the nonlinear atomic polarizability $\alpha^{(j)}$ or the product of number density and interaction length.

We now introduce the functional dependence of the polarizabilities $\alpha^{(i)}$ up to fifth order to point out possible ways to increase the nonlinear response. Thereafter the compatibility of these approaches with the phase matching criterion is examined.

1.2 The atomic polarizability

The polarizability of atomic gases can be calculated for an ensemble of a free atom in a quantum mechanical treatment. Within the perturbative regime (at intensities well below $\approx 30\,\mathrm{TW/cm^2}$ [36]) the Hamiltonian of atom and field can be split into the Hamiltonian $\widehat{H}_0$ of the free atom and the energy $\hat{\widetilde{V}}(t)$ of the interaction between atom and the applied radiation field $\widetilde{\boldsymbol{E}}(t)$

$$\hat{\widetilde{H}} = \hat{H}_0 + b\hat{\widetilde{V}}(t). \tag{1.12}$$

We can derive the polarization of the atom in the dipole approximation[3]:

$$\hat{\widetilde{V}}(t) = -\hat{\boldsymbol{\mu}} \cdot \widetilde{\boldsymbol{E}}(t) \tag{1.13}$$

Here $\hat{\boldsymbol{\mu}} = e\hat{\boldsymbol{r}}$ is the dipole moment operator and, involving the electron charge e and the position operator $\hat{\mathbf{r}}$ The electric field is considered as linearly polarized parallel to the unitary vector $\mathbf{e}$: $\widetilde{\boldsymbol{E}}(t) = E(t) \cdot \mathbf{e}$. The perturbative multiplier $b \in \{0..1\}$ scales the strength of interaction, and is the expansion parameter in this perturbation theory [37].

1.2.1 The linear polarizability of noble gas atoms

The linear polarizability $\alpha^{(1)}$ of the atom is the proportionality of the ensemble averaged expectation value of the induced dipole moment $\langle\hat{\boldsymbol{\mu}}\rangle$ (oscillating at frequency ω) with respect to the electric field $\widetilde{\boldsymbol{E}}(t)$. The induced dipole moment is a result of the interaction between atom and electric field and is calculated from the first order correction $\rho^{(1)}$ for the density matrix of atom and field ρ_f

$$\rho_f = \rho^{(0)} + b\rho^{(1)} + b^2\rho^{(2)} + b^3\rho^{(3)} + \ldots \tag{1.14}$$

[3] We neglect the spatial dependence of the electromagnetic wave, as the size of an atom is much smaller than the length of the incident wave.

By knowledge of the initial population distribution onto the atomic levels i of the free atom $\rho_{ii}^{(0)}$ and the knowledge of all electric dipole transition moments[4] $\mu_{ml} = |m\hat{\boldsymbol{\mu}} \cdot \boldsymbol{e}l$ from level l to level m, the polarizability of the atom

$$\alpha^{(1)}(\omega) = \sum_l \rho_{ll}^{(0)} \underbrace{\sum_m \frac{1}{\hbar}\left[\frac{\mu_{ml}\mu_{lm}}{\omega_{ml} - \omega - i\gamma_{ml}} + \frac{\mu_{ml}\mu_{lm}}{\omega_{ml} + \omega + i\gamma_{ml}}\right]}_{\alpha_l^{(1)}(\omega)} \tag{1.15}$$

$$= \sum_l \rho_{ll}^{(0)} \cdot \alpha_l^{(1)}(\omega) \tag{1.16}$$

can be computed. The damping $\gamma_{ml} = \gamma_{lm} = \frac{1}{2}(\Gamma_m + \Gamma_l) + \gamma_{ml}^{(coll)}$ is the dipole dephasing rate with the individual decay rates Γ_i of the levels and the decay rate due to collisions[5] $\gamma_{ml}^{(coll)}$. Here we have already assumed our linearly polarized electric field and only sum over those transition moments parallel to the polarization direction. The polarizability $\alpha^{(1)}(\omega)$ then is a scalar quantity, consisting of a sum over all polarizabilities $\alpha_l^{(1)}(\omega)$ of the atom in state l, weighted with the respective population probability $\rho_{ll}^{(0)}$. The second term of the sum in equation 1.16 only approaches resonance for negative transition frequencies ω_{ml}, i.e. for atoms prepared in an excited state. Also in the limit of low frequencies compared to the transition frequency it has to be considered[6].

When the atom initially is in the ground state ($\rho_{11} = 1$, $\rho_{ll} = 0$ for $l \neq 1$), the summation over l yields [37]:

$$\alpha_1^{(1)}(\omega) = \frac{1}{\hbar}\sum_m \left[\frac{\mu_{1m}\mu_{m1}}{\omega_{m1} - \omega - i\gamma_{m1}} + \frac{\mu_{m1}\mu_{1m}}{\omega_{m1} + \omega + i\gamma_{m1}}\right] \tag{1.17}$$

1.2.2 The linear refractive index

From this equation we can model the linear susceptibility $\chi^{(1)}(\omega) = N \cdot \epsilon_0^{-1}\alpha^{(1)}(\omega)$ with the number density $N(p) = \frac{p}{k_B T}$, assuming an atomic ideal gas at temperature T and static pressure p with the Boltzmann constant k_B. The complex refractive index of the medium then reads

$$n(\omega) = \sqrt{1 + \chi^{(1)}(\omega)} = \sqrt{1 + N \cdot \epsilon_0^{-1}\alpha^{(1)}(\omega)} \tag{1.18}$$

Through the wave equation (1.5) the real part $n' = \mathrm{Re}[n]$ defines the phase velocity $c_m(\omega) = c/n'(\omega)$ inside the medium, the imaginary part $n'' = \mathrm{Im}[n]$ defines the (intensity) absorption coefficient $\alpha_{Beer} = 2n''\omega/c$ known from Beer's law.

Figure 1.1 as an example shows the refractive index of argon at normal conditions as computed by the methods explained in chapter 5.2.4. The blue line

[4] We use the scalar transition dipole moments μ_{ml} which arise from the projection of dipole operator $\hat{\boldsymbol{\mu}}$, projected onto the field unit vector $\mathbf{e}$. Because of the three spatial dimensions $\mu_{ml}\,\mu_{lm} = \frac{1}{3}|m\hat{\boldsymbol{\mu}}l|^2 = \frac{1}{3}|\hat{\boldsymbol{\mu}}_{ml}|^2$.

[5] In our experiments at $N \approx 10^{17} cm^{-3}$ the linewidth including collisional broadening [38], as well as Doppler broadening is lower than 10 GHz. This is almost three orders of magnitude lower than the laser linewidth of 1 THz used in the experiments and hence negligible.

[6] For propagation of a laser at $\lambda = 500\,\mathrm{nm}$ in argon, neglecting all second terms of the sum results in a calculated polarizability 40 % too small. For $\lambda = 100\,\mathrm{nm}$ the error is $< 8\,\%$.

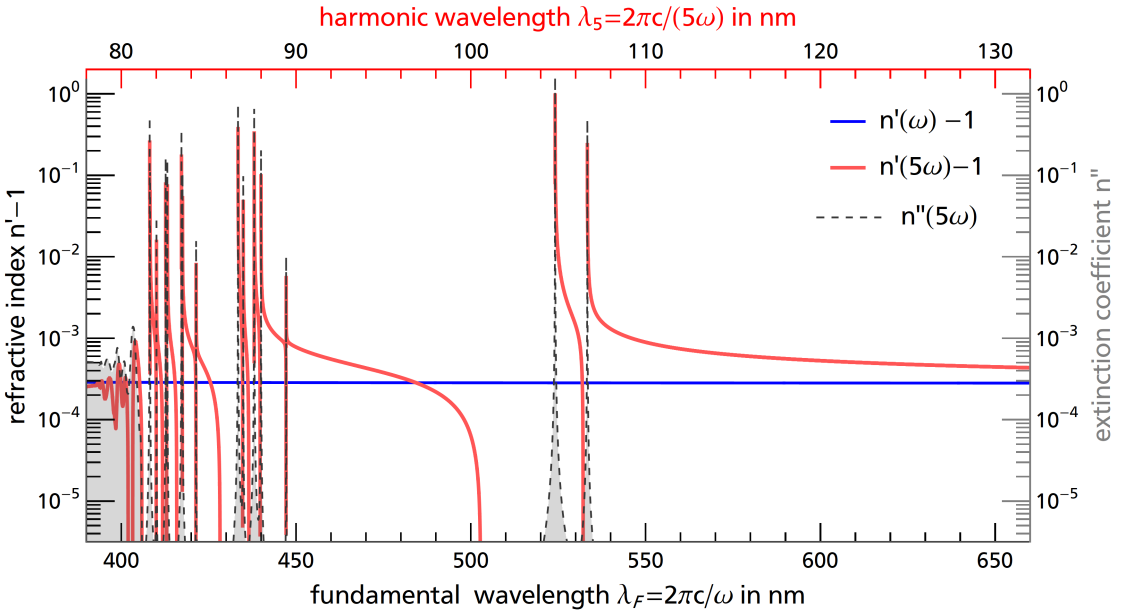

Figure 1.1: Refractive index $n' = \mathrm{Re}[n]$ of argon for visible radiation at frequency ω (blue) and the fifth harmonic 5ω (red), together with the extinction coefficient $n'' = \mathrm{Im}[n]$ (gray, right abscissa) at normal conditions (1013.25 mbar, 0 °C). A collisional broadening of $\gamma_{coll} = 2\pi \cdot 20$ GHz is assumed. Above 81.5 nm the dense manifold of levels can no longer be identified by the limited experimental resolution of the data set used [39,40], so in this model of the refractive index a region of spectrally averaged absorption starts (81.5 - 78.672 nm, see chapter 5.2.4 for details).

depicts the refractive index for radiation of visible wavelength. It exhibits almost no dispersion due to the high detuning $\omega_{m1} - \omega$ of the corresponding light frequency ω from all atomic transition frequencies ω_{m1}. The red line depicts the refractive index n' at the fifth harmonic frequency within the VUV spectral regime. The extinction coefficient n'' (shown in gray) rises for each resonance in equation 1.17 when the atoms can be excited from the ground state to one of the higher levels. Below 78.672 nm the electrons are no longer promoted to bound states but ionized [41], resulting in a smooth absorption continuum.
To gain high efficiency in harmonic generation, re-absorption of the harmonic field by the medium should be avoided, so the transparency windows between the absorption peaks exhibit promising spectral regions for a given atomic level structure. Also in these regions, the difference in refractive index between the driving (fundamental) field and the fifth harmonic is low. Even a zero crossing of the difference in refractive indices is observed, canceling the plane wave phase mismatch (see chapter 1.3).

We now exploit ways to maximize the source term of the harmonic radiation by enhancing the nonlinear susceptibility.

1.2.3 The nonlinear polarizability of noble gas atoms

As discussed already in the previous paragraph, the energy levels of an atomic gas are rather sharp (compared to liquid or solid media, featuring broad energy bands). It is possible to obtain very large values of the nonlinear susceptibility using resonance enhancement [37]. This is especially favorable as due to the low number density $N = 2.5 \cdot 10^{19}\mathrm{cm}^{-3}$ of a gaseous medium (1013.25 mbar, 0 °C), its susceptibilities $\chi \propto N$ are usually about a factor of 10^4 smaller than those of bulk materials $N \approx 10^{23}\mathrm{cm}^{-3}$[7].

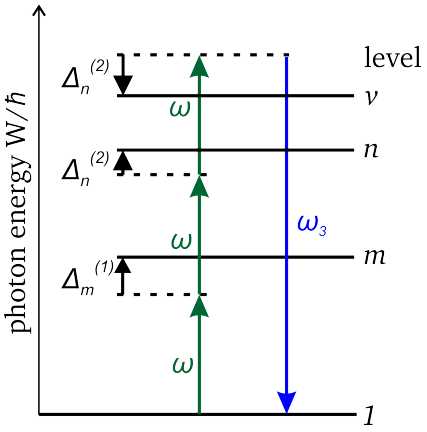

Figure 1.2: Simplified level scheme and resonance structure of the dominant coupling scheme for third harmonic generation. Black arrows depict the detunings, positive detunings upwards, negative detunings downwards.a Doppler broadening with a FWHM of $\Delta\nu_D = 6\,\mathrm{GHz}$.

For harmonic generation inside a monoatomic (centrosymmetric) medium, the first nonzero higher order susceptibility is the third-order susceptibility $\chi^{(3)} = N\epsilon_0^{-1}\alpha_0^{(3)}(\omega_s, \omega_p, \omega_q, \omega_r)$, which can be derived by the same perturbative approach as $\alpha^{(1)}$ from the third order correction of the density matrix (equation 1.14) [37] in terms of the perturbation by the electric field. The polarization involves three possible driving frequencies $(\omega_p, \omega_q, \omega_r)$ and one frequency of interest, at which the polarization oscillates $\omega_s = \omega_p + \omega_q + \omega_r$.

The nonlinear polarizability of third order, as found in literature [37], is a sum over all atomic levels, and all possible three photon couplings of those levels by the incident frequencies $\omega_p, \omega_q, \omega_r$. For third harmonic generation, the driving frequencies are degenerate $(\omega_p = \omega_q = \omega_r = \omega)$, so the 48 term sum over all levels reduces to an eight term sum. Of this sum, only one term dominates, when the atom is initially in the ground state and the laser is tuned to a multiphoton resonance. It corresponds to the coupling scheme depicted in Figure 1.2 and reads:

$$\alpha^{(3)}(3\omega, \omega, \omega, \omega) \approx \frac{1}{\hbar^3} \sum_{m,n,v} \frac{\mu_{1v}\mu_{vn}\mu_{nm}\mu_{m1}}{(\omega_{v1} - 3\omega - i\gamma_{v1})(\omega_{n1} - 2\omega - i\gamma_{n1})(\omega_{m1} - \omega - i\gamma_{m1})} \tag{1.19}$$

Here μ_{ij} are the dipole transition moments of each possible excitation pathway to a final level v, from which a photon of three times the driving frequency is emitted.The equation features the one-photon detuning to the first intermediate level m: $\Delta_m^{(1)} = \omega_{m1} - \omega$, (compare Fig. 1.2) the two photon detuning $\Delta_n^{(2)} = \omega_{n1} - 2\omega$, and the three photon detuning $\Delta_v^{(3)} = \omega_{v1} - 3\omega$. This nonlinear susceptibility

[7] The ratio of the third order nonlinear susceptibilities for the nonlinear refractive index for argon (normal conditions) and fused silica at λ =400 nm is $\chi_{Ar}^{(3)}(\omega, \omega, -\omega, \omega)/\chi_{fs}^{(3)}(\omega, \omega, -\omega, \omega) = 3.5 \cdot 10^{-26}/2.6 \cdot 10^{-22} = 1.4 \cdot 10^{-4}$ [42, 43].

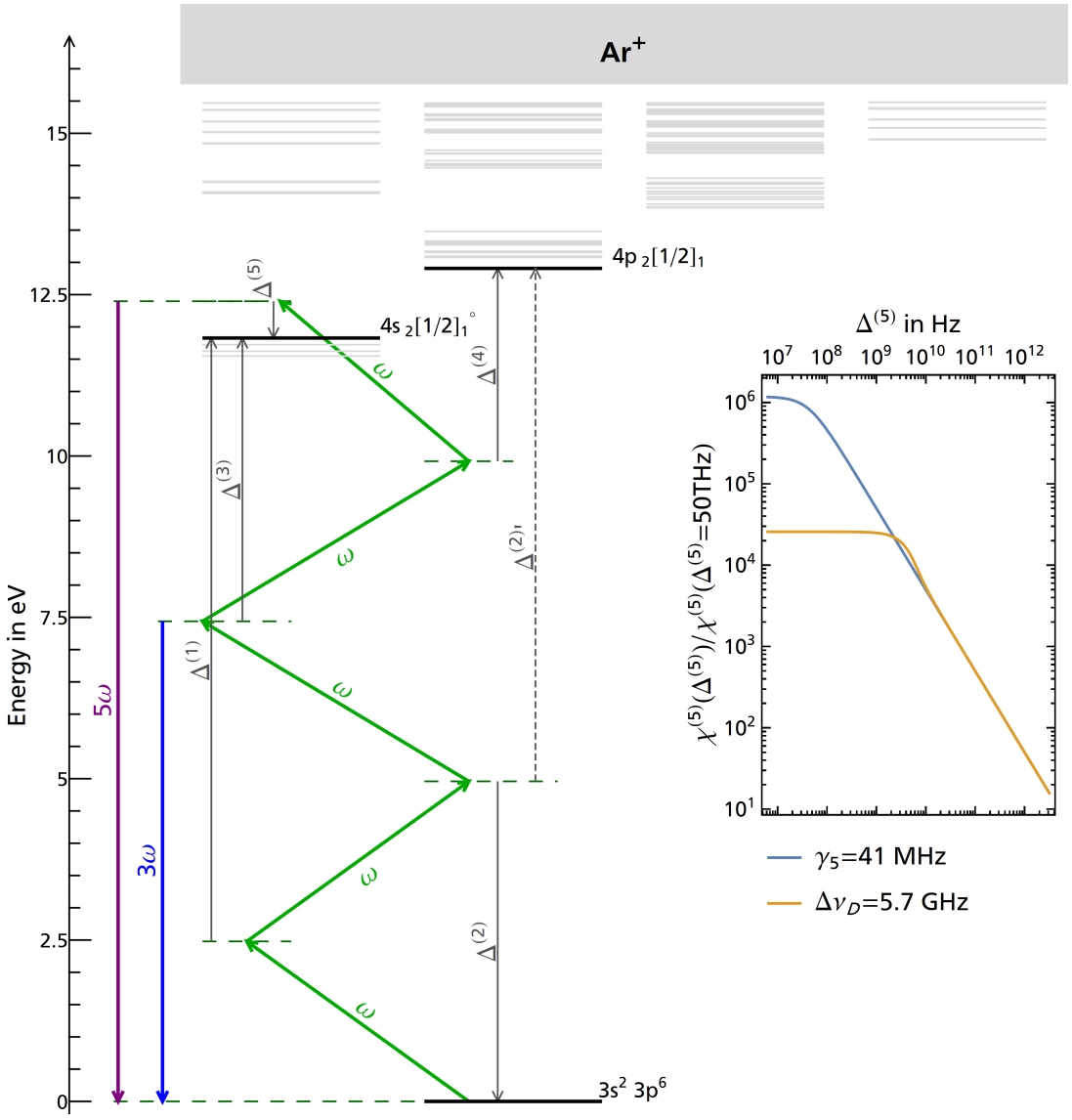

Figure 1.3: Level scheme of Argon, including the first 175 energy levels (gray horizontal lines) of lowest energy and angular momentum quantum numbers $L = 0$ (leftmost group) to $L = 3$ (rightmost group) [41]. Dashed horizontal lines show the "virtual levels" from Fig. 1.2, depicting the angular momentum (horizontal position) and energy acquired by the individual photons. Gray arrows show the respective multi-photon detunings towards the actual atomic energy levels (shown in black). From the third virtual level, the third harmonic can be generated (shown as blue arrow). Here all coupling schemes, involving the $4s^2[1/2]_1^\circ$ level can be enhanced by tuning the laser towards $\Delta^{(3)} = 0$.
Also shown is the level scheme for fifth-harmonic generation, featuring a possible five-photon resonance for $|x\rangle \rightarrow 4s_2[1/2]_1^\circ$. The generated harmonic photon within the VUV spectral regime is depicted in purple. (The realized coupling with $|m\rangle \rightarrow 4s_2[1/2]_1^\circ$ exhibits the smallest detunings and high transition dipole moments. Also depicted with a dashed arrow is a possible coupling with level $|n\rangle \rightarrow 4p_2[1/2]$, with a two photon detuning $\Delta^{(2)\prime} \approx 2 \cdot \Delta^{(2)}$.)
The inset shows the calculated resonance enhancement of the susceptibility $\chi \propto \frac{1}{(\Delta^{(5)} - i\gamma)}$ for detunings up to $\Delta^{(5)} = 2\pi \cdot 50\,\mathrm{THz}$ from the $4s_2[1/2]_1^\circ$ level. Shown are the cases of a natural line-shape (blue line) and a Doppler broadening with a FWHM of $\Delta\nu_D = 6\,\mathrm{GHz}$.

can be enhanced by tuning the laser frequency such, that one or more of the detunings vanish.

The simplified level scheme of Fig. 1.2 suggests an easily achievable "ladder-climbing" coupling scheme. In fact, the level structure of the noble gas atoms much less favors this possibility. A possible coupling scheme for third harmonic generation in argon is shown in 1.3. For visible radiation, all detunings for third harmonic generation are much bigger than the light frequency. Therefore the first detuning to vanish would be $\Delta^{(3)}$ at a fundamental laser wavelength of $\lambda_1 = 320\,\mathrm{nm}$. The same holds true also for the other noble gases, with xenon and krypton requiring slightly lower necessary photon energies and Neon and Helium requiring even higher photon energies for the first possible multi-photon resonance.

The energy ranges (8.3..12.1) eV, (9.9..14) eV and (11.6..15.8) eV of of the excited levels of the noble gases xenon, krypton are four to five times the photon energy of a visible photon. Consequently the nonlinear polarizability of fifth order is the lowest order polarizability to exhibit strong four- or five-photon resonances for visible radiation. It is derived by the same approach and simplifications as $\alpha^{(3)}$. The dominant terms of the fifth order nonlinear polarizability for fifth harmonic generation (FHG) close to a five-photon resonance are:

$$\begin{aligned}\alpha^{(5)}(5\omega,\omega,\omega,\omega,\omega,\omega) \;\approx\; & \frac{1}{\hbar^5}\sum_{m,n,v,w,x} \\ & \frac{\mu_{xv}\mu_{vn}\mu_{nm}\mu_{m1}}{(\Delta_v^{(3)}-i\gamma_{v1})(\Delta_n^{(2)}-i\gamma_{n1})(\Delta_m^{(1)}-i\gamma_{m1})} \\ & \cdot\; \frac{\mu_{x1}\mu_{wx}}{(\Delta_x^{(5)}-i\gamma_{x1})(\Delta_w^{(4)}-i\gamma_{w1})}\end{aligned} \tag{1.20}$$

Figure 1.3 shows such a possible five-photon coupling to generate light at a wavelength of $\lambda_5 = 100\,\mathrm{nm}$. The nonlinear susceptibility $\alpha^{(5)}$ can be enhanced by minimizing the five photon detuning $\Delta^{(5)}_{x=4s_2[1/2]^\circ} = \omega_{x1} - 5\omega$. When the coupling via level $|x\rangle$ dominates the nonlinear response, the summation over x can be dropped and all residual terms of the nonlinear polarizability will be proportional to $(\Delta_x^{(5)} - \gamma_{x1})^{-1}$. The value of the polarizability then exhibits a sharp enhancement peak with a magnitude proportional to the inverse linewidth $1/\gamma_{x1}$ of the level, while for detunings $\Delta^{(5)} \gg \gamma_{x1}$, the magnitude is proportional to $1/\Delta^{(5)}$. Hence the possible resonance enhancement compared to "off-resonant" interaction is $\approx \Delta^{(5)}/\gamma_{x1}$. For argon with a natural linewidth $\gamma_{4s_2[1/2]^\circ} = 41\,\mathrm{MHz}$, including an inhomogeneous Doppler broadening towards a Voigt line shape with a full width at half maximum (FWHM) of $\Delta\nu_D = 6\,\mathrm{GHz}$, the enhancement with respect to an "off-resonant" excitation at $\Delta_x^{(5)} = 50\,\mathrm{THz}$. is $\approx 3\Delta^{(5)}/\Delta\nu_D > 10^4$.

This enhancement can only be achieved, if the laser can be tuned "on resonance" and has a lower FWHM linewidth $\Delta\nu_L$ than the resonance. Resonance enhancement is therefore especially suitable for lasers with low linewidth.

Tuning the laser for vanishing Δ_i is also limited to the intermediate resonances, because for $\Delta^{(1)} = 0$ the fundamental radiation is absorbed and for $\Delta^{(5)} = 0$ the fifth harmonic is absorbed by the medium. It will be shown in the next section, that those two conditions will also give rise to a very large mismatch in propagation

constants for the two fields, so a residual detuning has to be maintained, maximizing the nonlinear response while still maintaining low absorption and phase mismatch. Work on optimal parameters with respect to absorption and phase mismatch has been published by Constant et.al. [44].

Resonances at intermediate levels in contrast (i.e. the two photon detuning towards level n for third harmonic generation) can be utilized without the disadvantage of absorption of either the driving radiation (for a one-photon resonance) or the generated harmonic (for a 3-photon resonance).

Another way of enhancing the nonlinear response of a medium is to increase the number density N by an increase in pressure p, so that the number of interactions per volume increases. As a consequence, the susceptibility of each order will scale by

$$\chi^{(N)} \propto N \underset{\text{ideal gas}}{\propto} p$$

As the propagation constants of harmonic and driving field are proportional to the refractive index at the respective frequencies, increasing N and increasing the length in equation 1.9 both relates to increasing the $N \cdot L$ product and is limited by a potential wave vector mismatch, as the refractive index is proportional to N in first approximation and consequently the accumulated phase mismatch $\Delta\Phi \propto N \cdot L$.

In the next section, the phase matching conditions for fifth-harmonic generation in the noble gas argon is derived to check the feasibility of resonance enhancement and increasing the number of interacting particles.

1.3 Phase matching

In section 1.1 we have already stressed the importance of a low accumulated phase mismatch $\Delta\phi = \int_0^z (j \cdot k_1(z') - k_j(z'))\, dz'$ in order to avoid destructive interference of harmonic photons generated at position z with those generated at an earlier position in the medium. Starting from phase matching of plane waves in a homogeneous medium we derive the modifications arising for the case of focused beams inside a inhomogenous jet of atoms.

1.3.1 Phase matching for a plane wave

For a plane wave incident on a homogeneous medium, the accumulated phase $\Delta\Phi_j$ reduces to $\Delta\Phi_j = (j \cdot k_1 - k_j) \cdot z = \Delta k_j z$ and thus the harmonic intensity I_j after the medium is

$$I_j(L) \propto \left| P_{NL}(\omega_j) \cdot \frac{e^{i\Delta k \cdot L} - 1}{\Delta k} \right|^2 \propto |P_{NL}(\omega_j)|^2 L^2 \mathrm{sinc}^2\left(\frac{\Delta k \cdot L}{2}\right) \tag{1.21}$$

For efficient frequency conversion it is desirable to maximize the interaction length and minimize the wave vector mismatch. Figure 1.4 shows the phase mismatch $\Delta\Phi_5$ of a plane wave electric field for our experimental conditions. Within the transparency windows, the phase mismatch can be neglected. For an atomic jet

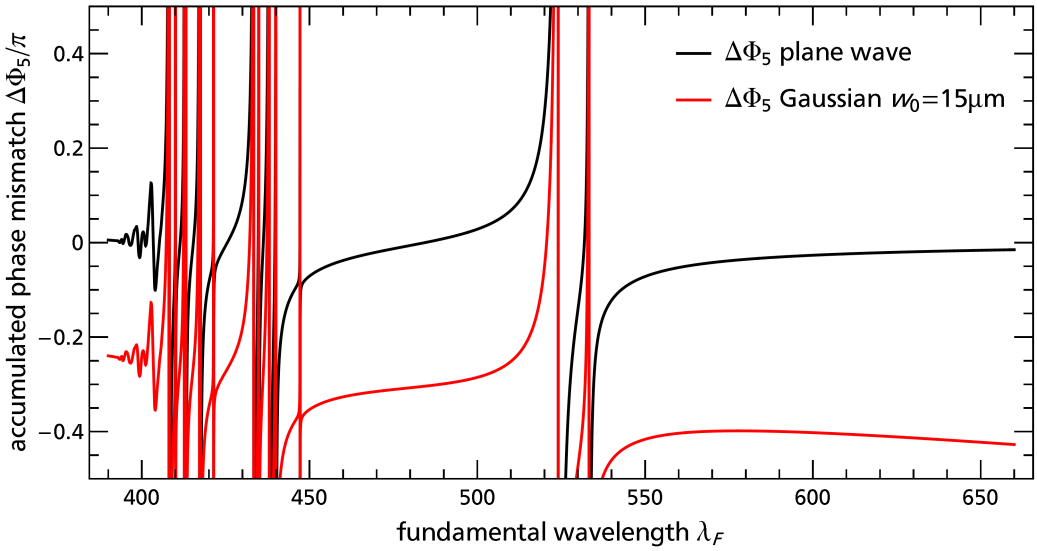

Figure 1.4: Accumulated phase mismatch for FHG inside an atomic jet of argon with a Gaussian density distribution at a maximal number density of $N = 5 \cdot 10^{17}\,cm^{-3}$. The jet has a FWHM width of $L_{FWHM} = 350\,\mu$mand is surrounded by vacuum (see chapter 2). The black line depicts the phase mismatch $\Delta\Phi_5$ of a plane fundamental wave. The red line shows the result $\Delta\Phi_5^{(Gauss)}$ for a focused Gaussian beam with a minimal beam waist w_0 =15 μm, centered at $z = 0$.

of fixed dimension instead of the interaction length also the number density (i.e the pressure) can be increased to yield a higher harmonic intensity between the resonances. However the maximal number density is limited by the experimental conditions (pump rates of the vacuum system, clustering of the gas and the actual gas consumption). When tuning close to five-photon resonances, exhibiting much higher nonlinear susceptibility, the phase mismatch exhibits the same rapid increase as the nonlinear susceptibility. So a finite detuning ($\Delta^{(5)} \approx -6.3$ THz for the $4s^2[1/2]_1^\circ$level) has to be maintained, to avoid back-conversion. This limits the amount of possible enhancement.

1.3.2 Phase matching of focused Gaussian beams

Due to the scaling of the nonlinear polarization $P^{(j)} \propto E_1^j$ with the j^{th} power of the fundamental electric field, high intensity is a premise for efficient frequency up-conversion. At a given average power a high intensity can be achieved by use of a Gaussian beam of (ultra-) short laser pulses focused to a small $1/e^2$ beam radius w_0 incident on the nonlinear medium. The electric field amplitude is then modified to:

$$E_1(r,z) = E_1 \frac{w_0}{w(z)} e^{-\frac{r^2}{w(z)}} e^{\frac{ikr^2}{2r(z)}} e^{i\Phi_{Gouy}(z)}$$

Due to the focusing, an additional Gouy-Phase $\Phi_{Gouy}(z) = \arctan(z/z_r)$ is acquired during the propagation through the focus. It can be shown [34], that the

harmonic field E_j is generated with the same Rayleigh length $z_r = \frac{\pi w_0^2}{\lambda}$, as the fundamental beam. So the nonlinear polarization $P^{NL}(\omega_j)$ exhibits a phase shift of $j\left(\Phi_{Gouy}(L/2) - \Phi_{Gouy}(-L/2)\right)$ during the propagation from $z = -L/2$ to $z = L/2$. The j^{th} harmonic only acquires a shift equal to $\left(\Phi_{Gouy}(L/2) - \Phi_{Gouy}(-L/2)\right)$. As a consequence, the accumulated phase mismatch after a medium of length L is

$$\Delta\Phi_j^{(Gauss)} = \int_{-L/2}^{L/2} (j\,k_1 - k_j)\,dz' - (j-1)\left(\Phi_{Gouy}(L/2) - \Phi_{Gouy}(-L/2)\right).$$

The red line in Fig. 1.4 depicts our experimental conditions with a focused Gaussian beam of $w_0 = 15\,\mu$m. Within the transparency windows between the atomic resonances the phase mismatch stays well below the critical value of π. However the negative contribution of the Gouy phase is clearly visible. Focusing shifts the optimal phase matching conditions towards the atomic resonance frequencies and thus favors resonance enhancement by a five photon resonance. The strongest resonance occurs when the fifth harmonic gets resonant with the transition to the $4s^2[1/2]_1^\circ$ level at 104.822 nm, i.e. when the driving laser is tuned to 524.1 nm.

Perfect phase matching near this resonance is achieved at 520.6 nm. Tuning close to the resonance will increase the harmonic yield, until at 523.2 nm the harmonic accumulates a phase mismatch of π, leading to back conversion and a reduced efficiency. So the detuning for highest harmonic yield under these experimental conditions is roughly 1 nm (corresponding to $\Delta^{(5)} \approx -4.75$ THz). When the resonances are closer together as for the 400-450 nm wavelength interval of the driving laser, the optimal detuning is even lower[8]. The possible resonance enhancement next to this five-photon resonance is examined experimentally in chapter 3.

In the transparency windows between the atomic transitions, frequency conversion is possible without a significant phase mismatch. However in the considered case of a rather short ($L_{FWHM} = 350\,\mu$m) atomic jet at low particle density $N \approx 10^{17}\,cm^{-2}$ the conversion efficiency will be low due to the low $N \cdot L$ product. Nevertheless a resonance enhancement by e.g. a four-photon resonance is still possible and will be discussed in the experiments of chapter 4.

The problem of low $N \cdot L$ can be addressed in a confined geometry like a long hollow core waveguide. This waveguide confines the medium and enables both, high L and N values. If furthermore enables phase matching at those high $N \cdot L$ values by compensation of the gas dispersion by the waveguide dispersion. Theoretical as well as experimental treatment of this approach is presented in chapter 5.

[8]The findings presented here are at $z_r \approx 4L$, i.e. for constant fundamental electric field E_1.When the medium is comparable to or longer than the Rayleigh length z_r, the divergence of the Gaussian beam leads to a linear decrease in electric field with respect to z. This reduces the source term P_{NL} for large z and limits the length of significant harmonic generation to the confocal length $-z_r < z < z_r$. The mathematical treatment presented by Boyd [34] incorporates this effect and should be used in this case.

1.4 Dynamic shift of energy levels

Starting from equations 1.12 and 1.14 it can be shown [45, 46], that from this polarizability a second order correction ($\propto E^2$) (known as the AC Stark shift) in the energy eigenvalue of the level m results.

$$\Delta W_l^{(2)} = -\frac{E_0^2}{4}\alpha_l^{(1)}(\omega) = -\frac{E_0^2}{4}\sum_m \frac{1}{\hbar}\left[\frac{\mu_{ml}\mu_{lm}}{\omega_{ml}-\omega-i\gamma_{ml}} + \frac{\mu_{ml}\mu_{lm}}{\omega_{ml}+\omega+i\gamma_{ml}}\right] \tag{1.22}$$

For the ground state $l = 1$, this shift can be directly evaluated, when the refractive index of the gas $n = \sqrt{1+N\alpha_1^{(1)}\epsilon_0^{-1}}$ is known. For $\lambda_1 = 520\,\mathrm{nm}$ in argon, we calculate a Stark shift of the ground state of $\Delta W_1^{(2)} = -2.2\,\mathrm{meV/(TW\,cm^{-2})}$. This small correction can usually be neglected compared to all other Stark shifts.

We now approximate the Stark shift for highly excited levels l, similar[9] approximation was shown by of Pan et. al. [48]. If the laser frequency ω is not specifically tuned to an atomic transition frequency ω_{ml}, the detuning term $\omega_{ml}-\omega$ dominates the denominator and we can neglect the linewidth γ_{ml}.

$$\Delta W_l^{(2)} = -\frac{E_0^2}{4}\alpha_l^{(1)}(\omega) = -\frac{E_0^2}{4}\sum_m \frac{|\mu_{lm}|^2}{\hbar}\left[\frac{1}{\omega_{ml}-\omega}+\frac{1}{\omega_{ml}+\omega}\right] = -\frac{E_0^2}{4}\sum_m \frac{|\mu_{ml}|^2}{\hbar}\cdot\frac{2\omega_{ml}}{\omega_{ml}^2-\omega^2}$$

We substitute the oscillator strength[10] $f_{lm} = \frac{2m_e\omega_{ml}|\mu_{lm}|^2}{\hbar e^2}$

$$\Delta W_l^{(2)} = -\frac{E_0^2 e^2}{4m_e}\sum_m \cdot\frac{f_{ml}}{\omega_{ml}^2-\omega^2}.$$

For highly excited states (with a main quantum number $n_l \gg 1$) of high angular momentum quantum number L, transitions to the bound states of low energy and low angular momentum are dipole forbidden. Thus for those levels, the sum contains only couplings between the state $|l\rangle$ and other highly excited states $|m\rangle$. The transition frequencies $\omega_{ml} \propto n_l^{-1} - n_m^{-1}$ between these levels are all much smaller than the light frequency of visible radiation ω and consequently we can apply the high frequency approximation $\omega^2 \gg \omega_{ml}^2$:

$$\Delta W_l^{(2)} \approx \frac{E_0^2 e^2}{4m_e\omega^2}\sum_m \cdot f_{ml} \underset{TRK}{=} \frac{E_0^2 e^2}{4m_e\omega^2}$$

In the second step we used he Thomas-Reiche-Kuhn (TRK) sum rule $\sum_m f_{lm} = 1$. As a result the shift of an highly excited level (with low coupling to the ground state) is approximately the quiver energy of an electron in an electromagnetic field

$$\Phi_p = \frac{e^2}{4m_e\omega^2}E_0^2.$$

[9] We use the field gauge, while Pan et. al. start from the Hamiltonian in radiation gauge (vector potential). Their derived formula (2) for the general Stark shift gives the same transition energies between two states l, m as our equation [47].

[10] Please note, that $\mu_{lm}$is the dipole transition matrix element parallel to the laser polarization and hence $f_{lm} = \frac{2m_e\omega_{ml}|\mu_{lm}|^2}{\hbar e^2} = f_{lm} = \frac{2m_e\omega_{ml}}{\hbar e^2}\frac{1}{3}|m\hat{\mu}l|^2$.

The probability density function of those levels extends up to nanometer from the core, so the dipole transition moments μ_{ml} towards the tighter bound states are very low and the electron within this orbital can quiver almost unrestricted by the atomic potential, consequently experiencing a quite similar energy correction as a free electron. For $\lambda_1 = 520\,\text{nm}$, the ponderomotive energy is $25\,\text{meV}/(\text{TW}\,\text{cm}^{-2})$. With the rather small energy correction for the ground state $\Delta W_1^{(2)} \leq 0.1\Phi_p$, the Stark shift of the excited levels dominates the transition frequency ω_{l1} of any $|1\rangle \longleftrightarrow |l\rangle$ transition in noble gases.

Unfortunately for all other levels l, the Stark shift $\Delta W_l^{(2)}$ is highly dependent on the detuning terms $\Delta^{(1)} = \omega_{ml} - \omega$ and requires knowledge of all dipole moments μ_{ml} (or oscillator strengths f_{ml}) for transitions to the other levels m.

Another limitation is the derivation of the Stark shift $\Delta W_l^{(2)}$ from the second order perturbation theory. In the derivation the assumption is made, that the electric field in the Hamiltonian

$$\hat{\tilde{H}} = \hat{H}_0 + b\hat{\tilde{V}}(t) \tag{1.23}$$

is only a small perturbation. However for visible laser radiation at an intensity of about $1\,\text{TW/cm}^2$ already, the energy corrections $W_l^{(2)}$ do approach the energy spacing between subsequent levels $E_l - E_m$. In this case, the simple perturbative model no longer holds and the eigenenergies of the Hamiltonian $\hat{\tilde{H}} = \hat{H}_0 + \hat{\tilde{V}}(t)$ have to be evaluated in a non-perturbative method.

For temporally periodic electric fields, the Hamiltonian can be well approximated by a numerical calculation for a single active electron interacting with an inert core through a model potential, optimized to yield precise unperturbed eigenenergies [49, 50]. The act of calculating the data is subject to current theoretical research and exceeds the scope of this experimental work. It is shown, that for the example of argon the ponderomotive up-shift in energy is dominant compared to the complex additional structure for almost all levels above an intensity of $4\,\text{TW/cm}^2$. We note, that this finding is in good accordance to the above approximation for highly excited Rydberg levels deriving an energy shift of $\approx \Phi_p$.

As a result in this work, the change $\Delta\omega_{m1}$ in transition frequency $\omega_{m1} = (W_m - W_1)/\hbar$ towards the excited states as well as the continuum is expected to be approximately$\Delta\omega_{m1} \approx \Phi_p/\hbar$ for intensities above $4\,\text{TW/cm}^2$. At lower intensities intensity resolved multi-photon spectroscopy is carried out to to reveal potential stronger or weaker level shifts.

From the Stark shift also some limitations for resonantly enhanced frequency conversion arise: For visible radiation ($\lambda_1 = 520\,\text{nm}$), the ponderomotive frequency shift is $\Phi_p/h = 6.1^{THz}/_{TW\,cm^{-2}}$. Thus at $1\,\text{TW/cm}^2$, a given detuning $\Delta^{(5)}$ dynamically changes by more than its magnitude for optimal efficiency ($\Delta^{(5)} \approx -5\,\text{THz}$), derived in chapter 1.3.2. So for highest efficiency close to an atomic resonance, the fundamental peak intensity is limited to approximately $1\,\text{TW/cm}^2$. At higher intensities, the line shape in a multi-photon spectroscopic investigation will change towards a broader feature, affected by the temporal and spectral pulse shape as well as phase matching effects. We will investigate this behavior in the following chapter 3 and in chapter 5.

Chapter 2

Basic experimental setup and methodology

2.1 Laser system

Investigations on resonance enhancements in harmonic generation towards the VUV/EUV regime require on one hand high peak intensities (i.e. short, intense laser pulses), but on the other hand sufficient spectral resolution (i.e. not too short laser pulses). Thus we apply an amplified (ps) laser system for the experiments. Pulse durations of 1 ps require a bandwidth of about 0.5 THz and yield a spectral resolution of about 0.5 nm at 500 nm central wavelength. The possible intensities beyond 10 TW/cm^2 are sufficient to drive harmonic generation. To compare the harmonic yield at resonant conditions to the off resonant case, the laser system must also be tunable over several laser bandwidths. This also enables the study of several atomic resonances for different gas species. Furthermore, all relevant parameters for the interaction shall be constant or at least accessible by direct measurement. In the following, the developed laser system is described. It is based on commercially available oscillators, seeding a home-made power amplifier to gain picosecond laser pulses of more than a milijoule of pulse energy, sufficient to achieve peak intensities of more than 10 TW/cm^2 at a smooth and stable beam profile.

2.1.1 Laser pulse generation and manipulation

The picosecond laser pulses are generated in a commercial Kerr-lens mode-locked titanium-sapphire (Ti:Sa) oscillator [1] with a repetition rate of 76 MHz. This oscillator is pumped[2] by 11 W of continuous wave (cw) radiation at 532 nm wavelength and emits a pulse train of Fourier limited ultra-short pulses of 26 nJ energy at a center wavelength of 800 nm. The pulses have a sech^2 intensity envelope and a typical pulse length of τ =1.8 ps (FWHM). A synchronously pumped optical parametric amplifier (OPO) converts the radiation towards the visible spectral regime. It is a modified version[3] of a commercial system (APE OPO automatic) equipped with a fan-out periodically poled lithium niobate (PPLN) crystal and motorized crystal and cavity tuning. Inside the OPO a dispersion block serves to temporally separate the signal spectrum and thus tune the central wavelength by tuning the

[1] Coherent MIRA 900P

[2] The pump laser used for chapters 4 and 3 (Coherent VERDI V18) was replaced by a Laser Quantum Finesse 14 with the same beam characteristics for chapter 5

[3] see “Erweiterung zur automatischen Wellenlängenkontrolle in einem optisch parametrischen Oszillator” (Master’s thesis of René Kolb, 2015) for further details of the modified oscillator.

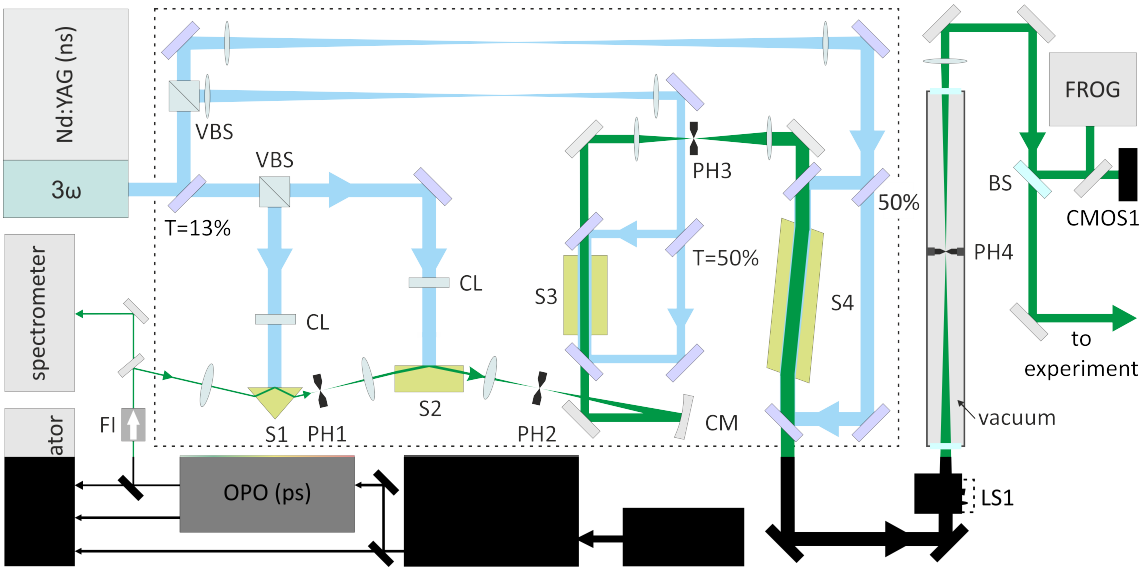

Figure 2.1: Schematic representation of the laser system (bottom), four stage (S1-S4) dye amplifier chain (dashed rectangle) and pulse characterization. The mirrors used in the amplifier are broadband dielectric mirrors for the visible (gray) and narrowband dielectric mirrors for 355 nm light (light purple). (FI: Faraday isolator, CL: cylindrical lens, VBS: variable beamsplitter, CM: concave aluminium mirror, LS1: lens system, BS: beam sampler, CMOS1: image sensor, PH: pinhole) (adapted from [51]).

cavity length. The signal radiation at a wavelength of λ_S =1010-1400 nm is intracavity frequency doubled towards λ_F =505-700 nm. These laser pulses serve as the fundamental (F) for all frequency conversion experiments in this work. The spectra of pump, signal and second harmonic (SHG) are monitored on a turning grating spectrometer[4] and the pulse durations are determined by a home made SHG autocorrelator[5].
The OPO generates pulses of Gaussian temporal and spectral envelope with a temporal FWHM of τ =1..1.5 ps and a spectral width $\Delta\lambda_F = 0.5...1$ nm (FWHM). Due to the group-velocity dispersion inside the OPO a spectral width $\Delta\lambda_F > 0.5$ nm results in an increased pulse duration. Therefore, the OPO is typically operated at $\Delta\lambda_F$ =0.5-0.7 nm, delivering 150 mW of average optical power and a corresponding pulse energy of 2 nJ. Central wavelength and bandwidth are monitored (and can be stabilized) by a home made Czerny-Turner spectrometer with 0.02 nm resolution and 0.04 nm accuracy [M2].

2.1.2 Amplification and spatial filtering

To detect fifth and higher harmonic signals we drive the noble gases with as high as possible peak intensities. The limiting factor is the resonance shift that should not exceed the pulse bandwidth for on-resonance excitation. As derived in the

[4]APE Wave Scan (version 1)
[5]We assume a Gaussian temporal shape for the (uncompressed) pulses from the OPO and a sech² shape for the pump pulses, for further details please refer to [B3]

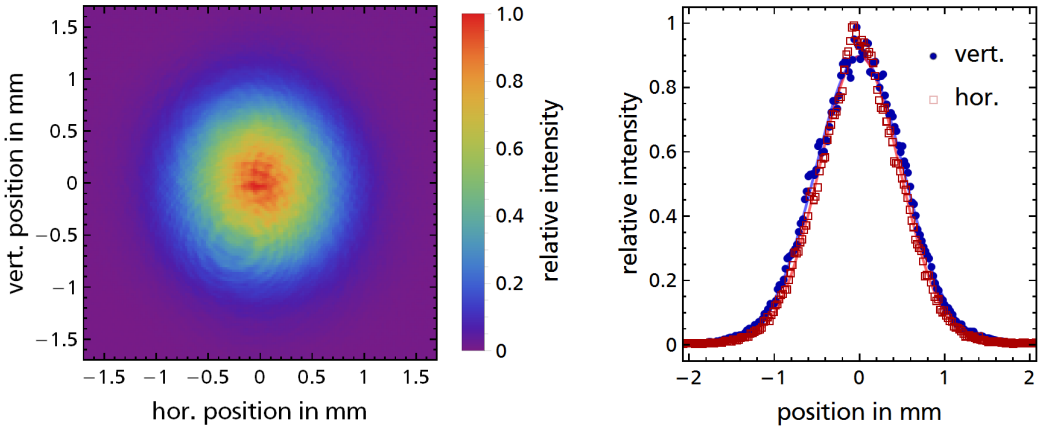

Figure 2.2: Optimized intensity profile of the amplified pulses at a pulse energy of $W_p \approx 200\,\mu$J after the last spatial filter at CMOS1 (left). The grainy structure and the interference rings are induced by the thin window covering the CMOS image sensor. The right figure shows a horizontal and vertical cut of the intensity profile together with a 2-dimensional Gaussian fit (red line: $w_{hor} = 0.95\,$mm, blue line: $w_{vert} = 1.04\,$mm).

previous chapter, we will require a peak intensity of up to 100 TW/cm². For a focusing geometry with a Gaussian beam radius of $w = 25\,\mu$m we require 1.5 mJ of pulse energy at a pulse duration of 1.5 ps for this intensity.

To reach this pulse energy, the pulses from the OPO are amplified by a home-made pulsed dye amplifier (see Fig. 2.1). The design is based on a pre-amplification stage consisting of two transversal pumped dye cells [30] to preserve the Gaussian beam profile and a power amplification stage consisting of two longitudinal pumped cells for efficient energy extraction. The pump energy is delivered by an injection seeded, frequency tripled Nd:YAG (ns) laser[6] at 20 Hz repetition rate. Up to 370 mJ of pump energy are available. A total of 50 mJ is vertically focused into the first (S1), and second amplification cell (S2). The beam line of the amplified pulses is spatially filtered by the pinholes PH1, PH2 and PH3 after each amplification stage to preserve the Gaussian beam shape and suppress amplified spontaneous emission (ASE)[7]. By relay imaging the pump beam onto both sides of the longitudinal dye cells, the uniformity of the gain is enhanced and the rotational symmetry of the amplified pulses is preserved, which improves the power handling of the last spatial filter and the coupling efficiency towards circular waveguides [M4]. The third cell (S3) is pumped by a Super-Gaussian transversal intensity distribution with a FWHM of 6 mm and the last cell by a 8 mm FWHM Super-Gaussian distribution from each side. To minimize ASE further, each lens of the amplifier is slightly tilted, so that no reflections are amplified. We reduce the introduced astigmatism by these tilts and the concave mirror (CM1), by a specially designed 2 m focal length lens system before the last pinhole (PH4). The synthetic CVD diamond pinhole[8] of 550 μm diameter resides inside a vacuum chamber to avoid filamentation and self focusing. The beam finally recollimated to a beam

[6] Spectra Physics QuantaRay PRO 230
[7] For further details on the design considerations see ref. [52]
[8] Lenox Laser CVD Diamond Aperture

waist of 1.0(1) mm (see Fig. 2.2) with a beam quality of $M^2 = 1.2(1)$, before entering the experiment. We reach more than 1 mJ of pulse energy, but the system is typically operated at 100-500 μJ to maintain better beam profile and tunability.

The optical path of pump and seed are matched to an accuracy of less than 1 ns. We set the delay between the pump pulses and the picosecond seed pulses for maximum gain. The FWHM of the temporal gain envelope gain (as determined by the FWHM of the temporal envelope of the residual ASE) is 7 ns. Consequently the succeeding picosecond pulse, 13ns after the main pulse is only amplified to well below 5% of the main pulse's energy [52]. Thus the amplifier acts as a pulse picker. We estimate that the second pulse only generates less than three orders of magnitude lower pulse energy at the third harmonic frequency and even less energy at the fifth harmonic, so it can be neglected in interpreting the data. Possible pre-pulses that could disturb the quantum system are eliminated by the single-pass design.

2.1.3 Pulse characterization

To precisely determine the temporal and spectral pulse profile as well as its phase we employ the technique of frequency resolved optical gating (FROG) [53]. Our polarization gated FROG setup consists of a polarization-gated autocorrelator and a Czerny-Turner-spectrometer with 500 mm focal length (see Fig. 2.3). The spectrometer features a 1800 l/mm holographic grating[9], that is tunable for the whole spectral region shorter than 1000 nm and a variable slit, optimized for a spectral resolution of 0.015 nm at 633 nm.

The Fourier transformed spectral resolution corresponds to a maximum temporal analysis width of ±43 ps. For each delay τ of the probe pulse, we record the spectrum of the PG signal

$$I_{PG}(\tau,\omega) \propto \left| \int_{-\infty}^{\infty} E(t-\tau)\cdot|E(t)|^2 \cdot e^{-i\omega t} dt \right|^2 \qquad (2.1)$$

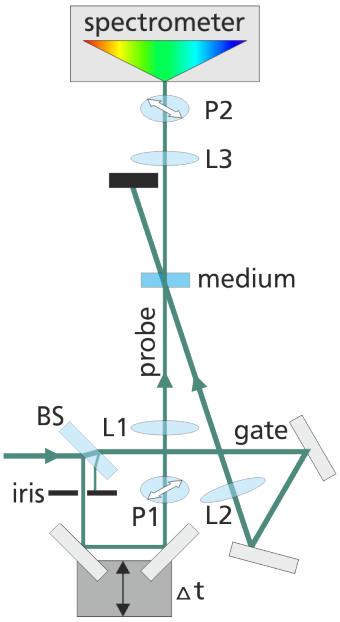

Figure 2.3: Schematic representation of the FROG setup

on a 3000 pixel CCD camera[10]. The width of the spectrum corresponds to a Fourier transformed temporal resolution of $\delta\tau$ =78 fs, while the stepper motor driving the delay stage is capable of a five times higher resolution.

To reconstruct the electric field temporal and spectral envelope, as well as its respective phases, we adapt an open access FROG-Code[11] to our measurement device [B5]. This code is based on a square 256 pixel matrix that represents the electric field amplitude $A_{sig} = \sqrt{I_{PG}}$. The algorithm is capable to reconstruct the

[9] GH50-18V, Thorlabs
[10] LC1, Thorlabs
[11] Trebino-Group Code, FROG v1.2.0 (19.9.2013) http://frog.gatech.edu/code.html

FROG signal of complex test pulses even with up to 10 % RMS noise on the raw data (resulting in approximately 0.8 % RMS noise on the final grid[12]). The RMS difference is $G^{(1000)} < 3 \cdot 10^{-3}$ $(1 \cdot 10^{-4})$ for the spectrogram and $< 3\,\%$ of the peak intensity for the intensity envelope. The phase is reconstructed with a RMS deviation of $< 0.13\pi$.

For a typical laser pulse, the reconstructed FROG signal A_{recon} as well as the difference of the reconstruction with respect to the measured data are shown in Fig. 2.4 (a) and (b).

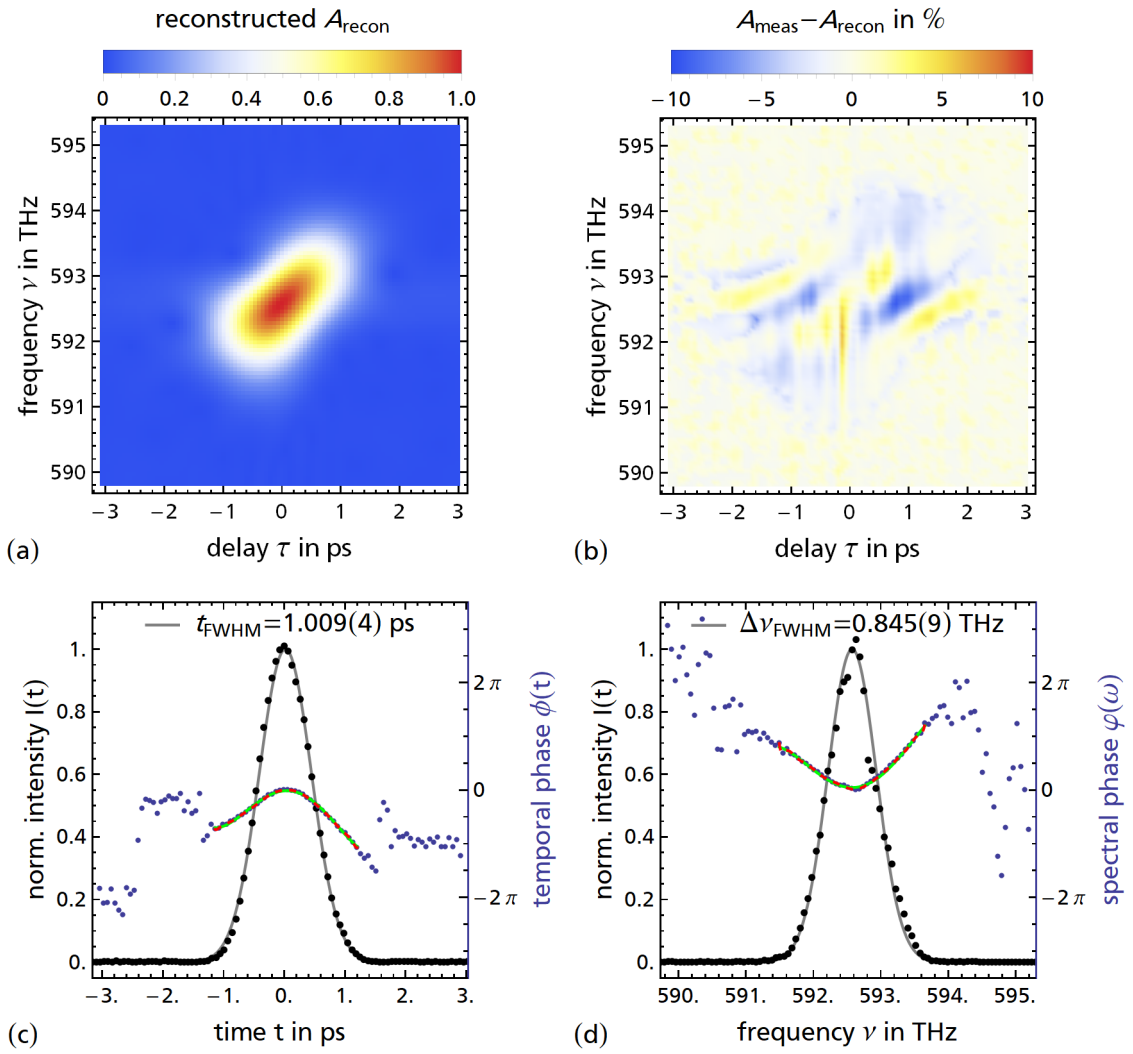

Figure 2.4: FROG signal (a) and difference between the measured and reconstructed FROG signal (b) of a typical laser pulse without re-compression. (c): Temporal intensity envelope in black, together with a Gaussian fit, as well as the temporal phase (blue) together with a polynomial fit of fifth and 15th order (overlaying green and red dashed lines). (d): Spectral power density and spectral phase with the respective fits (same colors as c). (For better visibility only the central 70 × 70 points of A_{recon} are shown.)

From the reconstructed temporal intensity envelope we retrieve the pulse

[12]We use additional low-pass filtering and a 2D wavelet noise reduction to 0.25 % RMS.

length by fitting of a Gaussian or (when not appropriate) by taking the full width at half maximum (FWHM) of the envelope.
The pulse characterization is used to tune the amplifier and OPO such that the pulses are as close as possible to a Gaussian laser pulse. Typically the time bandwidth product (TBP) of an uncompressed pulse then is in the range of 0.7..0.9, a factor of 2 higher than the TBP of a Fourier limited Gaussian pulse (0.44). The dispersion is caused by a dispersion block and the mirrors of the OPO ($\approx 0.4\,\mathrm{ps\,THz^{-1}}$) and the amplifier as well as other optical elements between OPO and experiment ($0.6\mathrm{ps\,THz^{-1}}$)[13]. These estimations correspond well with the group delay dispersion of $1.1(3)\,\mathrm{ps\,THz^{-1}}$, determined from the fits to the spectral phase in Fig. 2.4 (c)). That is why for uncompressed operation of the OPO a pulse with higher bandwidth exhibits a larger TBP also.

At the experiment the pulse energy fluctuates and shows a normal distribution with a standard deviation of $\approx 10\,\%$ (during a 15 min acquisition time). We attribute this to about 3 % standard deviation of the pump pulse energy[14] and 0.7 ns of standard deviation in the build-up time of the pump pulse inside the laser. Those two effects result in a gain fluctuation of the amplifier. As we are operating the amplifier only slightly in saturation to avoid self-phase modulation and self focusing [52] also the large signal gain of the amplifier is nonlinearly affected by the fluctuations, resulting in an increased standard deviation of the output pulse energy. When the system is operated for several hours at high pump fluence we also record a trend towards lower pulse energy as the dye molecules are slowly but steadily destroyed by the UV light, decreasing the gain. We compensate this effect by increasing the pump power for constant gain.

For all measurements proceeding chapter 3, we sample the beam onto an AC coupled photo diode[15] and calibrate the photo diode signal with a pyroelectric energy sensor[16]. For the nonlinear experiments we then select only laser shots within a pulse energy range of typically $\pm 3\,\%$ around the desired mean pulse energy, thus drastically decreasing the standard deviation in fundamental intensity. Data of all laser shots is still recorded and can be used with different filters, when desired.

2.2 Conclusion

In this chapter the basic laser system and the data acquisition setup was described. This laser system was developed in parallel to the experiments towards resonantly enhanced, coherent frequency up-conversion, presented the following chapters. In each of the chapters 3-5, we give details on modifications with respect to the introduced basic setup, that were necessary to suit the preconditions of the respective experiment.

[13] see [M3] for a detailed investigation.

[14] A standard deviation of 2.2% was measured for the 2nd harmonic of the laser in [M5]. Due to the nonlinear intensity dependence of the sum-frequency generation to yield the 532 nm radiation, we estimate the standard deviation to be $\Delta W = 1.022^{1/3} - 1 = 3.3\%$.

[15] Becker & Hickl PDI-400-UV

[16] Ophir PE-50 (above $100\,\mu$J) and PE-9 (below $100\,\mu$J)

Chapter 3

Resonantly enhanced higher harmonic generation in a jet of argon atoms

3.1 Introduction

In chapter 1 we have derived how resonance enhancement can be used to enhance the otherwise very small nonlinear susceptibility of gaseous media for frequency conversion towards the VUV spectral regime. Such resonantly-enhanced frequency conversion is well known from low-order frequency conversion processes, driven by lasers of moderate intensities. In recent years there already have been some (but still quite few) experimental investigations of resonance enhancements in harmonic generation via bound atomic states. As early examples, we note the work by L'Huillier et al. [23] and Toma et al. [24]. The authors observed enhancement of particular harmonics for specific laser intensities, e.g. an increase in the yield of the n-th harmonic by exciting a dynamically shifted n-photon resonance. Barkauskas et al. [25] observed enhancement of high harmonics driven by rather long (200 ps) laser pulses, when the driving laser wavelength was tuned appropriately. The authors suggest, that phase matching effects or multi-photon resonances may lead to these enhancements. However, no definite explanation was given. Finally we mention a sequence of experiments by Ganeev et al. on pronounced enhancement of single harmonics in plasma plumes [26] by dynamically-shifted ionic resonances close to specific harmonics. However, in most of the above experiments resonance effects could not be systematically investigated requiring further experimental and theoretical work for detailed insight [54]. Furthermore, in most cases only single harmonics were enhanced, while excitation of n-photon resonances should also affect harmonics with order larger than n, as the higher order nonlinear polarizability $\alpha^{(n)}$ features the same possible multi-photon resonances as a lower order $\alpha^{(n-2)}$nonlinear [19].

However there are some limitations of the experimental parameters for multi-photon processes to actually dominate the harmonic yield. In the terminology of high intensity laser-matter interaction, a Keldysh parameter $\gamma = \sqrt{W_I/2\Phi_p}$ larger than unity is required to still observe multi-photon resonances in ionization. This corresponds to the limit, where the semi-classical tunneling time t_{tu} is larger than 4π times the cycle time of the electromagnetic field or $t_{tu} > 1/2\omega$. Furthermore the laser bandwidth must be sufficiently small to resolve single excited levels and benefit from the enhancement, as derived in the previous section.

In the following, we present systematic investigations of resonantly-enhanced harmonic generation up to a Keldysh parameter of $\gamma \geq 2.3$, involving pronounced

Stark shifts, and simultaneous enhancement of several harmonics with order higher than the resonantly driven multi-photon transition. The pulse duration of about one picosecond in combination with the higher frequency of the tunable visible radiation (compared to standard ultra-short pulse lasers with $\lambda > 700\,\mathrm{nm}$) permits us to generate EUV light already with lower order frequency conversion processes. The tunability of the laser system allows us to resolve the Stark shifts. The results presented here were published in Optics Express [51]. Graphics and parts of the text are adapted from this publication. The data is critically re-evaluated with the insight gained from subsequent experiments in our laboratory, resulting in slightly different values and uncertainties, however still within the confidence interval of the original publication.

3.2 Coupling scheme and experimental setup

For the experiment we tune the intense, picosecond laser pulses in the vicinity of the five-photon resonance $3p^6 \rightarrow 3p^5\,4s'^2[1/2]^\circ_1$. Fig. 3.1 shows a simplified version of the full level scheme (Fig. 1.3), including only dipole allowed levels close to a multi-photon resonance. For the experiment, we chose the $3p^5\,4s'^2[1/2]^\circ_1$ level (in opposition to to the slightly lower energetic $4s^2[3/2]^\circ_1$ level) as it exhibits a much higher transition dipole moment ($\mu^2_{4s',3p^6} = 21 \cdot 10^{-60}\,\mathrm{C^2/m^2}$ vs. $\mu^2_{4s,3p^6} = 6 \cdot 10^{-60}\,\mathrm{C^2/m^2}$) with respect to the ground state $3s^2 3p^6$ [41]. The $3p^6 \rightarrow 3p^5\,4s'^2[1/2]^\circ_1$ transition occurs at wavelength of $\lambda_5 = 104.8\,\mathrm{nm}$, so we expect the unperturbed five-photon resonance at a fundamental wavelength of $\lambda_1 = 524\,\mathrm{nm}$. In the experiment we expect resonantly-enhanced fifth harmonic generation of the driving laser radiation as well as harmonics of higher order (indicated by dashed arrows in Fig 3.1).

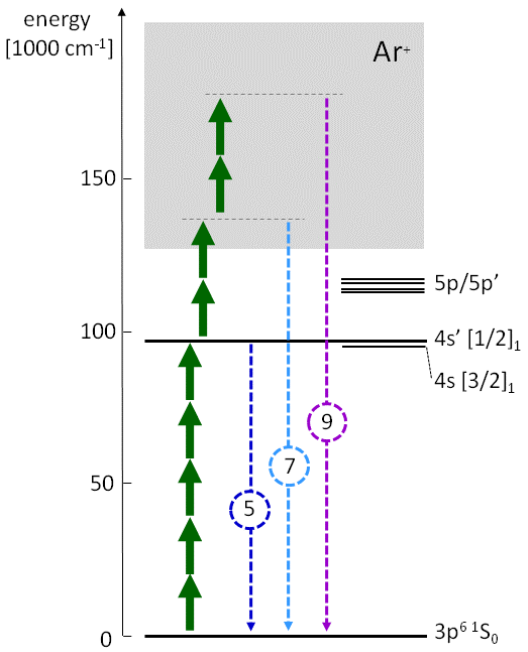

Figure 3.1: Coupling scheme in argon with relevant energy levels and generated harmonics. [51]

To gain high intensity, the laser system is optimized for a high pulse energy and operated without the two last spatial filters (PH3 and PH4 in Fig. 2.1) for lower loss. It provides tunable (ps) radiation pulses in the visible regime, with linear polarization. The amplified pulses have a Gaussian temporal envelope with a width of $\tau_p = 1.5(3)\,\mathrm{ps}$ (FWHM) at a time-bandwidth product of about 0.8.[1]

[1] For this experiment the FROG setup was operated with Chlorobenzene as a nonlinear medium, rendering the reconstruction of the pulse impossible (see appendix A.1). The pulse length is estimated from the raw spectrogram. This increases the error margin on pulse length and TBP.

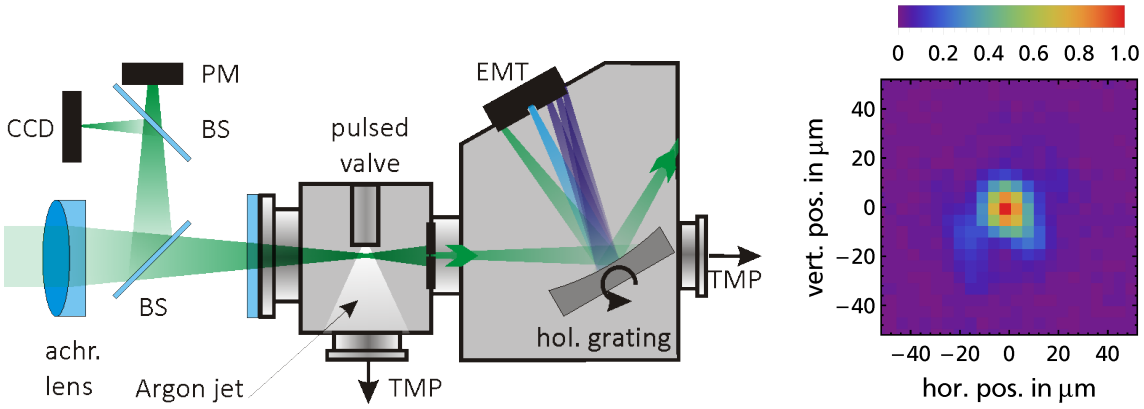

Figure 3.2: (a) Experimental setup (BS: beam sampler, PM: power meter, CCD: image sensor, TMP: turbo-molecular pump) [51] (b) Transversal intensity distribution in the focal plane as captured by the CCD.

In the experiment (see Fig. 3.2 (a)), we focus the laser beam by an achromatic doublet (focal length $f = 150\,\text{mm}$) into a pulsed gas jet of argon atoms, expanded through a pulsed nozzle[2] in a differentially pumped vacuum chamber. The Gaussian $1/e^2$ waist of the picosecond laser beam intensity in the interaction region is $w_0 = (14 \pm 2)\,\mu\text{m}$. In addition to the Gaussian portion of the focus, about one third of the pulse energy, covered by higher Fourier components of the transversal beam profile, is imaged outside the Gaussian slope (see blue areas in Fig. 3.2 (b)). With these data we calculate a possible peak intensity of$I_1 = 51(15)\text{TW/cm}^2$.
The harmonics, generated by the focused radiation inside the gas jet propagate into an evacuated monochromator[3]. The monochromator separates the harmonics and directs them onto an electron multiplier tube[4] for detection. The EMT is terminated with a voltage amplifier[5] before the amplified signal is digitized by means of an analog boxcar gated integrator[6] in combination with a analog to digital converter[7]. In parallel to acquisition of harmonic spectra, we carefully monitor the average laser pulse energy and the spatial beam profile to guarantee stable conditions in the interaction volume. The statistical spread in pulse energy is about 10 % FWHM.

3.3 Experimental results

With our tunable laser system, we are able to track the effect of resonance enhancement at the transition from the multi-photon to the tunneling regime by acquisition of the harmonic yield in the vicinity of the resonance with respect to fundamental wavelength and intensity.

[2]General Valve 009-0181-900, stagnation pressure 0.8(1) bar, orifice diameter 0.9 mm
[3]VM502, Acton Research, resolution $\delta\lambda = 0.1$ nm, 1200 l/mm holographic grating (iridum).
[4]EMT R595, Hamamatsu
[5]FEMTO DHPVA100, gain 10 dB, bandwidth 100 MHz
[6]Stanford Research SR250, 5 mV sensivity.
[7]National Instruments PCI-6220, 16 bit.

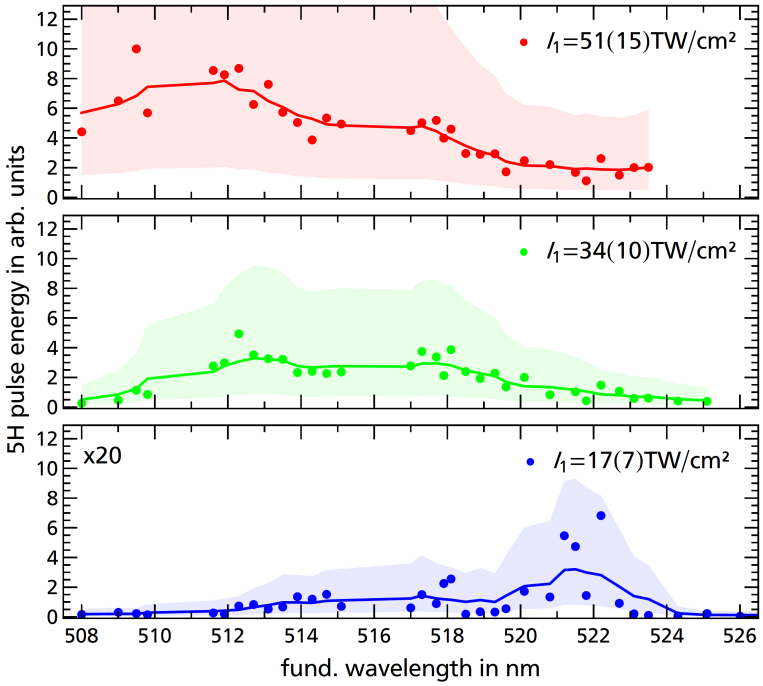

Figure 3.3: Yield of the fifth harmonic vs. driving laser wavelength for different fundamental laser intensities I_1. Raw data points after averaging 20 laser shots (dots) and a moving average of 9 data points (line). Shaded areas depict the uncertainty of the fifth harmonic energy due to parameter variations. For better visibility, the harmonic yield at I_1 =17 TW/cm² is scaled up by a factor of 20. The unperturbed five-photon-resonance is expected at 524 nm fundamental wavelength.

3.3.1 Intensity dependence of the resonance enhancement for FHG

To record the effective line shape of the dynamically shifted five-photon resonance, we monitor the intensity of the fifth harmonic frequency when tuning the wavelength of the driving picosecond laser pulse. Figure 3.3 shows such spectra, obtained for different laser intensities.
We superimpose a moving mean of 9 consecutive data points to smooth the spectral dependence of the raw data (dots) for better visibility. Due to slight variations in pulse length, focal spot size and average pulse energy for each data point, the raw data are prone to a possible relative variation of up to a factor of three (indicated by the colored area) with respect to the mean. At the lowest intensity of 17(7) TW/cm², the highest fifth harmonic energy is recorded slightly blue detuned from the resonance. In addition, a second, broader feature of high harmonic energy is visible at even shorter wavelength. At a laser intensity of 17 TW/cm², the excited state $4s'^2[1/2]_1^\circ$ (termed 4s' in the following) experiences a Stark shift of $\Delta W_{4s} \approx 100$ THz in the ponderomotive approximation (as of section 1.4), so the five-photon resonance wavelength moves towards shorter wavelengths. Due to the Gaussian temporal and transversal intensity distribution, the an averaging over all possible ΔW_{4s} from zero to the maximum value occurs. As a consequence, different portions of the beam experience resonance enhancement at different fundamental wavelengths $524 < \lambda_1 < 504$ nm. When we further increase the inten-

sity to $(34 \pm 10)\,\mathrm{TW/cm^2}$ and $(51 \pm 15)\,\mathrm{TW/cm^2}$, the shift and line broadening of the five-photon resonance becomes very pronounced. For the highest intensity at $51\,\mathrm{TW/cm^2}$, position of maximum VUV energy shifted by more than 10 nm with respect to $17\,\mathrm{TW/cm^2}$. This corresponds to a total shift of 55 THz. The shape of the mean curves seems to stretch proportionally to the fundamental intensity. If we take the right shoulder of this envelope as an indicator for the strength of the level shift, a proportionality between fundamental intensity and ΔW_{4s} is evident. One explanation, why the apparent line shape does not much stronger towards the position of the five-photon resonance at the peak intensity is the deviation of the transversal intensity distribution from the ideal Gaussian, with rather large areas at approximately 20% of the peak intensity. Another explanation are the rather large uncertainties in absolute intensity.

Given the spectral dependence of the fifth harmonic energy with respect to the fundamental wavelength we can anyway identify an intensity dependent optimal wavelength for harmonic generation. This wavelength minimizes the detuning and maximizes the efficiency for a given temporal and spatial intensity distribution. At this particular wavelength, we also expect an enhancement in higher harmonics compared to a wavelength of lower fifth harmonic yield.

The Stark shift in transition energy extracted from the data ΔW_e is of the same order of magnitude as the ponderomotive energy Φ_P, as predicted by theoretical calculations [50]. The strong intensity averaging effects inside the focal region together with the variation of the experimental parameters permit the estimation $\Phi_p \geq \Delta W_e \geq 0.25\Phi_p$.

3.3.2 Effect of the five-photon resonance on higher harmonics

To investigate this resonantly-enhanced multi-harmonic generation, we tune now the laser on and off the Stark-shifted resonances and compare the obtained harmonic spectra. Figure 3.4 (a) shows harmonic spectra for a laser intensity of 17 $\mathrm{TW/cm^2}$. In this case, the fifth harmonic yield exhibits a maximum at a wavelength of 522 nm (compare Fig. 3.3). If we tune the laser to a wavelength of 524 nm (off the Stark-shifted five-photon resonance, towards the unperturbed position), the harmonic spectrum shows a weak 5^{th} harmonic and a very weak 7^{th} harmonic of the driving laser (see Fig. 3.4 bottom). If we tune the laser now towards λ_1 =522 nm, the intensities of both the 5^{th} and 7^{th} harmonic increase by an order of magnitude due to resonance enhancement (see Fig. 3.4 middle). Thus, the five-photon resonance also enhances generation of a higher harmonic, generated from a nonlinear polarizability $\alpha^{(7)}_{(7\omega)}$. If we tune the laser further to a shorter wavelength around 510 nm, the yield of 5^{th} and 7^{th} harmonic decrease significantly (see Fig. 3.4 top). However, both harmonics are still slightly stronger than the harmonics, driven with the laser wavelength at 524 nm. We attribute this to the high possible shift of the 4s' level at the peak intensity of the pulse, already leading to the long tail of the Stark-shifted resonance towards shorter wavelength in Fig. 3.3. The effect of resonantly-enhanced harmonic generation becomes even better visible at a laser intensity of $51\,\mathrm{TW/cm^2}$, when more harmonics appear in the spectrum shown in Fig. 3.4 (b). At this intensity, we observed the highest fifth

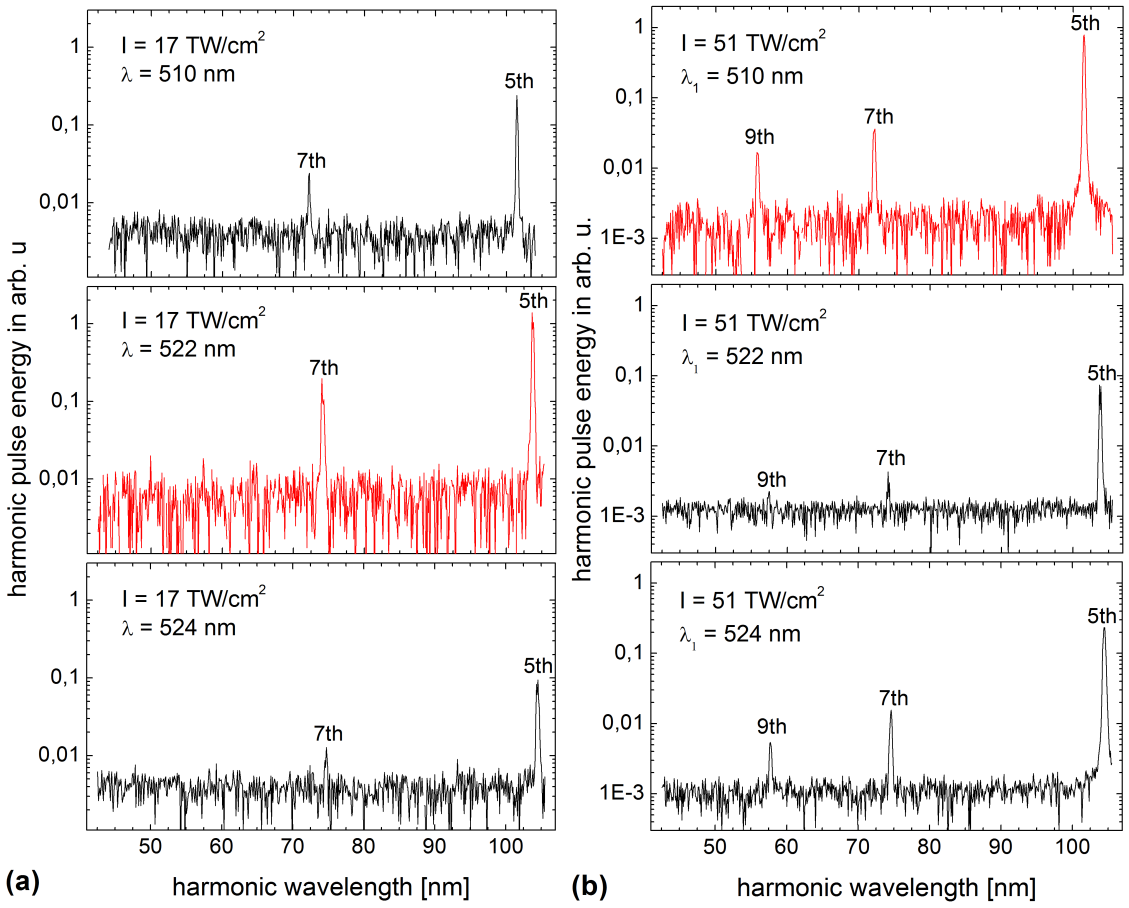

Figure 3.4: Harmonic spectra at (a) 17(7) TW/cm² and (b) (51±15) TW/cm² at λ_1 =524 nm, 522 nm and 510 nm. Lines depict raw data after averaging 20 laser shots, but without filtering. Red spectra are for the laser tuned to the wavelength of maximum enhancement.

harmonic yield at a wavelength of 510 nm (compare Fig. 3.3). When the laser is tuned to the unperturbed resonance position at λ_1 =524 nm, as well as for the former optimal wavelength $\lambda_1 = 522$ nm (at 17 TW/cm²), besides the 5th harmonic only rather weak 7th and 9th harmonics show up in the spectrum, as shown in Figs. 3.3(a,b). If we tune the laser towards $\lambda_1 = 510$ nm, the wavelength of optimal 5th harmonic yield, the 5th, 7th and 9th harmonic are enhanced by factors of 10, 9 and 7, when compared to excitation at $\lambda_1 = 522$ nm (see Fig. 3.4(b), middle).

The harmonic signals for excitation with a laser wavelength of 524 nm, shown in Fig. 3.4 (b) bottom) are slightly stronger compared to the harmonic signals obtained with a laser wavelength of 522 nm. We attribute this to a potential resonance enhancement from the energetically lower lying level $4s\,^2[3/2]^\circ_1$ (corresponding to an unperturbed five-photon resonance at 533 nm. The energy of this resonance is also being shifted up, passing the 524 and also enhancing the harmonic yield. Due to the four times weaker squared transition dipole moment $\mu^2_{4s,3p^6}$, the enhancement is still small compared to the 4s' level.

Comparing Figs. 3.4 (a) and (b), we conclude that (transient) resonance enhancement of multiple harmonics is possible. However at the high intensities nec-

essary to generate sufficient photons at the 7th and 9th harmonics, the inevitable Stark shift already covers several THz of frequency offset for a given excited level. To achieve enhancement at a given peak intensity, the laser wavelength λ_1 has to be adjusted accordingly. Even then, the resonance condition can not be satisfied for all intensities within the envelope of of a focused laser pulse. This shortcoming significantly reduces the possible enhancement for several orders of magnitude to about one order of magnitude in this case.

3.4 Conclusion

We demonstrated resonance enhancement in frequency conversion of picosecond laser pulses towards the EUV spectral regime. By tuning the central wavelength of the visible fundamental pulses, we investigated the conversion efficiency for various five-photon detunings from the $3p^6 \rightarrow 3p^5\,4s'\,^2[1/2]_1^\circ$ transition in argon. In each of the three recorded curves at different intensity, we identified a clear maximum in conversion efficiency, shifting towards shorter driving wavelength at higher intensity. This shift in excess of 50 THz is attributed to the Stark shift of the excited level and is found to be of the same order of magnitude as the ponderomotive potential Φ_p. We concluded that, the efficiency enhancement is due to a transient resonance enhancement, when the Stark-shifted level comes in (five-photon) resonance with the driving laser. Temporal and spatial averaging, as well as the pulse to pulse energy fluctuation is found to broaden the retrieved lineshape.

In a second experiment, we tuned the laser to the maximum of the lineshape for two different fundamental intensities I_1. In both cases we gain a significant enhancement of the pulse energy of multiple harmonics with respect to the "field-free" resonance position at 524 nm. At the highest intensity near 50 TW/cm^3. for the harmonics H5-H9 an enhancement of up to one order of magnitude was achieved by tuning to the position of maximal fifth harmonic yield. We pointed out, that the strength of the enhancement is limited by the transient nature of the effect. Stronger enhancements may be achieved by special shaping of the spatial and temporal distribution of the intensity, to reduce averaging effects.

The experimental data show, that resonant enhancement of multiple harmonics is feasible, even at intensities in excess of 10 TW/cm^2, when laser wavelength is matched to the (intensity dependent) position of the Stark-shifted atomic resonance. This resonance enhancement of multiple harmonics emphasizes the importance of intermediate resonances also in higher harmonic generation.

Chapter 4

Coherent control of frequency up-conversion towards short vacuum-ultraviolet radiation pulses

4.1 Introduction

The interaction of coherent radiation with matter at high (peak) intensity enables the investigation of interference effects that do not exist for incoherent radiation. We use the coherent properties of ultra-fast laser pulses at high intensity (TW/cm^2) to actively enhance or suppress the (nonlinear) generation of harmonic frequencies. "Coherent Control" in atomic or molecular systems is a prominent field in physics and chemistry [27, 55]. The method of "phase control" was introduced by Brumer and Shapiro in 1986 [56]. The basic concept of phase control is to drive two indistinguishable excitation pathways by a multi-color laser field (most commonly two laser beams). Control of the phase difference between the (two) respective fields, serves to drive the total transition probability such, that the two transitions add constructively or destructively. In chemistry, reactions that start from a specific excited state can be significantly enhanced or suppressed. In nonlinear optics the method of coherent control can be applied to enhance or suppress the generation of a specific harmonic frequency. However up to date there are only a few experiments in this field. To our knowledge before our work, the experiments of Karapanagioti [28], Xenakis [29] and Münch [30] are the only demonstrations of phase control in harmonic generation. In 2016 finally the scheme of phase control has been implemented with high selectivity in coherent control of femtosecond above threshold photo-emission [57, 58], paving the way towards even faster electron microscopes, and tabletop particle accelerators as well as intense x-ray sources [59].

Resonance enhancement is one way to enhance the usually very low conversion efficiency of a highly nonlinear process. At the same time interference of two indistinguishable frequency conversion pathways is possible, although they are driven by fields of different fundamental frequencies. The combination of resonance enhancement and coherent control finally empowers the experimenter with an additional control parameter. By control of the phase relation it is possible to enhance this process or suppress possible loss channels in another undesired frequency mixing scheme and thus exhibits a promising technique in suitable conditions.

We will show an example, where two different frequency mixing processes

yield the same output frequency. We control the phase relation between the driving radiation fields from constructive to destructive interference between the two conversion processes. To select two specific pathways in frequency up-conversion of picosecond radiation pulses towards the VUV regime, we employ resonantly enhanced frequency mixing. So far, the few previous works on phase control in nonlinear optics were all carried out with nanosecond or even longer pulses, so our results are the first to apply ultra-short (ps) laser pulses yielding strong control of high-order frequency conversion processes towards short VUV wavelengths.

The demonstration of high visibility at short pulse durations (and extended bandwidth) is of interest for applications in ultra-fast nonlinear optics, e.g. higher harmonic generation. This chapter will discuss the requirements to achieve the large visibility by careful matching the two conversion processes in in space and time. We will also explore the onset of limitations arising from the high intensity necessary to drive the higher order processes as well the large bandwidth carried by an ultra-short pulse. The research on this topic lead to a publication in Physical Review A [60].

4.2 Coupling scheme

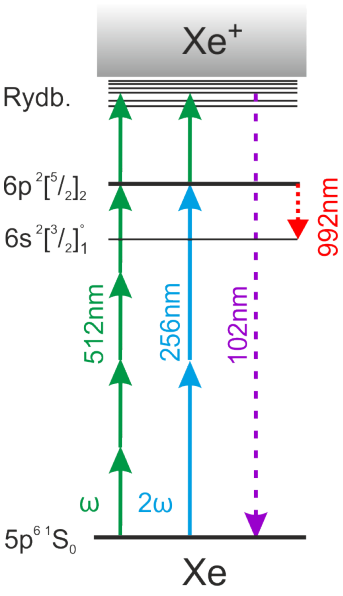

Figure 4.1: Coupling scheme with relevant energy levels and transitions (adapted from [60])

In our experiment we investigate coherent control of frequency up-conversion in a supersonic jet of gas atoms. We choose the noble gas xenon as a medium because it offers the lowest transition frequencies of the stable rare gas atoms and thus also exhibits large susceptibilities for frequency conversion towards the VUV and XUV spectral regime.

The excited state $6p\,^2[5/2]_2$ can be addressed from the ground state $5p^6\,^1S_0$ of xenon either via four photons of a laser at $\lambda_F = 512\,\text{nm}$ or via two photons of the second harmonic[1] (SH) of this radiation at $\lambda_{SH} = 256\,\text{nm}$ (see Fig. 4.1). Consequently the medium features four-photon resonant fifth harmonic generation and two-photon resonant four-wave mixing, both yielding VUV radiation at $\lambda_{VUV} = 102.4\,\text{nm}$. The additional fifth photon mixed with the coherence generated between $6p\,^2[5/2]_2$ and the ground state couples the excited state with the dense manifold of Rydberg states. This on the one hand further enhances the frequency conversion process, on the other hand generates dispersion for the fifth harmonic radiation field. For simplicity, in the following we will first neglect the Rydberg coupling and discuss the possible effects later. In case of resonant excitation, there is another process driven by the two excitation pathways: Population is excited to

[1] To distinguish this two-color pump experiment from the single-color pump experiments of chapters 3 and 5, we term the two independently controlled pump fields $E_F (= E_1)$ and E_{SH}.

the $6p\,^2[5/2]_2$ level and can decay with a lifetime of 35 ns [61] towards the $6s^2[3/2]_1^\circ$ level, yielding laser induced fluorescence (LIF) at a wavelength of 992.3 nm [62]. Due to the long lifetime, the decay during the interaction time can be neglected and the population dynamics is dominated by coherent optical excitation.

The coherent excitation also leads to "coherent population return" (CPR) [63–65]. When the detuning from resonance is much bigger than the laser pulse bandwidth, population is only transiently transferred to the excited state and returned back to the ground state after the pulse. So LIF, (occurring mainly after the interaction) is only expected for small detuning from multi-photon resonance.

4.2.1 Quantum interference in frequency conversion

We will first examine the frequency conversion yield towards the VUV radiation with respect to the relative phase φ_F between the incident fundamental and second harmonic beams. For simplicity we first consider the fundamental pulse as monochromatic, linearly polarized field with the magnitude $\widetilde{E}_F(x,y,z,t) = E_F(x,y,z)\cdot e^{-i(\omega_F t - k_F z + \varphi_F)} + c.c.$ propagating in z-direction with the complex amplitude of the Gaussian beam $E_F(x,y,z)$. Considering only the fundamental field, the part of the nonlinear polarization oscillating at the fifth harmonic frequency then reads

$$\widetilde{P}^{(5)}_{5HG} \propto \chi^{(5)}_{5HG}\cdot(E_F^5\cdot e^{-i(5\omega_F t - 5k_F z)}\cdot e^{-i\cdot 5\varphi_F} + c.c.) + O(E_F^7). \tag{4.1}$$

With the respective component $\chi^{(5)}_{5HG}$ of the fifth order nonlinear susceptibility. Considering also the second harmonic field $\widetilde{E}_{SH}(x,y,z,t) = E_{SH}(x,y,z)\cdot e^{i(\omega_{SH}t - k_{SH}z)} + c.c.$, an additional term

$$\widetilde{P}^{(3)}_{FWM} \propto \chi^{(3)}_{FWM}\cdot(E_{SH}^2\cdot e^{-i(2\omega_{SH}t - 2k_{SH}z)}\cdot E_F e^{-i(\omega_F t - k_F z)}\cdot e^{-i\varphi_F} + c.c.) + O(E_F^3\cdot E_{SHG}^3) \tag{4.2}$$

for sum-frequency mixing of two SHG photons and one fundamental photon arises, scaling with the component $\chi^{(3)}_{FWM}$ of the third order nonlinear susceptibility. Here we choose the second harmonic phase as a reference for φ_F.

Assuming an optically thin medium, permitting perfect phase matching and negligible pump depletion, we can calculate the field at $5\omega_F$ by spatial integration in z. For negligible phase mismatch inside a homogeneous medium of length L and a Raleigh length $z_R \gg L$, there is no phase acquired during integration, so the integral reduces to:

$$\widetilde{E}_{VUV} \propto \int_{-L/2}^{L/2} \widetilde{P}^{(5)}_{5HG} + \widetilde{P}^{(3)}_{FWM}\,dz = (\widetilde{P}^{(5)}_{5HG} + \widetilde{P}^{(3)}_{FWM})L \tag{4.3}$$

and the VUV intensity reads

$$\begin{aligned} I_{VUV} &\propto L^2(P^{(5)}_{5HG} + P^{(3)}_{FWM})\cdot(P^{(5)}_{5HG} + P^{(3)}_{FWM})^* \\ &= L^2\left[|\widetilde{P}^{(3)}_{FWM}|^2 + |\tilde{P}^{(5)}_{5HG}|^2 + 2|\tilde{P}^{(5)}_{5HG}\cdot\widetilde{P}^{(3)}_{FWM}|\cdot\cos(4\varphi_F + \phi_\chi)\right] \end{aligned} \tag{4.4}$$

with the (complex) polarization amplitudes $P^{(3)}_{FWM} = \chi^{(3)}_{FWM} \cdot E_F E^2_{SH}$ and $P^{(5)}_{5HG} = \chi^{(5)}_{5HG} \cdot E^5_F$ and the (atomic) phase difference ϕ_χ of both induced polarization at $\varphi_F = 0$. This phase is the argument of the product $(\chi^{(3)}_{FWM})^* \cdot \chi^{(5)}_{5HG}$ and hence a medium specific quantity. We note, that in our experiment we cannot determine the phase difference φ_F of the fields directly, so it is impossible to obtain ϕ_χ. However we can determine the difference ϕ_χ-ϕ_μ of two simultaneously acquired signals (with the second signal having the phase offset ϕ_μ).

4.2.2 Quantum interference in excited state population

We also consider the fluorescence from the excited state $6p\,^2[5/2]_2$, which is proportional to the excited state population after the interaction. The probability

$$\begin{aligned} W_{6p} \quad \propto \quad & |\mu^{(4)} E^4_F|^2 + |\mu^{(2)} E^2_{SH}|^2 \\ & +2|\mu^{(4)}\mu^{(2)} E^4_F E^2_{SH}| \cdot \cos(4\varphi_F + \phi_\mu). \end{aligned} \tag{4.5}$$

for excitation involves the dipole-moments for two-photon ($\mu^{(2)}$) and four-photon ($\mu^{(4)}$) transition [66]. With $\phi_\mu = \arg(\mu^{(4)*}\mu^{(2)})$ the phase difference of the two complex multi-photon transition moments. Both signals oscillate four times for a phase shift of $\Delta\varphi = 2\pi$ for the fundamental radiation. In contrast to the excitation probability, the nonlinear polarizations for harmonic generation involve additional atomic levels above the $6p\,^2[5/2]_2$ state[2]. In our case the dense manifold of Rydberg states is coupled by the additional photon, possibly affecting Δ_χ and leading to a finite shift $\phi_\chi - \phi_\mu$ in LIF and VUV interferograms.

4.2.3 Conditions for maximal control

To maximize the degree of control over the generated VUV pulse energy

$$W_{VUV} \propto \int_{-T}^{T} \Big| \int_{A_t} \int_{-L/2}^{L/2} (\widetilde{P}^{(5)}_{5HG} + \widetilde{P}^{(3)}_{FWM})\, dz\, dx\, dy \Big|^2 dt \tag{4.6}$$

we now have to match the nonlinear polarizations for four-wave mixing and fifth harmonic generation or the four- and two-photon excitation probabilities respectively in all three spatial and the temporal domain. From the simplified equation 4.4 we already see, that for maximum interference visibility the absolute value of $P^{(5)}_{5HG}$ and $P^{(3)}_{FWM}$ have to be equal. This condition is essential in all spatial dimensions. We can only adjust the spatial intensity distribution of the beams by choosing appropriate lenses and beam waists. If we assume two perfectly collinear Gaussian beams for fundamental and second harmonic,

[2]The excited state population after the pulse is given by the temporal integral of the excitation probability. In the limit of low multi-photon Rabi frequencies $\Omega^{(4)}_F \cdot T \ll 1$, $\Omega^{(2)}_{SH} \cdot T \ll 1$ and low detuning from the 4-photon resonance (i.e. no Rabi flopping), that is also much lower than the detuning from all other intermediate states $\Delta_{4p} \ll \Delta_i$ (no excitation to intermediate states), the population dynamics of the excited state vary approximately linear in time. Thus the population of the $6p\,^2[5/2]_2$ level is proportional to W_{6p} in equation 4.5.

the optimal ratio of beam radii are $w_0(\lambda_F)/w_0(\lambda_{SH}) = \sqrt{2}$, such that

$$I_F^4(x,y,z)/I_{SH}^2(x,y,z) = const. \tag{4.7}$$

for $z = 0$. This also guarantees for the same Rayleigh length $z_r(\lambda) = \frac{\pi w_0^2(\lambda)}{\lambda}$ for both beams, so condition (4.7) is automatically fulfilled along the whole laser beam path. Also Gunawardena et. al. achieve highest visibility [67] (for two-photon vs. one-photon quantum interference) at this optimal value. This condition at the same time also maximizes the visibility of the interference in equation 4.5, resulting in maximal control of the excitation probability towards the $6p\,^2[5/2]_2$ level.

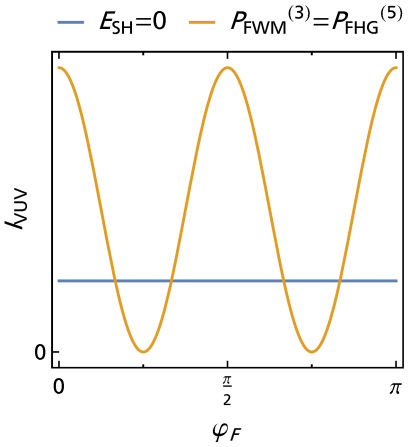

Figure 4.2: VUV intensity without SH field (blue) and for optimal conditions (orange)

While perfect phase matching $5k_F(z) = k_{VUV}(z) = 2k_{SH}(z) + k_F(z)$ is possible in vacuum, in a collinear geometry inside an isotropic medium, the excited states necessarily introduce dispersion, such that $2k_{SH}(z) > 4k_F(z)$ as long as both, ω_F and ω_{SH} are below the first one-photon transition frequency ω_1. We can define a propagation phase

$$\varphi_{prop}(z) = \frac{1}{4}\int [2k_{SH}(z) - 4k_F(z)]\,dz \tag{4.8}$$

additional to the intended control phase φ_F, that enters the cosine in equation 4.4. As φ_{prop} is z-dependent, it will lead to constructive interference at the beginning and destructive interference at the end of the medium, when $\varphi_{prop}(z=\infty) = \frac{\pi}{2}$. This condition limits the maximum gas density such that $\varphi_{prop}(z=\infty) \ll \frac{\pi}{2}$. It also prevents us from applying phase control inside a hollow core optical waveguide, as this tight confinement imposes additional positive dispersion which cannot be compensated below the first atomic resonance of the confined gas (see chapter 5).

The conventional phase mismatch $\Delta k_{VUV} = 5k_F(z) - k_{VUV}(z)$ however imposes no serious limit to coherent control. Only the absolute signal but not the relative interference pattern is affected by a finite phase mismatch Δk_{VUV}. We will therefore limit our discussions to the relative quantity visibility:

$$v = \frac{I_{max} - I_{min}}{(I_{max} + I_{min})} \tag{4.9}$$

This quantity is a measure of the degree of control possible on the desired process.

4.3 Experimental Setup

The experimental setup (see Fig. 4.3) is as follows: We tune the laser system to the four-photon resonance at $\lambda_F = 512\,\text{nm}$ and generate a second, phase locked beam of the second harmonic frequency inside a beta-Barium-Borate (BBO) crystal.

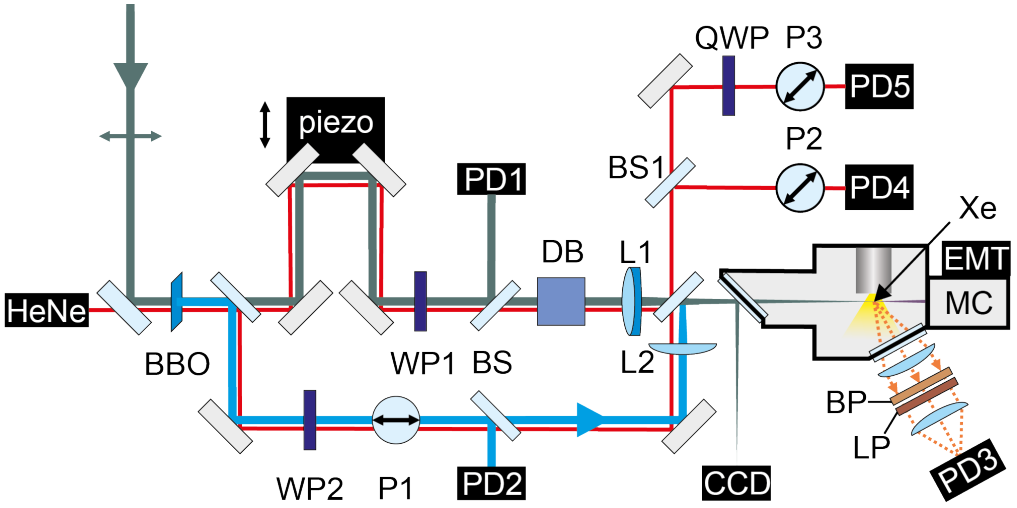

Figure 4.3: Schematic diagram of the setup for phase controlled fifth harmonic generation. (WP: half wave plates, QWP: quarter wave plate, BS: beam sampler, DB: dispersion block, L: lenses, P: polarizers, PD: photo diodes, BP: band-pass filter, LP: longpass filter, MC: vacuum monochomator, EMT: electron multiplier tube, Xe: jet of xenon atoms). The small double-arrows depict the polarization of laser fields and polarizers.(adapted from [60])

A Mach-Zehnder interferometer serves to tune the relative phase φ_F of the fundamental radiation (at frequencyω_F), before recombining the two laser beams inside the interaction region. We optimize the laser system for typical amplified pulse energies of up to 200 μJ at a pulse duration of 1.15 ps (FWHM) and a bandwidth of 0.66 nm (FWHM). The group delay acquired inside the OPO and during the propagation through PDA and spatial filters is not compensated[3], so the pulses are similar to the one shown in 2.2 with a residual group delay dispersion of $\approx 1\,\mathrm{ps}\cdot\mathrm{THz}^{-1}$. The frequency doubling process towards λ_{SH} =256 nm inside the BBO crystal (length 500 μm) in type I SHG. For phase control, the phases of the two laser beams have to be phase-locked to each other for the whole pulse duration. The phase distortions that can occur during frequency doubling due to back conversion or self-phase modulation, will reduce the contrast of the interference. We avoid such effects by using a thin BBO crystal and driving it within the pulse energy range of quadratic intensity dependence $I_{SH} \propto I_F^2$. Another possible issue destroying the phase relation is a frequency detuning between the four-photon and the two-photon process. This detuning occurs, when phase mismatch inside the BBO crystal is used on purpose to attenuate the second harmonic beam. The result is a shifted central frequency of the harmonic and distortion of the spectrum. A frequency detuning results in a temporal phase [53] $\phi_t = 2\pi\Delta\nu\cdot t$, so the actual phase between the two radiation fields is varying temporally, averaging out the interference signature. We therefore optimize the phase matching of the BBO before each measurement.

Inside the interferometer, the second harmonic propagates along the lower arm of the setup, passing a variable attenuator (zero order half wave plate (WP2)

[3]We repeated selected measurements also with Fourier limited pulses, yielding virtually the same results, but with about 10% lower visibility due to imperfect spatial overlap).

and an α-BBO polarizer (P1)) to adjust the intensity of the second harmonic in order to match the strength of the two frequency conversion pathways. To achieve temporal overlap and phase control, the fundamental pulses propagate along the upper arm of the setup, which contains a variable delay line[4] with a piezo actuator. A stepper motor is used to achieve temporal overlap, while a piezo stage is used for phase control afterwards. To maximize interference, we align the polarization of the fundamental radiation parallel to the second harmonic by an achromatic half-wave plate (WP1).

Due to the short wavelength, optical elements within the SHG interferometer arm impose an excess group delay dispersion (GDD) of 0.076 ps·THz^{-1}. The dispersion leads to wavelength-dependent delays of the fundamental and second harmonic pulses (i.e. a different temporal phase), reducing the interference visibility by temporal averaging. To restore the "phase locked" condition, the fundamental pulse has to be dispersed with a GDD of 0.038 ps·THz^{-1} . We achieve this by a dispersion block (DB[5]) placed in the fundamental arm of the interferometer.

To drive the nonlinear process, we focus both radiation beams into a jet of xenon atoms, expanded through a pulsed nozzle[6] in a differentially pumped vacuum chamber. The laser foci are placed as close as possible (less than 1 mm) to the nozzle, resulting in an estimated gas density of about 10^{17} cm^{-3} [68].

We use a f=250 mm achromatic lens (L1) to generate a focal spot of 45 μm·39 μm (hor. and vert. $1/e^2$-radius) for the fundamental and a f=300 mm fused silica lens (L2) to generate a focal spot of 39 μm · 23 μm for the second harmonic in the interaction region. Our actual spot size ratio of 1.12 / 1.41 (hor. / vert.) is close to the optimal value of $\sqrt{2}$ (from eq. 4.7). The difference in (averaged) Rayleigh length for the two beams ($z_r(\lambda_F) = 11$ mm and $z_r(\lambda_{SH}) = 12$ mm) is below 10%. The resulting change in relative phase φ in longitudinal direction due to the different Gouy phases of the beams is limited to a negligible $|\delta\varphi| < 6$ mrad at either extend of the atomic jet (at $z \approx \pm 0.8$ mm).

We note that the two beams should overlap not only in the focus, but also propagate perfectly collinear, to avoid spatial averaging over regions with varying intensity ratio. To minimize the angle between the two beams, during alignment we also monitor the beam positions approximately 30 cm after the focus on another CCD camera. We adjust the angle of the SHG beam entering L2 to overlap the foci and the beam position on L2 to overlap the far field intensity distributions.

For optimal visibility at a fundamental pulse energy of 42 μJ we attenuate the second harmonic pulses to an energy of 87 nJ to match the nonlinear polarization of four-wave mixing and fifth harmonic generation.

Parallel to the experiment, we monitor these pulse energies on calibrated photo detectors (PD1 & PD2)[7]. The intensity distribution of each driving field within the

[4]The delay stage is a flexure stage (Thorlabs NFL5DP20/M) enabling for 20 μm of piezo driven travel with nm resolution for phase control, stacked onto a OWIS Limes 122 linear stage modified with a low vibration 5 phase stepper motor (Orientalmotor) enabling for 50 mm of travel with micrometer resolution (to achieve temporal overlap)

[5]2x Thorlabs LSM03DC - VIS, (H-ZLAF52 glass, total length 35.6 mm)

[6]General Valve 009-0181-900, stagnation pressure 1 bar, orifice diameter 0.9 mm

[7]Becker&Hickl PDI-400 UV

interaction volume is monitored on a CCD sensor[8], by sampling a small portion of the beams before entering the vacuum setup.

We spatially separate the generated VUV radiation from the driving beams by a vacuum monochromator[9] (MC) and detect it by an electron multiplier[10]. The signal from the EMT is amplified[11] and sampled by boxcar gated integrator[12].

We also record a second signal, the laser-induced fluorescence from xenon atoms excited to the 4-photon resonant intermediate state. Excited atoms decay towards the lower lying $6s^2[3/2]_1^\circ$ state, emitting photons with a wavelength of 992.3 nm [62]. We collimate the light by a lens system with focal length f = 75 mm orthogonal to the laser beam and the xenon jet. The LIF signal is separated from stray light by a low-pass filter LP[13] , before the photons are focused onto a photo diode for detection. The signal is amplified by a current amplifier and thereafter sampled[14] for further data processing.

A crucial point for coherent control is the perfect control and measurement of the relative phase. We determine the path length of the interferometer (see Fig. 4.3) with a Helium-Neon (HeNe) reference laser[15] and observe it to fluctuate more than 20 nm (peak-peak) on the timescale of less than a minute due to vibrations of vacuum pumps, chillers and the solenoid valve. With this limited phase accuracy the maximum visibility is already limited to below 90 %. We therefore collinearly couple the vertically polarized laser through the interferometric setup and precisely measure the relative phase between the two driving radiation fields about 10 μs before each laser pulse. The optical setup is designed such that the beams coming from the two interferometer arms exit the Mach-Zehnder setup at the beam combiner just before the vacuum setup, so that all delays by moving parts and even density modulations by acoustic waves are captured.

The achromatic half-wave plate serves to turn the polarization of the beam traveling along the optical delay stage, resulting in orthogonal polarization after the interferometer. We separate the reference beams from residual pulsed radiation by a colored glass filter and project the crossed polarization onto a common polarization axis of 45° by a Glan-Taylor polarizer (P2). Thereafter we detect the interferogram on a photo diode (PD4). By inserting a quarter-wave-plate (QWP) into the other half of the beam, transmitted through the beamsplitter (BS1) we retard just the horizontally polarized beam (that has traveled along the optical delay stage) by a quarter wave. The second interferogram recorded by the second set of polarizer and photo diode (P3, PD5) then is shifted in phase by 90°, enabling quadrature detection of the optical delay and resolving ambiguous information at the minima and maxima of the individual interferogram signals.

[8]The Imaging Source DMM 315403ML with removed cover glass

[9]Home-made Seya-Namioka type [69] vacuum monochromator with HORIBA 522 00 250 grating

[10]Hamamatsu, EMT R595, stock voltage divider, linearized for pulsed operation with PDI400-UV for each gain setting by a reference measurement at 256 nm.

[11]FEMTO DHPVA-100

[12]SRS SR250, digitized by National Instruments PCI-6221

[13]Thorlabs LP900, with a suppression of 10^{-6} for the driving laser and VUV wavelengths

[14]amplifier: FEMTO DLPCA-200; digitizer: National Instruments PCI-6221

[15]Melles-Girot 05-LRH/P-151, wavelength stability < 0.004 nm

Processing both interference signals, we obtain the path difference in the Mach-Zehnder setup with an absolute accuracy better than 5 nm, corresponding to a phase accuracy[16] of $\Delta\varphi_F = 2\pi \cdot 10^{-2}$. This accuracy is independent from the displacement of the piezo driven delay stage. Thus, our setup permits interferometrically stable and continuously controlled phase variations corresponding to pulse delays of more than 110 fs.

For this type of phase measurement it is crucial to maintain constant ambient gas density. Otherwise a higher density leads to an increase in dispersion (between 512 nm and 256 nm), effectively retarding the SHG pulse with respect to the fundamental. As the temperature is subject to faster changes than the ambient pressure, we calculate the dispersion of the optical path difference Δl_{opt} in our setup with an arm length of $L_a = 0.83$ m with respect to the temperature T

$$\frac{\partial \Delta l_{opt}}{\partial T} = \frac{\partial}{\partial T}\left(\sqrt{1+\chi^{(1)}(\omega,T)} - \sqrt{1+\chi^{(1)}(2\omega,T)}\right) L_a$$

assuming an ideal gas at constant atmospheric pressure p, such that $\chi^{(1)}(\omega,T) \propto N(T) = {}^{p}/_{k_B T}$ with the number density $N(T)$ and the Boltzmann constant k_B. Using the Sellmeier equation for dry air [70], we get a delay dispersion of $71\,{}^{nm}/_{K\,m}$ at room temperature. This dispersion can not be measured by the reference laser, so it has to be minimized otherwise. By encasing the Mach-Zehnder setup inside a plastic housing, we achieve a temperature fluctuation of below ±0.1°C corresponding to a maximum ±6 nm of optical length fluctuation of the interferometer arms during the measurement time.

4.4 Spectroscopy

To determine the resonance position at a given intensity of SH and fundamental radiation, we carry out intensity resolved multi-photon spectroscopy. We acquire the intensity dependence of the fifth harmonic for 20 fundamental wavelength λ_F between 510 nm and 515 nm and combine them to yield intensity resolved multi-photon spectra[17]. The line shape of the resonance enhancement of fifth harmonic generation for three driving peak intensities driven by the fundamental field at central wavelengths between 510 and 515 nm is shown in Fig. 4.4 (a). A shift of the line shape towards lower wavelength (higher energy) is evident. Therefore we extract the position of maximal efficiency by Gaussian fits to the spectra up to a fundamental intensity of $I_F = 2.2\,\mathrm{TW/cm^2}$. The centers of the Gaussian fit are shown in 4.4 with error bars, representing the standard deviation of the fit. We note that for a fundamental peak intensity above $I_F = 0.7\,\mathrm{TW/cm}$, the line shape starts to become asymmetric. The peak positions of an empirical asymmetric fitting function (shown dashed in Fig. 4.4(a)) are shown in black and gray in Fig. 4.4 (b). To determine the resonance shift, we fit a linear function to the

[16] The phase measurement is explained in detail in [M1]

[17] The spectra together with detailed information on the methodology can be reviewed in [B4]. The data of Fig. 4.4 was measured together with Fabian Cipura and re-evaluated for this work.

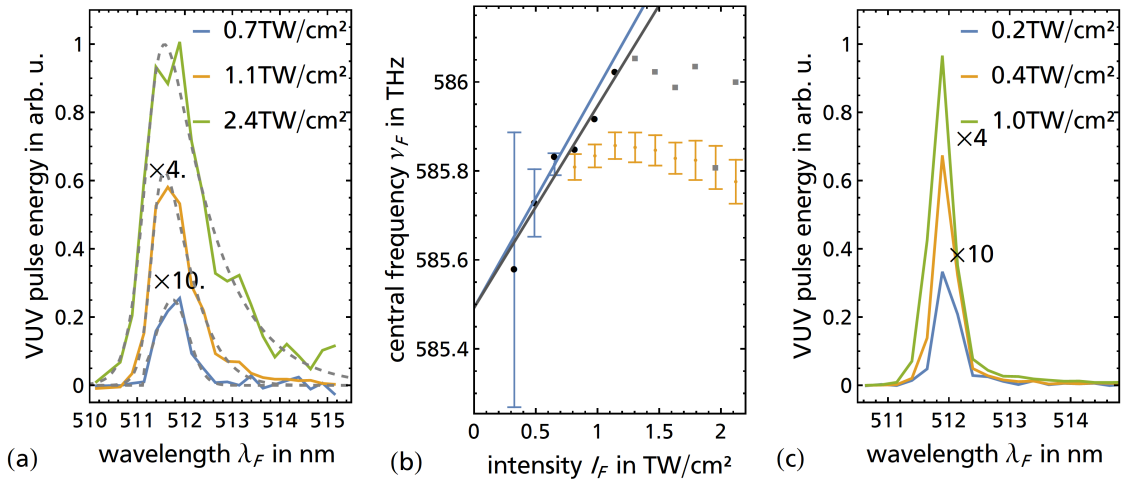

Figure 4.4: Intensity dependent central frequency of the resonance enhancement in xenon. Figure a) shows the line shape of 4-photon resonant fifth harmonic generation at three fundamental intensities. The intensity dependent position of highest efficiency is shown in Figure b) derived by fitting of a Gaussian (points with error bars, showing the fit's standard uncertainty). The peak positions of a empirical Gaussian function multiplied with a logistic sigmoid (superimposed for the three spectra in (a)) are shown as black and gray dots. Linear fits to the data are shown in the respective color of the processed data set. Figure c) shows the enhancement line shape in two-photon resonant third harmonic generation driven by the SH field near $\lambda_{SH} = 265$ nm, but referenced to the fundamental wavelength.

central frequencies of the Gaussian fits (blue data points) as well as the black portion of the peak positions, each starting from the unperturbed resonance position at 585.5 THz fundamental frequency (512.08 nm). Both slopes are similar, indicating a resonance shift of 2.0(5) THz / (TW/cm²) (Gaussian fits) or 1.8(5) THz / (TW/cm²) (peak position). This shift corresponds to $1/3$ of the ponderomotive potential Φ_p at the peak intensity of the fundamental radiation, so the retrieved value is plausible. Above 1 TW/cm² we are unsure what causes the change in line shape, therefore we cannot deduce the resonance shift. We limit our experiments to an intensity of $I_F \leq 1$ TW/cm², to stay within the linear regime of the shift. At 1 TW/cm² the fundamental wavelength $\lambda_F$for four photon resonance has shifted only 0.43 nm, so is still within the spectral width of the pulse. As a consequence, we can neglect the Stark shift of the 6p level in a simplified theoretical treatment.

The same measurement was conducted for 2-photon resonant excitation around 256 nm by the SH pulses. In addition to third harmonic photons at 85 nm we also record LIF from the $6p\,^2[5/2]_2 \rightarrow 6s\,^2[3/2]_1^\circ$ transition (see Fig. 4.1). Fig. 4.4 (c) shows the acquired line shape for third harmonic generation by three photons of the SH field, enhanced by the two photon resonance. On the the x-axis we plot the fundamental wavelength λ_F for better comparison with Fig. 4.4 (a). In this case the line shape stays symmetric, exhibiting only little resonance shift, that can be well described by a linear dependence. We determine a similar shift of of 0.61(8) $\frac{\text{THz}}{\text{TW cm}^{-2}}$ for the resonance position for both acquired signals. The derived shift corresponds to about half the ponderomotive shift of the ionization continuum. We conclude that for the low intensities used in the quantum interference

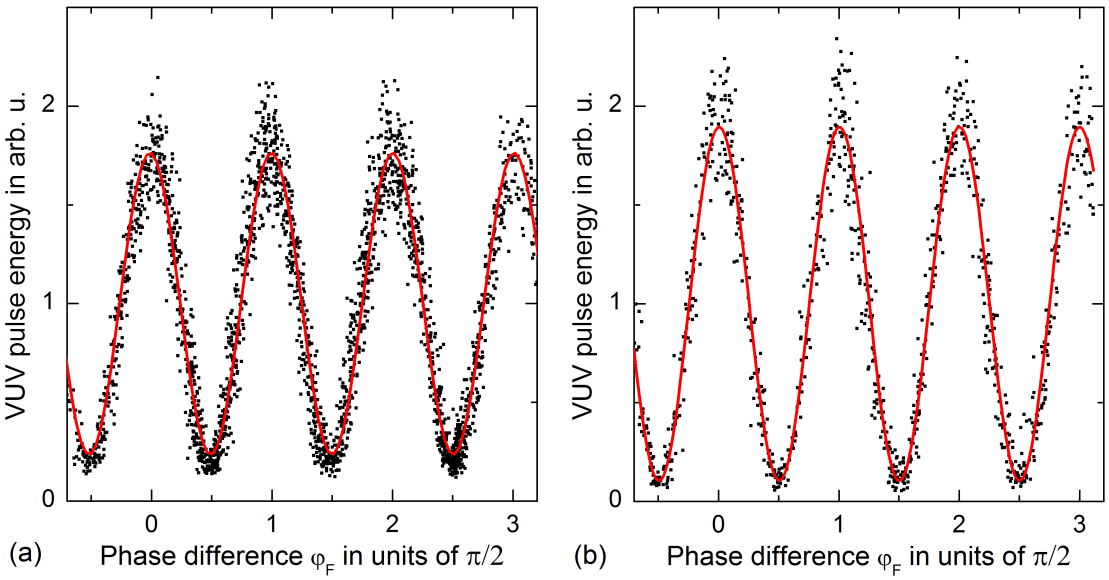

Figure 4.5: VUV intensity vs. phase difference of the driving laser fields at fundamental laser wavelengths of (a) $\lambda_F = 512.0\,\text{nm}$ (resonant) and (b) $512.7\,\text{nm}$. Black dots depict single shot experimental data without any averaging. Laser intensities are $I_F = 1.1(3)\,\text{TW/cm}^2$ and $I_{SH} = 5(1)\,\text{GW/cm}^2$. The red lines show fits with simple sine functions with a visibility of 76(3) % and 90(3) % respectively. [60]

experiment ($I_{SH} \ll 1\,\text{TW/cm}^2$), the resonance shift introduced by the SH field is also negligible.

4.5 Results

After the experimental determination of the resonance frequency, we tune the fundamental wavelength to the (unperturbed) 4-photon resonance at $\lambda_1 = 512\,\text{nm}$ and monitor the fifth harmonic yield versus the relative phase between fundamental and second harmonic laser pulses. The fifth harmonic pulse energy (as expected) shows an almost quintic power dependence with respect to the fundamental pulse energy, resulting in a huge spread of the (single shot) data points for the given statistical distribution of amplified pulse energy (see 2.1.3). To reveal the interference pattern from the spread in VUV pulse energies generated, we only analyze the VUV pulse energy generated from pulses within a window of ±7% around a peak intensity of[18] of I_1 =1.1 TW/cm². The resulting signal is shown in Fig. 4.5 (a). For this data set the second harmonic intensity is attenuated to I_2 =5(1) GW/cm² yielding maximal visibility of the sinusoidal interference trace. We determine the visibility by a fit to the experimental data yielding an

[18]The values stated here differ from the published values in [60], due to lower than expected transmission of the optics between the energy measurement position and the gas jet. We derive the correction factors of (85(8)% for UV and 76(16)% for visible pulses) from a pulse energy measurement inside the vacuum spectrometer (i.e. after the focus) and data for the cw transmission of the visible interferometer arm at 512 nm wavelength acquired after the publication of the data.

already high value of 76(3) %.

The degree of coherent control can even be enhanced by detuning the laser about one bandwidth (0.7 nm) towards lower wavelength. At the same intensities we now achieve a visibility $v = 90\%$, shown in Fig. 4.5 (b).

Both data sets shown in 4.5 demonstrate an efficient way to control a frequency conversion process by proper choice of the relative phases of the driving fields. It is possible to enhance a desired harmonic generation or even suppress an unwanted harmonic or transition. The demonstrated degree of control reaches a factor of 18 between the VUV yields of constructive and destructive phases. To the best of our knowledge, there are only few quantum interference experiments (for arbitrary systems or quantum processes) with similar modulation depths. In particular, there were no quantum interference experiments in frequency conversion of short laser pulses with up to 90(3) % modulation. As another realization of ultrafast coherent control with a very high visibility, we note the very recent experiments in coherent control of photo-electrons, emitted from a nano-tip. At these strongly localized targets, suppressing spatial averaging effects [57,58] a visibility of 94 % and 97.4 % in a four- vs. three-photon photo-emission is demonstrated.

4.5.1 Effect of resonance detuning

In the previous paragraph we discussed a higher visibility for detuned excitation. This unexpected feature is not easily explained. At the first glance it seems that the Stark shift pushes the $6p^2[5/2]_2$ resonance down towards $\lambda_F = 512.7$ nm fundamental wavelength, when the intensity is increased. However together with the spectroscopy data shown in 4.4 we discover that the highest efficiency in frequency conversion at $I_F = 1.1\,\mathrm{TW/cm^2}$ occurs at $\lambda_F = 511.8$ nm. In the measurements shown in Fig. 4.5 also the higher absolute VUV yield is generated at 512 nm fundamental wavelength, indicating a resonance position nearby.

Figure 4.6 shows the relative VUV yield (averaged over all phases φ) and the visibility of the quantum interference for fundamental wavelengths next to the 4-photon resonance. We note that a 10 % pulse duration fluctuation[19] between the data sets may lead to fluctuations in the recorded VUV yield. Still the spectral envelope of the yield is in qualitative agreement to the spectroscopic investigations, featuring it's maximum near 512 nm. Surprisingly, the quantum interference (QI) visibility is consistently higher below resonance, rising from about 70 % to almost 90 %. This higher value seems to be constant until 515 nm fundamental wavelength and within the uncertainty of the fits and is clearly higher than for blue detuned excitation. There are two possible explanations for this effect:

(1) The detuning from the $6p^2[5/2]_2$ level itself effects the relative phases of the two conversion pathways in a way not captured by the simple model.

(2) For fundamental wavelength below 511 nm (or 510 nm at the peak intensity of 1.1 TW/cm²) the fifth harmonic addresses the ionization continuum (i.e. the fifth photon couples the continuum states with the $6p^2[5/2]_2$ intermediate state).

[19] The pulse length could not be measured as the FROG spectrometer was used to stabilize the OPO with the spectrum of the amplified pulses as a feedback parameter.

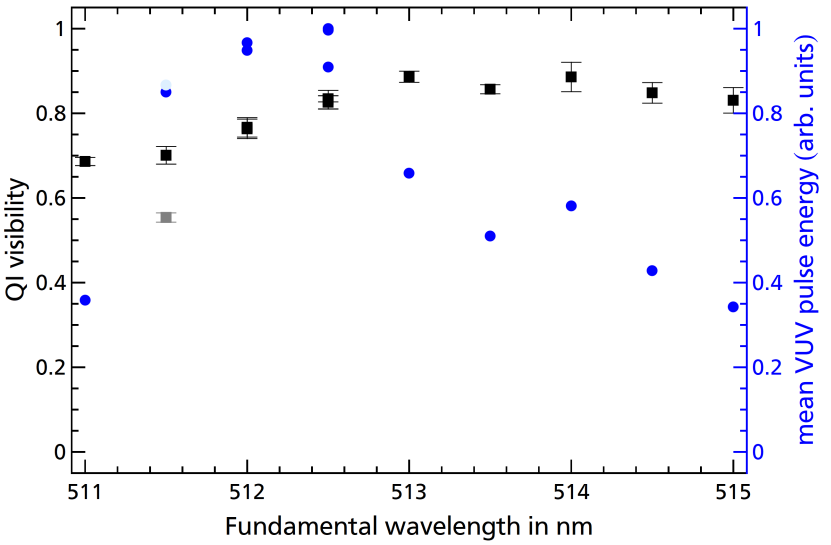

Figure 4.6: Mean VUV yield and visibility of the QI signature at different fundamental wavelengths. Error bars depict the standard uncertainty of the fits. The lighter set of data points was measured with residual phase mismatch inside the BBO crystal.

This coupling leads to resonantly enhanced photo-ionization and exhibits an additional loss channel competing against the frequency mixing process. This possibly introduces decoherence to the quantum system, reducing the visibility. Because of the finite bandwidth (0.66 nm FWHM) of the pulses this coupling fades in gradually.

Except of the 15% reduction in visibility, the detuning from resonance has no strong effect on the QI visibility as long as the interferometer is compensated for dispersion. In the present experiment the absolute fringe position shifted linearly by 0.04 π (20 nm delay) per nanometer detuning.[20]

We will now have a closer look on two parameters that strongly affect the visibility and therefore have been optimized for each of the above results.

4.5.2 Variation of interference traces with laser intensities

To achieve large visibility the conversion efficiencies between fifth harmonic generation driven by the fundamental beam exclusively and four-wave mixing driven by the fundamental and the second harmonic beam have to be matched. In our setup we tune the (peak) intensity of the second harmonic at a constant (peak-) intensity (0.7 TW/cm^2) of the fundamental pulses. This is equivalent to matching the light intensities of a conventional interferometer, but in contrast to the optimal fraction of 1:1 in our nonlinear phase control setup we have to balance a two-photon excitation with a four photon excitation of much lower effective transition moment. As a result we strongly attenuate the second harmonic beam. We record the visibility for several SHG intensities and show the data in Fig. 4.7.

The data shows, that already with this parameters, a high degree of coherent control is possible, with highest visibility of about 75 % at intensities of around 1.3 GW/cm^2 for the second harmonic. The maximum visibility corresponds well with the value achieved in Fig. 4.5. We notice that a variation of 50 % in SHG

[20] Without compensation we calculate a phase dispersion of 10 π per nanometer detuning, leading to strong temporal averaging.

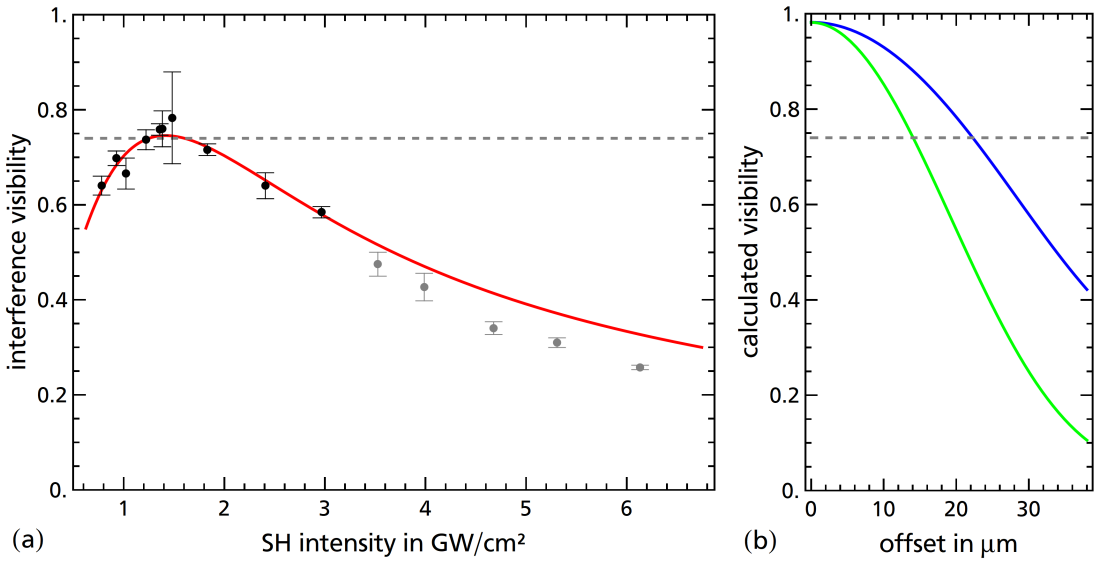

Figure 4.7: (a) Visibility of quantum interference in VUV pulse energy at a fundamental wavelength of 512 nm, plotted versus the SH intensity. Black and gray squares show the mean visibility at a fundamental intensity of 0.7(2) TW/cm². The red line is a numerical calculation of the dependence. In the model we assume an offset of the two beams in the focal region. The drop in visibility with respect to horizontal (blue) and vertical (green) offset is shown in Fig. (b) (discussion see text). Dashed lines indicate 74% visibility.

intensity only reduces the visibility about 10% before further variation leads to a significant drop. The absolute values of the SH intensity are much lower because of the I_{SHG}^2 vs. I_F^4 dependence of the excitation probability. In our scheme, the SH power automatically reduces accordingly when attenuation the fundamental before the BBO crystal.

We now analyze the functional dependence by comparing the results with a numeric integration of equation 4.6 in spatial and temporal domain[21].

For our experimental conditions we first calculate the decrease in visibility due to the imperfect spatial matching of the foci. We compute a drop of less than 3 % due to the transversal mismatch of the foci. The longitudinal phase change due to the difference in Gouy phase of the two beams is well below 1%. This is because of the large ($z_R \geq 11\,\mathrm{mm} \gg L = 1.5\,\mathrm{mm}$) and almost equal Rayleigh lengths of the fundamental and SH beam[22]. We also account for the residual phase dispersion of 0.08 $\frac{\pi}{\mathrm{nm}}$ by adding the nonlinear polarization of 23 wavelength steps, weighted with the spectral power distribution of the pulse. This dispersion further reduces the visibility to slightly above 96 %.

The obtained value is still significantly higher than our experimental results. Therefore, to explain the limited visibility, we allow for a misalignment Δx, Δy in transversal direction. The red line in Fig. 4.7 (a) shows the calculated QI vis-

[21] As we are only interested in the relative quantity visibility, we neglect phase matching by setting the wave vectors of both Gaussian beams to zero, to reduce the necessary spatial resolution to 0.5 points/μm. Furthermore we calculate with relative susceptibilities and intensities only.

[22] Consequently, we omit the integration in longitudinal z-direction for the following investigations.

ibility at a transversal offset of $\Delta y = 14\,\mu$m yielding a maximal value of 74 %. The same dependence is obtained when allowing for $\Delta x = 22\,\mu$m of horizontal offset (compare Fig. 4.7 (b)). The allowable offset for a given drop in visibility in horizontal direction is higher due to the better matching of their spatial intensity distributions in this direction. The calculation involves the ratio of unknown susceptibilities $\chi^{(3)}_{FWM}$, $\chi^{(5)}_{5HG}$, which remains as a free parameter. We fit the simulation to the experimental data between 1 and 3 GW/cm² (shown in black), obtaining a function that resembles the data points very well. Above 4 GW/cm² the experimental data (shown in gray) exhibit a drop of approximately twice their standard uncertainty in visibility when compared to the numerical expectation. We can not reproduce this effect by any parameter variation, so we attribute it to a variation in experimental conditions.

Another possibility is again the photo-ionization channel: A third photon of the second harmonic field couples the intermediate state to the ionization continuum. This process is proportional to the SH intensity and can cause a loss in coherence. We note that this data is acquired at 512 nm, where the visibility has already dropped about 13(2) % when compared to the optimal parameters for red detuned excitation, reaching up to 90 % visibility (see Fig. 4.6). For this visibility we compute an offset of 8 μm or 12 μm in vertical or horizontal direction (compare Fig. 4.7 (b)). The experimental uncertainty in relative focus position is estimated to be below 15 μm transversal direction. So both values of visibility can be explained by the experimental limitations in spatial overlap. However we suspect the offset to cause only the drop to ~90 % in visibility and another effect in the spectral domain to cause the further drop to 75% at and blue detuned to the 4-photon resonance.

4.5.3 Variation of interference traces with the laser wavelength

In subsection 4.5.1 we investigated the effect of resonance detuning on the visibility of the interference signature. However when we specify a phase, we can only tune this phase $\varphi_F = 2\pi\Delta z \cdot n_{air}(\lambda_F) \cdot \lambda_F^{-1}$ by changing the path of the pulse by Δz, resulting in a delay of $\Delta t = c^{-1} \cdot n(\lambda_F) \cdot \Delta z$ with the refractive index $n_{air}(\lambda_F)$ of air. Therefore the fundamental wavelength also changes the functional dependence of optical delay and phase. From 4.4 we expect four oscillations of the interference signal for a difference of one wavelength in path length. Our experimental setup is capable of resolving the change in modulation period with fundamental frequency as it allows for long delay scans maintaining the 5 nm phase measurement resolution without changing the spatial overlap. We choose a measurement range of 35 μm as it contains 250 oscillation cycles at 514 nm fundamental wavelength and 261 oscillation cycles at 512 nm fundamental wavelength to clearly reveal the wavelength dependent delay.

In Fig. 4.8 we visualize the changing modulation period by showing cutouts of three data sets of the VUV pulse energy acquired over a delay of 111 fs (35μm) at 512, 513 and 514 nm fundamental wavelength. During the long measurement time of 30 minutes for one set of data we check the determination of the relative phase several times by repeated control measurements of already measured parts

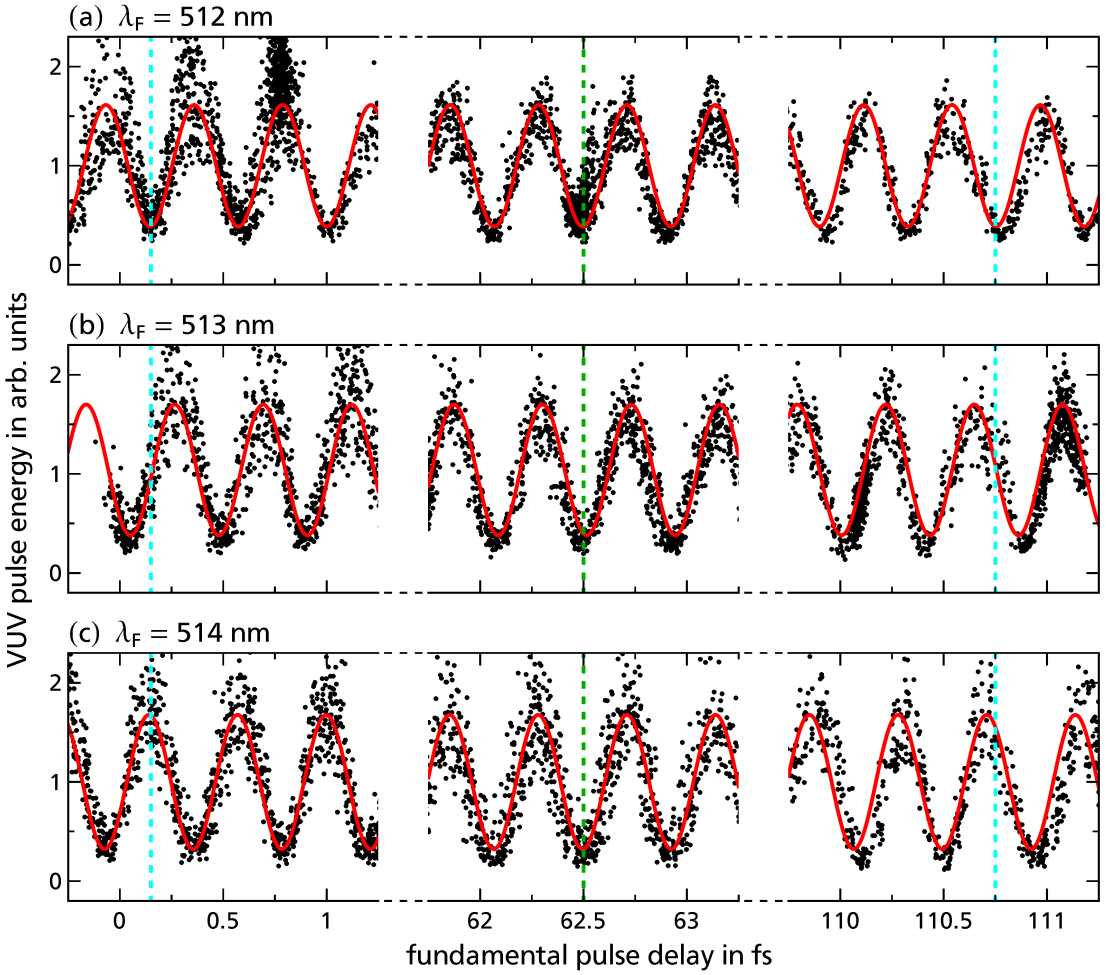

Figure 4.8: Long range measurements of the VUV pulse energy vs. phase difference of the driving laser fields at fundamental laser wavelengths of (a) 512 nm (b) 513 nm and (c) 514 nm. For better visibility, the plots show short sections of the recorded long interference traces only. Black dots depict single shot experimental data without any averaging. Laser intensities are $I_F = 1.1\,\mathrm{TW/cm^2}$ and $I_{SHG} = 1.8\,\mathrm{GW/cm^2}$. Red lines show fits with simple sine functions. Dashed lines are to guide the eye (see text). [60]

λ_1 in nm	retrieved period in nm	expected period in nm
512.00(15)	128.03(6)	128.00(4)
513.00(15)	128.27(7)	128.25(4)
514.00(15)	128.48(6)	128.50(4)

Table 4.1: Modulation period of the quantum interference signal for three driving wavelengths λ_1 (in vacuum). [51]

of the interferogram and take special care to hold all experimental parameters constant. In the data analysis we notice a slight decrease in absolute VUV signal at constant driving intensity. This might be caused by a change in the gas density or in a subtle degradation of the EMT dynodes. However for each wavelength despite the slight change in absolute signal a clearly visible interference signal of (locally) constant visibility was acquired.

We align[23] the measurements such that they are in phase at the middle of the scan range (referenced by a green dashed line). Near delays of 0 and 110.75 fs (cyan dashed line) the data set acquired at 513 nm already shows phase difference of a quarter cycle. The interference signal detuned 2 nm from the central frequency is even out of phase at these positions. This already visually shows the dependence of the phase as a function of central wavelength. To further solidify the finding, we perform a nonlinear regression of a sinusoidal model to the whole data set (i.e. much more oscillations as shown in Fig. 4.8. The results are shown in Table 4.1. In parenthesis we state the standard uncertainty which is due to the uncertainty $\Delta\lambda = 0.005$ nm in the wavelength of the reference laser combined with the statistical error of about 0.05 nm when retrieving the oscillation period from the quantum interference traces by fitting. The expected oscillation period also has an uncertainty of 0.04 nm due to the accuracy in the determination of the fundamental laser central wavelength. The derived oscillation periods agree very well with the expected values and clearly prove the correspondence of interference period and fundamental wavelength.

4.5.4 Variation of the interference visibility with pulse delay

In contrast to the above traces, in which the interference visibility is constant (within the experimental accuracy), an additional delay of the fundamental pulses leads to a drop in interference visibility. For bandwidth limited pulses, we can derive the visibility envelope from 4.4 and 4.9 as a function of delay

$$v_\tau \propto \frac{\int_{-\infty}^{\infty} 2|\tilde{P}^{(5)}_{5HG} \cdot \tilde{P}^{(3)}_{FWM}|\,dt}{\int_{-\infty}^{\infty} |\tilde{P}^{(3)}_{FWM}|^2 + |\tilde{P}^{(5)}_{5HG}|^2\,dt} \tag{4.10}$$

Here we neglect the effect of the spatial coordinates, possibly reducing the overall visibility as discussed above. We now assume perfect frequency doubling (i.e. $E_{SH}(t) \propto E_F^2(t)$) and drop the nonlinear susceptibilities to reveal the convolution kernel in the denominator:

$$v_\tau \propto \frac{\int_{-\infty}^{\infty} 2 \cdot E_F^5(t) \cdot E_F(t) E_F^4(t-\tau)\,dt}{\int_{-\infty}^{\infty} |E_F(t) E_F^4(t-\tau)|^2 + |E_F^5(t)|^2\,dt} \tag{4.11}$$

We shift the delay τ of the fundamental into the second harmonic field $E_{SH}(t-\tau) \propto E_F^4(t-\tau)$ to reduce the number of occurrences. The temporal FWHM of

[23] For each measurement we optimize the BBO crystal for optimal SHG efficiency, to avoid spectral shaping of the SH spectrum due to the limited phase matching bandwidth. The birefringence of the BBO crystal also affects the HeNe reference laser, so we have to recalibrate the phase measurment for each dataset, possibly introducing a phase offset between the measurmenets.

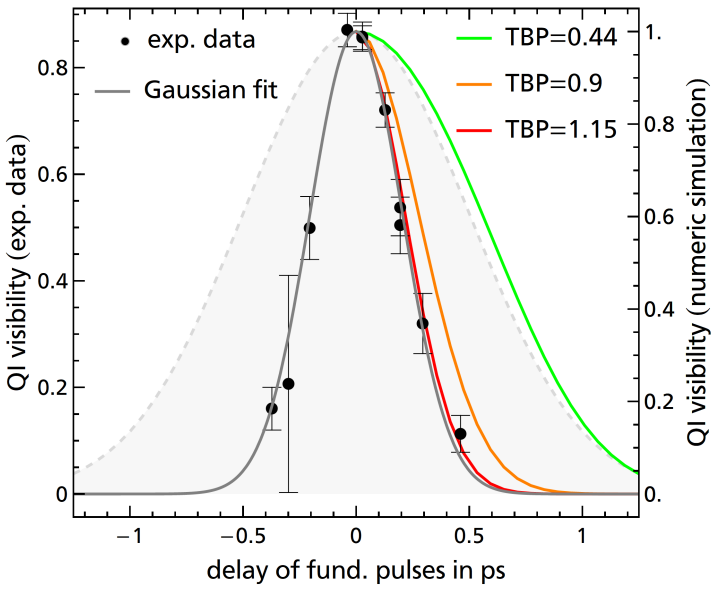

Figure 4.9: Visibility of the interference pattern (black dots, together with standard uncertainty of the fit) vs. delay of the fundamental pulses ($\lambda_F = 513\,\text{nm}$) with respect to second harmonic. Superimposed is a Gaussian fit (gray line). Colored lines are the results of numerical simulations for Gaussian pulses of different time-bandwidth products. The gray shading in the background is the assumed temporal intensity distribution of the laser pulse.

the convolution $E_F^5 E_F \otimes E_F^4$ in the denominator can be calculated from the standard deviations of the Gaussian distributions $\sigma(E_F^5 \cdot E_F) = {}^{\sigma(E_F)}/_{\sqrt{6}}$ and $\sigma(E_F^4(t-\tau)) = {}^{\sigma(E_F)}/_{\sqrt{4}}$, yielding [71]

$$\sigma_c = \sqrt{(\frac{\sigma(E_F)}{\sqrt{6}})^2 + (\frac{\sigma(E_F)}{\sqrt{4}})^2} = \sqrt{\frac{5}{12}}\,\sigma(E_F) \tag{4.12}$$

This convolution width is slightly shallower than the fundamental pulse width. As we can only observe the visibility, the convolution is modified by the τ-dependent normalization, resulting in an visibility envelope with a FWHM of $1.055 \cdot \tau_p$ with the FWHM pulse duration $\tau_p = 1.15(13)\,\text{ps}$. Thus, for bandwidth limited pulses we expect interference visibility for the full pulse duration.

We record a set of interference traces for different delays[24] of the fundamental pulses and show the visibility and the standard uncertainty of the sinusoidal fit in Fig. 4.9. It is evident from the experimental data that the visibility drops to below 10 % already within the FWHM of the fundamental pulse. By a Gaussian fit (gray line in Fig. 4.9), we determine the temporal visibility width to be $\tau_v = 0.48\,\text{ps}$ (FWHM), corresponding to $0.42 \cdot \tau_p$. The visibility width however corresponds much better with the hypothetical Fourier limited pulse duration[25] of $\tau_p = 584\,\text{fs}$, than with the derived visibility envelope for a transform limited pulse (see green line in Fig. 4.9). The chirp of the applied fundamental and SH pulses significantly reduces the visibility width (as known from fringe resolved SHG autocorrelation).

We modify our numerical calculation of equation 4.6 to account for the chirp of both, fundamental and second harmonic pulses by introducing a complex electric field envelope $E_F(x, y, z, t)$ with quadratic temporal phase $\phi_t(t)$ such, that the pulse exhibits a duration of $\tau_p = 1.187\,\text{ps}$ (including the GDD of the dispersion

[24] The delay stage is selected for minimum pitch and yaw such that the focus position is constant to below 7 μm in each dimension for 12 ps of delay.

[25] calculated from the spectral width of the fundamental pulses $\Delta\lambda_F = 0.66\,\text{nm}$ (FWHM).

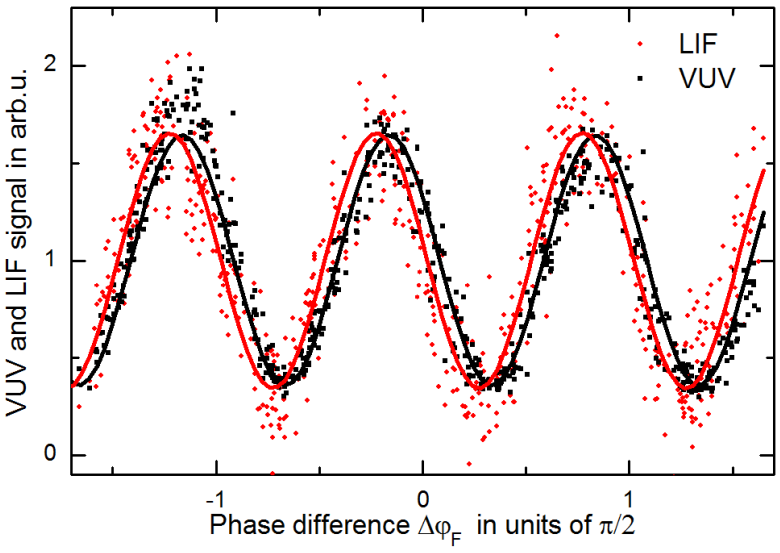

Figure 4.10: LIF (red circles) and VUV (black squares) intensities vs. phase difference of the driving laser fields. The laser intensities are $I_F = 2.8(6)\,\mathrm{TW/cm^2}$ and $I_{SHG} = 28(6)\,\mathrm{GW/cm^2}$. Lines show fits with sine functions to the LIF signal (red line) and VUV signal (black line).

block) and a spectral width corresponding to $\Delta\lambda_F = 0.66\,\mathrm{nm}$ (TBP = 0.9), as determined by our pulse spectrometer. We assume that the temporal phase of the SH field is twice the temporal phase of the fundamental[26].

The resulting visibility envelope is shown in Fig. 4.9 as orange line. It has duration τ_v =0.65 ps, very close to the experimental results. A simulation with a TBP of 1.15 (red line) resembles the shape of the measurement data even better. The small discrepancy is within the uncertainty margin of pulse characterization. We conclude that the results are very well explained by the numeric model.

4.5.5 Simultaneous interference measurements of excited state population and frequency conversion

In our coupling scheme, excitation of atomic population to state $6p\,^2[^5/_2]_2$ is possible either via four-photon excitation driven by the fundamental radiation or two-photon excitation, driven by the SH field. The LIF signal, as shown in Fig. 4.10 in red, is acquired simultaneously with the VUV pulse energy (shown in black). To acquire the LIF signal with sufficient signal to noise ratio, we increase the fundamental intensity to $I_F = 2.8(6)\,\mathrm{TW/cm^2}$ and the SHG intensity is automatically increased to $I_{SH} = 28(6)\,\mathrm{GW/cm^2}$. As expected, we only observe significant fluorescence when the laser is detuned less than one spectral bandwidth from the four-photon resonance. Therefore we tune the laser to $\lambda_{fund} = 512.0\,\mathrm{nm}$ for maximum signal. The VUV interference trace exhibits a visibility of 65(2) %. This value does not agree with the visibility of 76% recorded at 1.1 TW/cm² in Fig. 4.5 (a). We note that at the higher fundamental intensity used for the present data set back-conversion and/or higher order nonlinear effects are occurring inside the BBO crystal during frequency up-conversion. This is visible in a proportionality $W_{SH} \propto W_F^p$ with $p < 1.6$ (i.e. saturated frequency conversion). This saturation distorts the temporal shape and phase of the SH pulse such, that temporal (and spectral) averaging

[26]This is justified for ideal frequency doubling and a perfectly compensated interferometer.

reduces the modulation of the total VUV yield.

The fluorescence signal also exhibits pronounced sinusoidal modulation with the same visibility and period as the frequency mixing signal. The fitted sine function finally reveals a slight but consistent lag of 7.8(2) nm delay between the two data sets. We repeated the measurement three times, twice with compressed, nearly bandwidth limited pulses and an improved bandpass filter combination[27] in front of an avalanche photo-diode[28] for detection, yielding a spectral selectivity of $> 10^3$ when compared with light at wavelength shorter than 1000 nm and $\gg 5 \cdot 10^7$ versus scattered laser light. Although the visibility is very sensitive to experimental conditions, the phase relation of the two signals seems stable, every time showing the same phase lag of $0.0304(8)\,\pi$ at 512 nm fundamental wavelength. As both signals are acquired simultaneously, we attribute the phase lag not to the phase of the fundamental, but suggest a phase lag of $0.122(3)\pi$ with regard to the 128 nm oscillation period, which could be introduced by the difference $\Delta_\chi - \Delta_\mu$ in atomic phase contributions (see equations (4.7) and (4.5)).

4.6 Conclusion

In this chapter we demonstrated the implementation of coherent control in frequency conversion of ultra-short laser pulses towards the VUV spectral regime. In a systematic study we examined the effect of temporal and spatial overlap, relative intensities and central wavelength on the visibility of the interference signature. Optimizing all these parameters, we were able to achieve up to 90 % of interference visibility, corresponding to a factor of 18 increased in VUV yield, when constructive and destructive interference is compared. This value one of the highest degrees of control on a frequency conversion process by phase control.

By precise phase measurement we showed the change in temporal modulation period with driving wavelength and could distinguish the phase lag between the frequency conversion yield and the excited state population of the intermediate state. We attribute this phase lag to the different phase of the multi-photon transition moments for four-photon excitation and fifth harmonic generation. This is because more atomic levels (Rydberg levels and ionization continuum) contribute to the nonlinear polarization for fifth harmonic generation and possibly introduce additional phase.

[27] Thorlabs LP950 + Thorlabs BP990-10. At wavelengths longer than 2500 nm, where the two filters open again, the spectral response of the silicium photo-diode itself attenuates the signal several orders of magnitude.

[28] Laser Components SAR500S3 biased at 200V.

Chapter 5

Phase matched harmonic generation near a multi-photon resonance

5.1 Introduction

The previous chapters dealt with harmonic generation in the limit of a thin medium. In this chapter the interaction length L is increased by confining the medium as well as the driving radiation inside a hollow core optical waveguide. As a result, the fundamental radiation interacts with more atoms, increasing the harmonic yield as long as the phase mismatch between harmonic and fundamental vanishes. The phase-matching condition can be achieved by balancing the dispersion generated by the geometric confinement of the light inside the waveguide with the pressure tunable dispersion of the gaseous medium for a proper choice of the waveguide diameter and the input coupling of the fundamental radiation [72, 73].

The combination of resonantly enhanced harmonic generation together with phase matching is a promising approach towards even higher conversion efficiencies. However to our knowledge there are no experimental publications on phase-matched, resonantly enhanced harmonic generation in waveguides. We investigate the feasibility of phase matched fifth harmonic generation in argon close to the five-photon resonance already investigated in chapter 3. We demonstrate that appropriate choice of the gas pressure maintains optimal phase-matching conditions also in the presence of strong AC Stark Shifts at high intensities. Moreover, we reveal the considerable contribution of higher-order transversal waveguide modes to the total conversion efficiency and investigate the role of cascaded frequency conversion processes (which were already shown to support efficient frequency conversion in waveguides [74]). The experimental work is supported by a numeric model, taking multi-mode propagation, and cascaded frequency conversion processes into account. Finally, we transfer the method of buffer gas admixture (commonly known to tailor phase matching conditions for harmonic generation in gas jets and gas cells [75]) towards harmonic generation in waveguides to achieve higher conversion yield at a fixed laser frequency. The research results were published in the Journal of the Optical Society B [76].

5.2 Phase matched harmonic generation in a waveguide

5.2.1 Propagation of light in hollow core waveguides

When an electromagnetic wave is guided inside a waveguide of radius a, the spatial confinement leads to the development of transversal modes governed by the Helmholtz-equation. For a circular symmetric waveguide, an electromagnetic field propagating along the z direction has to obey the Bessel differential equation in the radial r direction. Among the solutions for this equation, the hybrid EH_{1m} modes [72] do resemble a linearly polarized input field best. In a circular, dielectric step index waveguide of radius a with a refractive index $n < 2.02$, those modes also have the lowest losses [77].

When coupling a linearly polarized input field polarized along the transversal, unitary vector $\overrightarrow{e_T}$ to the waveguide, the field guided in the m^{th} mode,

$$\vec{E}_{j,m}(r,z,t) = \tilde{E}_{j,m}(r,z,t) \cdot \overrightarrow{e_T} = \bar{E}_{j,m}(r,z) \cdot e^{-i(\omega_j t)} \cdot \overrightarrow{e_T} + c.c. \tag{5.1}$$

is also linearly polarized[1] along $\overrightarrow{e_T}$ in the transversal direction of the input polarization. In contrast to the general case of chapter 1, the spatial dependence of the electric field $\bar{E}_{j,m}(r,z)$ is given in the radial direction by the Bessel function of first kind in lowest order, J_0(shown in Fig. 5.1 (a)). In propagation direction, the electric field is determined by the propagation constant $\gamma_{(j,m)}$ (of mode m at harmonic frequency $j\omega_1$). The complex amplitude of each mode is given by $E_{j,m}$:

$$\bar{E}_{j,m}(r,z) = E_{j,m} \cdot J_0\left(u_{1m}\frac{r}{a}\right) \cdot \exp\left(i\int_0^z \gamma_{j,m}(z')\,dz'\right) \tag{5.2}$$

The complex phases of these linearly polarized, radially symmetric modes evolve with the propagation constant

$$\gamma_{j,m} = k_j - \left[\frac{1}{2k_j}\left(\frac{u_{1,m}}{a}\right)^2 \cdot \left(1 - i\frac{2\upsilon_{EH}}{k_j a}\right)\right]. \tag{5.3}$$

Where u_{1m} is the m^{th} root of the Bessel function of first order. For waveguides with a radius larger than the wavelength of the light wave, the propagation is dominated by the complex plane wave propagation constant $k_j = \omega_j \cdot n(\omega_j, p) \cdot c^{-1}$, with the pressure dependent complex refractive index of the gas $n(\omega_j, p)$. The confinement of the beam by the waveguide adds an additional, geometric component to the phase velocity, determined by the waveguide radius a (term in brackets in equation 5.3). The term $\upsilon_{EH} = (\upsilon_j^2 + 1)/(2\sqrt{\upsilon_j^2 - 1})$ accounts for the lossy guidance by reflection at grazing incidence at the waveguide walls. It is a function of the refractive index of the waveguide (n_W) normalized to the refractive

[1] These modes by derivation of Marcatili et. al neglect the component of the field in the propagation direction as well as other corrections of the same order (λ/a). In our case $\lambda/a \approx 1/100$, this approximation is well justified for the waveguides discussed here.

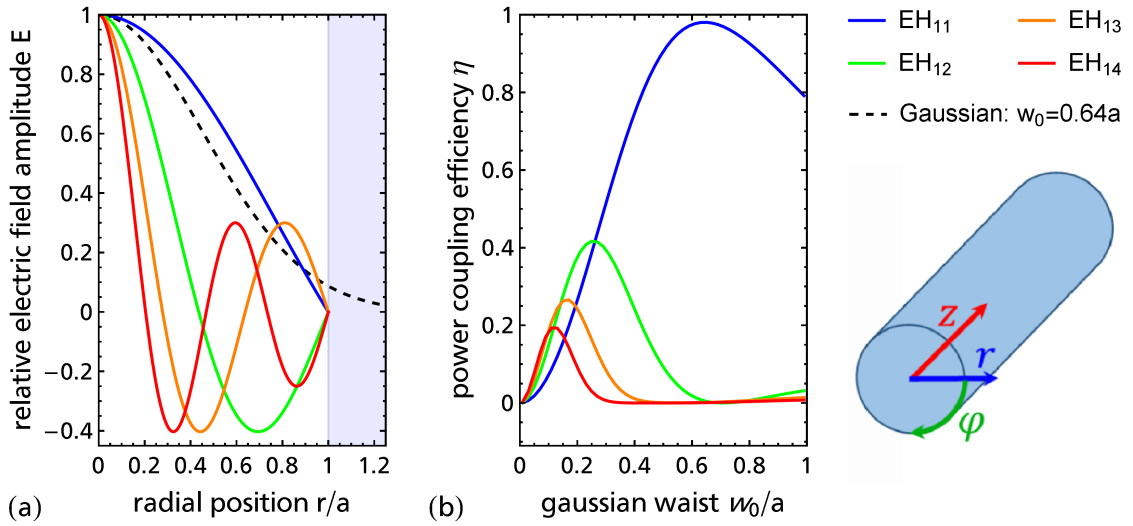

Figure 5.1: (a) Strength of the transversal electric field of the lowest three EH_{1i} modes in a circular dielectric hollow core waveguide with respect to the normalized radial coordinate r/a. The dashed line shows the Gaussian input field of highest coupling efficiency, the blue shaded area represents the waveguide wall. (b) Power coupling efficiency $\eta_m = \int_0^a |E_{1,m}|^2 r\,dr / \int_0^\infty |F_S|^2 r\,dr$ calculated from equation 5.6 for the lowest four waveguide modes for a Gaussian input beam with a waist w_0 at the waveguide entrance. The sketch to the right illustrates the geometry.

index of its gaseous (G) content $\upsilon_j = n_W(\omega_j)/n_G(\omega_j)$. In a given waveguide, the propagation constant $\gamma_{j,m}$ can be modified by tuning the gas density and thereby tuning the free space propagation constant k_j.

The attenuation constant $\gamma''_{j,m}$ of a gas-filled hollow core waveguide reads:

$$\gamma''_{j,m} = 2\,\mathrm{Im}\left[\gamma_{j,m}\right] = \underbrace{\left(\frac{u_{1,m}}{a}\right)^2 \cdot \frac{2}{k_j^2 a} \cdot \mathrm{Re}[\upsilon_{j,m}]}_{\text{waveguide}} + \underbrace{2\cdot\mathrm{Im}[k_j]}_{\text{gas}} \tag{5.4}$$

Here the attenuation by the bare waveguide is proportional to the real part of υ_{EH} and increases for higher mode numbers. The total attenuation of an electromagnetic wave at frequency ω_j also depends on the gas absorption. In our experiment however, attenuation is dominated by the waveguide, and the transmission is higher than 95 % for a capillary length of 55 mm at the fundamental frequency ω_1.

5.2.2 Input coupling

To generate harmonics inside a waveguide, the laser fundamental radiation must be launched into the waveguide. A known, linearly polarized, circularly symmetric[2] intensity distribution at the entrance of the waveguide ($z = 0$) excites modes

[2]For intensity distributions that are not circularly symmetric, also modes EH_{lm} of higher order l in the azimuthal dimension have to be considered.

of type $EH_{1,m}$ to satisfy the equation [78]

$$I_{in}(r, z=0) = \frac{\pi}{2Z}\left|\sum_m E_{1,m}(r,0) + c.c.\right|^2 . \tag{5.5}$$

Here Z is the impedance of the medium. At the interface, the energy flow in z-direction governs the coupling integral [79] for the electric field:

$$E_{1,m,} = \frac{\int_0^a J_0(u_{1m} r \cdot a^{-1}) \cdot F_s \cdot r\, dr}{\int_0^a J_0^2(u_{1m} r \cdot a^{-1}) \cdot r\, dr}, \tag{5.6}$$

Here the complex amplitudes E_{1m} of the waveguide modes are determined by the radial shape F_s of the source term. Assuming a Gaussian input beam with a focal plane at the entrance of the waveguide, the source electric field at the input $F_S = [\frac{Z}{\pi} \cdot I_{in}(r, \phi, z=0)]^{\frac{1}{2}}$ can be calculated from a measured intensity distribution I_{in}. Fig. 5.1 (b) shows the relative power coupled to the lowest 4 waveguide modes as a function of the Gaussian waist. A waist of $w_0 = 0.644a$ is best suited to couple the lowest waveguide mode $EH_{11}$with an efficiency of $P_{EH_{11}}/P_{in} > 98\%$.

5.2.3 Harmonic generation inside the waveguide

From the nonlinear wave equation (in SVEA, eq. 1.9) we derive the z-derivative

$$\frac{\partial E_{j,m'}}{\partial z} = \frac{i}{2\gamma_{j,m'}}\left[(k_j^2 - \gamma_{j,m'}^2)E_{j,m'} + \frac{\omega_j^2}{c^2\epsilon_0^2}\bar{P}_{j,m'}^{NL}(z) \cdot e^{-i\int_0^z \gamma_{j,m'}(z')\,dz'}\right] \tag{5.7}$$

of the mode amplitudes. Here the complex nonlinear polarization amplitude of the respective frequency and mode (calculated in section A.3.1) is the source term for harmonic generation. When the fundamental radiation is assumed to be perfectly coupled into a given waveguide mode m, inside a waveguide of constant radius, filled with a gas of homogeneous pressure, this equation can be transformed to

$$\frac{\partial E_{j,m'}}{\partial z} = \frac{i}{2\gamma_{j,m'}}\left[\frac{\omega_j^2}{c^2\epsilon_0^2}|\bar{P}_{j,m'}^{NL}| \cdot e^{-i\Delta\gamma_{m,m'}^{(j)} \cdot z}\right]. \tag{5.8}$$

We have neglected the first term of the brackets[3] and collected the phase difference between nonlinear polarization $\bar{P}_{j,m'}^{NL}(z)$ and the generated harmonic $E_{j,m'}$ in the mismatch of propagation constants of modes m and m' [73]

$$\Delta\gamma_{m,m'}^{(j)} = j \cdot \gamma_{1,m} - \gamma_{j,m'}. \tag{5.9}$$

[3] $k_\perp^2 = (k_j^2 - \gamma_{j,m}^2)$ is the squared transversal wave number of the given waveguide mode. We suspect this term to be the result of dropping the transversal derivative in the nonlinear wave equation in combination with a tightly confined mode that *can* have a significant derivative in transversal direction, when modes of high m or small waveguides are considered. In the present case of $a \approx 50\mu$m, $m < 5$ in comparative numeric calculations, we found the term to be negligible).

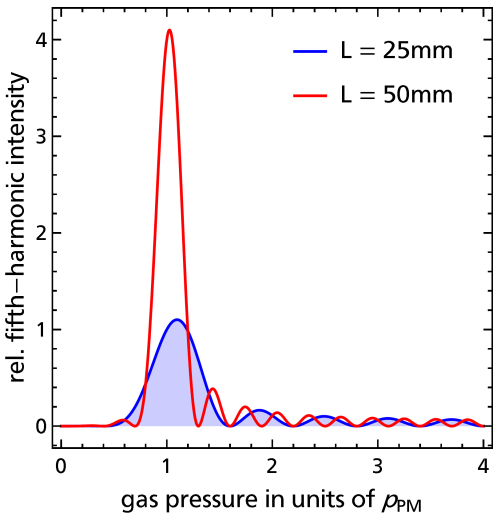

Figure 5.2: Fifth harmonic intensity $I_{5,1}$ guided inside the EH_{11} mode of a 25 mm (blue) and 50 mm (red) long waveguide of radius a =50 μm as function of the gas pressure p. The fundamental radiation is coupled to the EH_{11} mode exclusively. Curves are normalized to the intensity generated inside the 25 mm long waveguide at the phase matching pressure p_{PM}. The maximum of each curve is shifted slightly towards higher pressures because of the p^2-proportionality of I_5. For simplicity, only direct fifth-harmonic generation via $P^{(5)} \propto \chi^{(5)}_{(5\omega)} \cdot E^5_{1,1}$ is considered.

The mismatch $\Delta\gamma^{(j)}_{m,m'}$ between the fundamental and the j^{th} harmonic guided in mode m' can be nullified by tuning the pressure p of the gas inside the waveguide such that the gas dispersion cancels the waveguide dispersion for the chosen combination of modes. Which mode combinations can be phase matched depends on the dispersion of the gas. Harmonics above a single-photon resonance, where the refractive index is smaller than in the visible regime (negative dispersion) support the most mode combinations, as the positive dispersion of the waveguide at constant $m' = m$ can then be canceled by a negative gas dispersion[4].

In a first, simple approximation, equation 5.8 can be spatially integrated along the waveguide of length L in the undepleted pump assumption, yielding the intensity of the fifth harmonic $j = 5$:

$$I_{5,m'} \propto |P^{NL}_{j,m'}|^2 L^2 \mathrm{sinc}^2\left(\frac{L}{2}\Delta\gamma^{(5)}_{m,m'}\right) \propto p^2 L^2 \mathrm{sinc}^2\left(g \cdot L\left(\frac{p}{p^{(PM)}_{m,m'}} - 1\right)\right) \tag{5.10}$$

In the left equation, the nonlinear polarization, as well as the refractive index are proportional to the number density N for a gaseous medium. In the limit of an ideal gas, $pV = Nk_bT$, we derive the simplified proportionality on the right hand side with the waveguide dependent parameter g. shown in Fig. 5.2 for $m = 1$ and $m' = 1$ for two lengths of the same $a = 50\,\mu$m waveguide. Both curves exhibit a pronounced maximum near the phase matching pressure. The average enhancement by phase matching (with respect to an arbitrary high pressure $p \gg p_{PM}$) scales quadratic with the waveguide length.

In reality, the longer propagation distance and the higher amount of particles inside a confined geometry does not only enhance the efficiency for generation of

[4]Harmonic generation energetically below bound states usually demands the harmonic to be guided in a higher mode compared to the fundamental beam. For combinations of different modes, the overlap between the nonlinear polarization and the guiding mode field is reduced (see section A.3.1), reducing the overall efficiency of the process. Therefore, a low difference in mode number is preferable. For highest efficiency in frequency quintupling, a negative $\Delta^{(5)}$ is optimal as it enables phase matching already for the fundamental waveguide modes exhibiting the lowest damping.

a desired harmonic, but also enhances all nonlinear interactions. For the previous experiments presented in this work, phase matching as well as the change in electric field amplitudes of other generated harmonics could be neglected, as their effect on the harmonic field of interest was very small. On the contrary, in waveguides cascaded frequency mixing [74] and self focusing have been reported. Both effects are a result from a third order nonlinearity on either the fundamental or the fifth harmonic field. Consequently for calculation of fifth harmonic generation, all terms of fifth or lower order have to be considered and the harmonic electric field cannot be calculated from the simple spatial integral of equation 1.9.

Furthermore, in our particular geometry of a ported waveguide with pressure ramps towards vacuum at the ends, the phase integral does not vanish, as the refractive index of the gas is a function of the propagation coordinate z. For pulsed excitation also finite spectral width of the laser pulses has to be considered, rendering an analytic solution basically impossible. We describe our numerical approximation after deriving the necessary physical quantities in the next chapters.

5.2.4 Calculation of the refractive index of argon

For phase matched harmonic generation despite from the waveguide dispersion, also the refractive index of the medium is important. A negative five-photon detuning to an excited state exhibits possible phase matching already for the fundamental waveguide modes while simultaneously enabling resonance enhancement. Unfortunately the Sellmeier equation for refractive index of argon [80] is only modeled from experimental data points at photon energies below the first excited state of argon. The equation involves just two resonance terms, corresponding to the levels of lowest energy, $4s'^{\,2}[1/2]^{\circ}_{1}$ at a transition wavelength of 104.8 nm and $4s^{\,2}[3/2]^{\circ}_{1}$ at 106.6, as well as an empiric term for the ionization continuum (see Fig. 5.3, red dashed line). The accuracy of the model above the $4s'^{\,2}[1/2]^{\circ}_{1}$ level has not been proven experimentally and is expected to exhibit increasing error with increasing photon energy. As this is the spectral region in which the harmonics will be generated, a deviation from the actual refractive index will lead to discrepancy between experiment and theory. To avoid this discrepancy, we develop an approximation of the refractive index starting from equation 1.17 for the atomic polarizability.

Up to the 5d manifold at 81.62 nm wavelength, experimental data for the oscillator strengths[5] $f_{n1} = 2m \cdot \omega_{n1}|\mu_{n1}|^2/(\hbar e^2)$ is available from measurements of Chan et. al. [39, 40] and Wu et. al. [85]. So for the lowest m bound-bound transitions, we can evaluate the terms of the sum in equation 1.17:

$$\alpha_1^{(1)} = \frac{e^2}{2m_e}\sum_{n=2}^{m}\frac{f_{n1}}{\omega_{n1}}\left[\frac{1}{\omega_{n1}-\omega-i\gamma_{n1}}+\frac{1}{\omega_{n1}+\omega+i\gamma_{n1}}\right]+R \tag{5.11}$$

Here the decay rate $\gamma \approx \frac{\omega_{n1}^3|\mu_{n1}|^2}{3\pi\epsilon_0\hbar c^3} = \frac{A_{n1}}{2}$ is approximated by half the Einstein A coefficient, i.e. neglecting decay to other excited states [37]. We average the tabulated

[5] We use the component of the transition moment parallel to the electric field polarization axis $|\mu_{n1}|^2 = \frac{1}{3}|n\hat{\mu}1|^2$

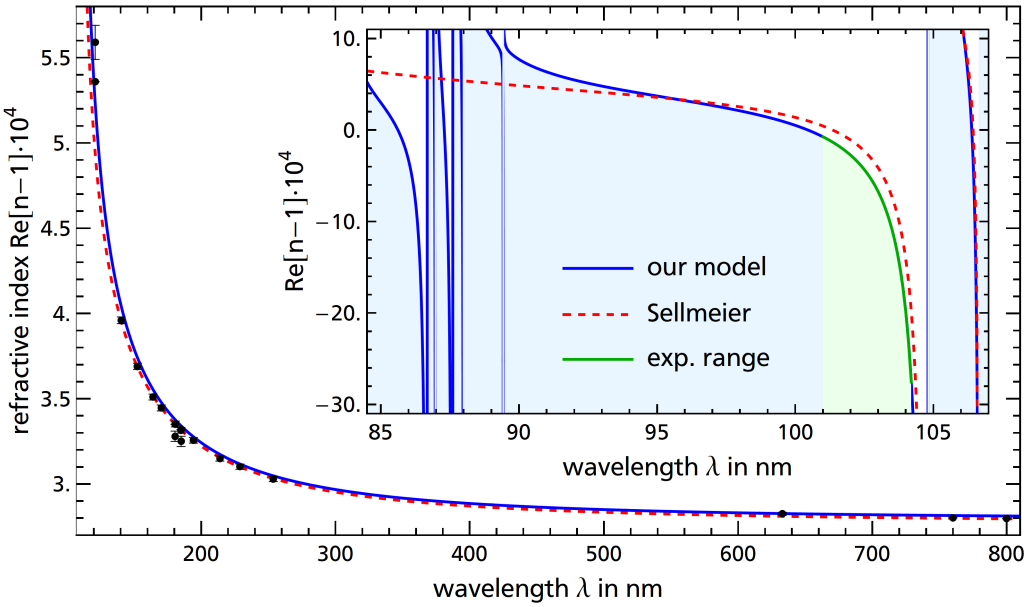

Figure 5.3: Refractive index of argon at normal conditions, computed by our model compared to experimental data [80–84] and the Sellmeier equation. The inset shows the values for the VUV spectral regime, with the tuning range of our experiment (green).

data of Chan and Wu and weight them the inverse of their specified error margins. The residual R covers the bound states of higher energy and the continuum levels.

$$R = \frac{e^2}{2m_e} \sum_{n=m+1}^{\infty} \frac{f_{n1}}{\omega_{n1}} \left[\frac{1}{\omega_{n1} - \omega - i\gamma_{n1}} + \frac{1}{\omega_{n1} + \omega + i\gamma_{n1}} \right]. \tag{5.12}$$

For this spectrum of photon energies only differential absorption cross sections are available [39, 85]. We calculate the imaginary part of the polarizability from this data, including the ionization continuum as well as the unresolved lines above level m. From this data we obtain the real part of the polarizability by means of a numeric Kramers-Kronig relation. We are then able[6] to compute the full ground state polarizability from equation 5.11 at any photon energy $\hbar\omega$. The resolution however will be limited by the experimental resolution of the oscillator strength at photon energies close to the ionization continuum ($\lambda < 81.61\,\text{nm}$). We finally obtain the pressure dependent refractive index from the atomic polarizability by equation 1.18 in assuming the ideal gas law for the number density.

This calculation, based only on measured values for the absorption cross sections, yields values of the index of refraction, that differ less than 1% from the Sellmeier equation approach within it's valid spectral regime [80] (see Fig. 5.3). Also with respect to experimental data (shown by black points in Fig. 5.3), this low error persists.

Our experiments are conducted in wavelength region $(101 < \lambda < 104.2)\,\text{nm}$. The calculated refractive index for both models is shown in the inset of Fig. 5.3.

[6] We assume that the result of the Kramers-Kronig Transformation can be represented as an infinite sum over the atomic states $n > m$ and thus be appended to the already computed part of the sum for $n \leq m$.

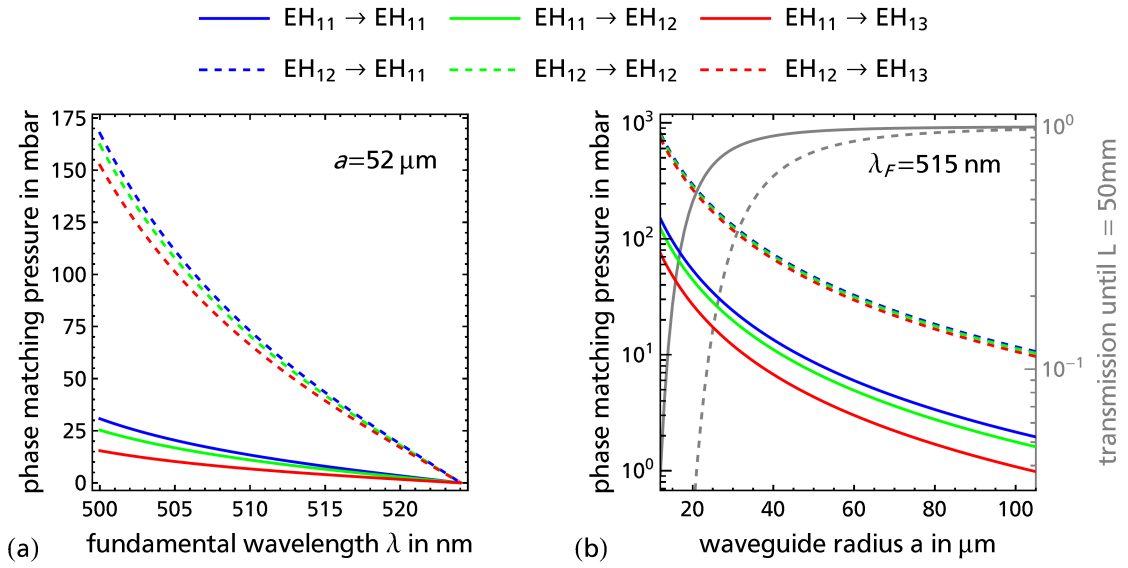

Figure 5.4: (a) Phase matching pressure for frequency up-conversion of laser pulses guided inside the EH_{11} mode (solid lines) and the EH_{12} mode (dashed lines) towards the fifth harmonic, guided inside the three lowest modes of a waveguide (made of fused silica glass) with radius $a = 52\mu$m. (b) Dependence of the phase matching pressure at $\lambda = 515$ nm on the waveguide radius a. The transmission of the fundamental radiation through a $L = 50$ mm waveguide is shown for EH_{11}(solid) and EH_{12} (dashed) gray lines (right abscissa).

Here a significant difference between the extrapolated Sellmeier equation and our enhanced model is evident. The discrepancy due to atomic transitions not modeled in the Sellmeier equation increases towards higher photon energies. As our model is based on a larger set of experimental data without any fitting we are confident, that in this spectral region it yields results that are much closer to reality than the empirical model.

5.2.5 Phase matching conditions for harmonic generation in argon

With knowledge of the refractive index, we can now compute the gas pressure for phase matched harmonic generation for the lowest order waveguide modes. Figure 5.4. (a) shows the argon pressures for phase matching in an $a = 52\,\mu$m waveguide. For harmonic generation starting from the lowest mode EH_{11} of the fundamental, quite low pressures are required to cancel the positive waveguide dispersion by the negative gas dispersion. When the harmonic is guided in a higher mode than the fundamental, even fewer gas pressure is required, as the propagation constant of mode is higher. When harmonic generation starts from a higher mode of the fundamental, much higher phase matching pressures are possible due to the stronger confinement. The particular pressure for a given mode combination is again dependent on the target mode for the harmonic.

The higher phase matching pressures possible seem to be a suitable approach towards higher conversion efficiency, but come with the disadvantage of higher losses and a significantly reduced input coupling efficiency due to the shape mis-

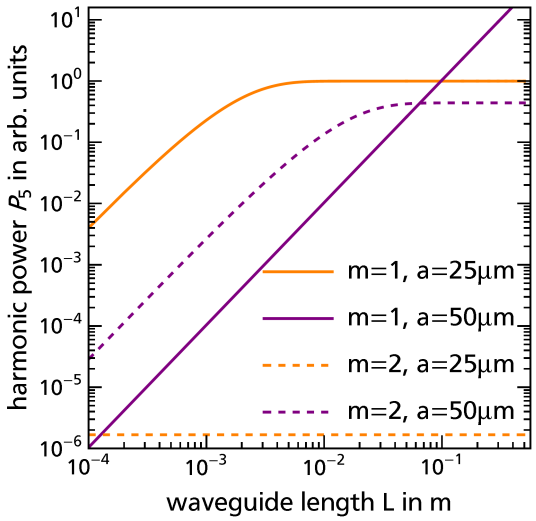

Figure 5.5: Variation of the fifth harmonic power vs. waveguide length for core radii $a = 25\,\mu$m (orange) and $a = 50\,\mu$m (purple), assuming a cw fundamental electric field of constant power, perfectly coupled to the EH_{11} (lines) or EH_{12} (dashed) waveguide mode. The results shown by solid lines are calculated with the corresponding loss and gas density for phase matching between the lowest EH_{11}waveguide modes. Dashed lines depict results for the $EH_{12} \rightarrow EH_{12}$ phase matching. Attenuation of the harmonic as well as harmonic generation inside other EH_{1m} modes is neglected.

match between a Gaussian input beam and the shape of the individual modes. Higher dispersion by tighter confinement is also achieved inside a waveguide of smaller bore (compare Fig. 5.4 (b)).

To visualize the effect of the waveguide dimensions (bore and length) as well as the coupling of the fundamental to different modes on the fifth harmonic yield, we employ here a very simple undepleted pump model. We start with a continuous wave pump field, assuming constant power coupled exclusively to the EH_{11} or EH_{12} mode and a constant gas pressure $p(z) = p^{PM}_{m,m'}(a,\omega_1)$ equal to the phase matching pressure of the corresponding mode combination:

$$I_5 \propto \left| \chi^{(5)}_{(5\omega,\omega,\omega,\omega,\omega,\omega)} \cdot \int_0^L E_1^5 dz \right|^2 \tag{5.13}$$

$$\propto \left| p^{PM}_{m,m'}(a,\omega_1) \cdot \left(\frac{1}{a} \cdot \int_0^L \exp(-\mathrm{Im}[\gamma_m(a,\omega)\cdot z])\, dz \right)^5 \right|^2 \tag{5.14}$$

The fundamental intensity at the waveguide entrance for constant pump power scales as a^{-2} and is attenuated exponentially. The source of the harmonics is then the electric field $E_1 \propto a^{-1}\exp(-\mathrm{Im}[\gamma_m(a,\omega)\cdot z])$ times the nonlinear susceptibility, which is proportional to the phase matching pressure $\chi^{(5)} \propto p^{PM}_{m,m'}(a,\omega_1)$. The generated fifth harmonic power $I^5 a^{-2}$ is shown as a function of the waveguide length L in Fig. 5.5. Due to the strong attenuation of the fundamental, inside the $a = 25\,\mu$m waveguide (orange) the harmonic power saturates already before 50 mm waveguide length L. Harmonic generation from the EH_{12} mode at this radius even saturates before $L = 100\,\mu$m. The $a = 50\,\mu$m waveguide exhibits a much lower gain per propagation length due to the lower phase matching pressure, but the lower loss leads to a saturation well after $L = 1$ m, such that the L^2 dependence of the harmonic power overcompensates the lower particle density. For short ($L < 60$ mm) waveguides at this radius, harmonic generation starting from the EH_{12} mode could be even more efficient[7].

[7]This very simple model does not account for harmonic radiation other than $|E_{5,1}|^2$, but still

For our experiment we will focus on waveguides of 50 μm radius as those exhibit good efficiency at a moderate length of several centimeters that can be handled easily. At the same time efficient input coupling is possible with Gaussian spot sizes that can still be characterized by means of standard image sensors.

5.2.6 Numerical simulation

The nonlinear wave equation generates a huge set of coupled differential equations for the mode amplitudes. We developed a numerical approximation of the experiment starting from equation 5.7, to compare the experimental results with theoretical expectations including nearby atomic resonances. In a numeric approach similar to Tani et al. [78], we solve the set of differential equations for the fundamental ($j = 1$) radiation guided in the four lowest waveguide modes ($m = 1..4$) as well as for the third and fifth harmonic $j = \{3, 5\}$, guided in the lowest five waveguide modes ($m = 1..5$) for all positions in z. In the equations, we use pressure-dependent nonlinear susceptibilities $\chi^{(j)}$ and propagation constants γ_m, computed for a given input peak intensity and fundamental frequency ω_1. To simplify the model in order to incorporate the dynamic level shifts, we skip the "split step" introduced in [78] and assume a single frequency laser field[8]. We later account for the temporal shape of the laser pulse: In the temporal domain, we apply an adaptive step size temporal integration with at least[9] five base points in fundamental intensity to yield the pulse energy of a quasi-cw laser pulse. To approximate the effect of the spectral width of the fundamental pulses with a residual chirp of about 1 THz/ps, as determined by our FROG setup, we calculate a set of "quasi-cw" pulse energies at five fundamental wavelengths, centered at λ_p with a step size of 0.25 nm and average the data to obtain the simulation results for pulsed excitation at the central wavelength λ_p. As the spectral components are temporally separated, their interaction is expected to be small.

This quasi cw model can not account for pulse propagation effects. This is well justified for the major part of our parameter range and also only becomes relevant for quite small detunings (see appendix A.3.4).

5.3 Waveguide preparation and characterization

In the experimental realization of phase matched harmonic generation we intend the fundamental radiation to interact with the medium only inside the waveguide, where the phase matching condition is met. Interaction before the waveguide might lead to self-focusing and alter the transversal intensity distribution for input

gives a good estimation of the expected harmonic power. We show a comparison of the two coupling cases for our 55 mm long waveguide in Fig. A.5 in the appendix.

[8]The numerical MATLAB code to generate and solve the coupled differential equations for a continuous wave electric field at given input parameters was developed by Xavier Laforgue. The code is further enhanced, incorporating a gas flow model, a dynamic level shift and the data post-processing to approximate a laser pulse of finite temporal and spectral width.

[9]We determine the error of the temporal integration to be well below 10% when compared with a temporal integration with more than 60 base points in fundamental intensity.

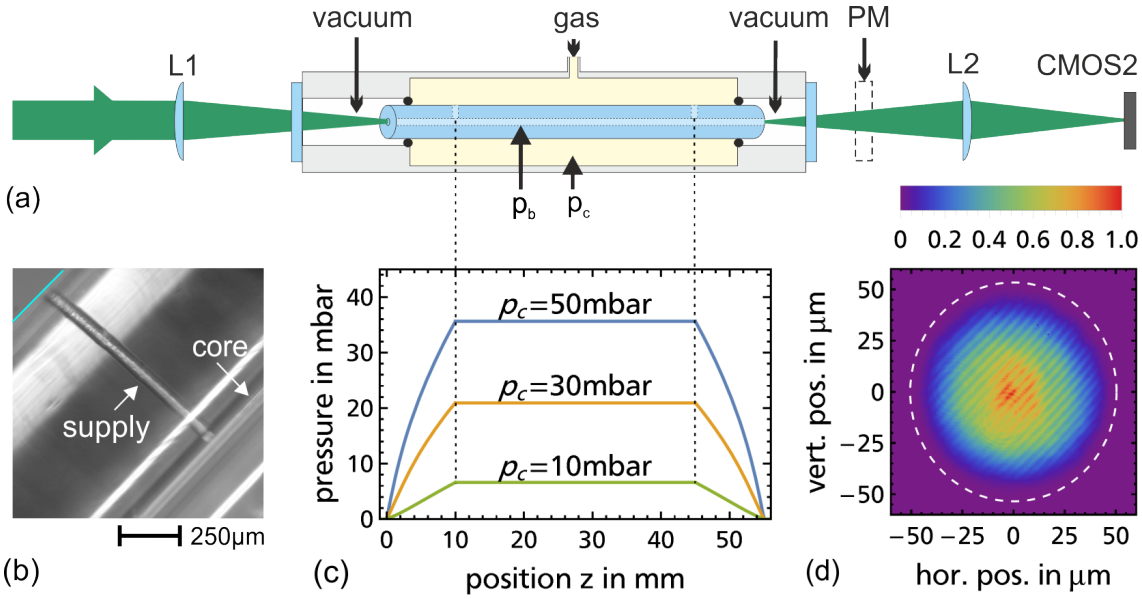

Figure 5.6: (a) Waveguide assembly with three chamber setup for gas supply, mounted inside the characterization setup. L: lens; PM: power meter; M: mirror; CMOS: image sensor (b) Gas supply channel etched from the outside (cyan line) towards the waveguide bore (image tilted 45° counter clockwise). (c) position dependent gas pressure inside the waveguide for different chamber pressures. (d) False color image of the waveguide exit, showing the intensity distribution of the fundamental mode at optimal coupling.

coupling. After the waveguide a low absorption beam path towards the detector is required for efficient detection. In particular, interaction with air or other gas species of low ionization threshold is to be prevented. These design considerations can be met by a waveguide, consisting of three segments of glass capillaries, aligned onto a common optical axis. The two outer sections seal an interjacent chamber which can be pressurized by the gas. Two small separations between the outer and the longer central segment serve to infuse the gas inside the core of the capillaries, forming a constant pressure section in the middle segment and pressure slopes towards vacuum inside the outer segments. This setup is common [32], but perfect alignment of the capillary cores to each other is crucial to maintain the desired mode structure and minimize the coupling loss between the individual sections [86]. Also the separation has to be kept of the order of waveguide diameter $2a$ to not introduce mode mixing.

It has been shown that preparing quartz glass capillaries with transversal holes for gas supply is a promising approach towards high transmission and a constant mode structure, when the holes are about the same size as the waveguide bore and smoothly interface with it [86]. The alignment procedure is eliminated and the waveguide can be integrated into the vacuum system in one piece.

We fabricate our waveguide from a UVFS capillary[10] with a length of 55 mm and a nominal bore radius of 50 μm. The capillary is processed by laser-induced etching [87] to provide two gas supply channels of 33(3) μm radius, each 10 mm

[10] supplied by Hilgenberg GmbH, Germany

from its extends[11] (see Fig. 5.6 (b)). After the etching we find the bore to be slightly elliptic with an average radius a = 52(2) μm and an aspect ratio of 1.06(3) (as indicated in Fig. 5.6(d) by a white dashed line). The waveguide is then air-tightly mounted inside a holder with a 3 chamber system (see Fig. 5.6 (a)), providing a chamber of tunable gas pressure[12], while maintaining $p < 0.1$ mbar at either ends of the waveguide by means of a turbo-molecular pump. The assembly is mounted on gimbals, rotating around the waveguide entrance, to align it with the laser in all spatial dimensions as well as the propagation direction[13]. The mounted waveguide is inspected by coupling a spatially filtered, frequency doubled Nd:YVO cw laser ($\lambda_{cw} = 532.1(1)$ nm)[14] focused (L1) to a Gaussian waist of $w_0 = 33.7(5)\,\mu$m. A high transmission of 92(1) %, compared to a theoretical maximum of 97 % is verified. The exit of the waveguide is imaged onto a CMOS image sensor by L2. The intensity distribution exhibits a distortion free mode profile (see Fig. 5.6 (d)) at the output[15]. Both, the high transmission as well as the symmetric intensity distribution at the exit (very close to EH_{11}mode) indicate, that the design requirements of the waveguide assembly are met.

5.4 Experimental setup

For generation of VUV light, the waveguide assembly is mounted to a specially designed 0.2 m constant deviation vacuum monochromator[16] such, that the exit of the waveguide lies in the object plane of the concave grating. The radiation enters the vacuum spectrometer through a 5 mm diameter aperture serving to further reduce the gas pressure inside the spectrometer to $p < 10^{-3}$ mbar.

We tune the center wavelength of the laser system between $\lambda_1 = 506\ldots520$ nm at a pulse length of 1.2 ps (FWHM) and bandwidth of 0.86 nm. This wavelength range is chosen to drive the atoms close to the five-photon transition between the ground state $3p^6\,(^1S_0)$ and the excited state $3p^5\,4s'\,^2[1/2]^\circ_1$ of argon, already introduced in chapter 3 yielding resonantly-enhanced fifth harmonic VUV radiation at $\lambda_5 = 101\ldots104$ nm (see Fig. 5.7). Due to spectral gain differences, the pulse length and bandwidth exhibit a statistical spread of 0.2 ps and 0.12 nm respectively. We characterize the temporal pulse profile for each fundamental wavelength in the FROG setup by 2D phase retrieval. Thanks to the spatial filtering between each amplification stage in the amplifier and inside an evacuated chamber after the amplifier, we obtain a laser beam profile with $M^2 < 1.2(1)$, which is important for efficient and consistent coupling towards the fundamental spatial mode of the waveguide.

We focus the fundamental beam with a plano-convex lens system of focal length 230 mm into the waveguide, yielding an almost perfectly round beam pro-

[11] Selective etching was done by LightFab GmbH, Aachen, Germany. The waveguide is thoroughly cleaned in distilled water and methanol to regain a clean inner surface after the preparation.

[12] measured by Pfeiffer APR250, above 1 mbar or Edwards PR10-K below 1 mbar

[13] See [M5] for further details and pictures of the vacuum setup and capillary holder.

[14] CrystaLaser CL532-025-S combined with a spatial filter to yield a M^2 value of <1.07(3)

[15] The visible fringes tilted by about 45° are caused by interference inside the sensor's cover glass.

[16] Grating: HORIBA Scientific 522-00-250, see Appendix A.2.1 for further details

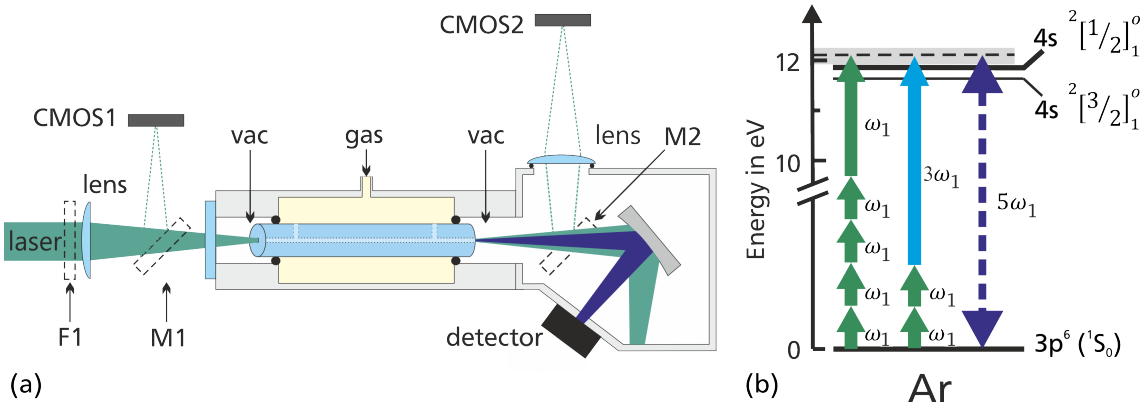

Figure 5.7: (a) Experimental setup for phase-matched harmonic generation inside the 55 mm long waveguide (blue tube) with two holes for gas inlet each 1 cm from the waveguide end. The filter F1 as well as the mirrors M1 and M2 are inserted to image the laser focus on a camera chip (CMOS1) and the waveguide end onto CMOS2 [76]. (b) Level scheme of argon with the relevant atomic levels and the tuning range (gray area) of the fundamental with respect to the 4s energy levels [76].

file with a $1/e^2$ radius of $w_0 = 32(2)\,\mu$m at the entrance of the waveguide (see Fig. 5.8, (a1)).This yields a ratio $w_0/a = 0.61$ close to the optimum of $w_0/a = 0.64$, which is expected to give the highest coupling efficiency into the lowest EH_{1m} modes of the waveguide. Inside the argon filled waveguide, the fundamental radiation drives harmonic generation towards the third and fifth harmonic mainly, as the higher harmonics (from H7) are attenuated by photo-ionization of the argon atoms. We separate the harmonic orders spatially in the vacuum monochromator and detect the fifth harmonic by a electron multiplier tube[17]. We monitor the fundamental pulse energy on a fast, calibrated photo-diode[18] and process only data points in an intensity window of ±3 % around an average fundamental intensity.

Fig. 5.8 (b1), shows the beam profile at the exit of the waveguide. As comparison with the input beam profile in Fig. 5.8, (a1) shows, the profile broadens and changes shape. We find, that the beam profile at the exit also varies with the pump wavelength, which we attribute to wavelength-dependent mode beating in the waveguide. The Super-Gaussian shape of the intensity distribution at the exit changes to a distribution with a pronounced maximum in the center, when tuning the fundamental radiation to $\lambda_1 = 506$ nm (compare Figs. 5.8 (c1) and (c2)). Hence, there are some contributions of higher order modes EH_{1m}, with $m > 1$, to the beam propagation in the capillary. From the measured intensity distribution at the entrance we determine the amplitudes of the EH_{1m} modes using the overlap integral (equation 5.6), assuming an electric field with real part only (i.e. a plane phase front) at the focal plane. Table 5.1 lists the relative mode contribution in the input pump beam profile, given by fractions of the power coupled into the modes vs. total power.

While almost 95 % are coupled to the lowest mode EH_{11}, less than 2 % are in EH_{12} and less than 1.5 % are in modes of $m \geq 3$, leaving 3 % of coupling loss. The asymmetric error bars include the dispersion of the calculated power decomposition

[17] Hamamatsu R595, with a tapered voltage divider and decoupling capacitors. See A.2.2.
[18] Becker&Hickl PDI-400

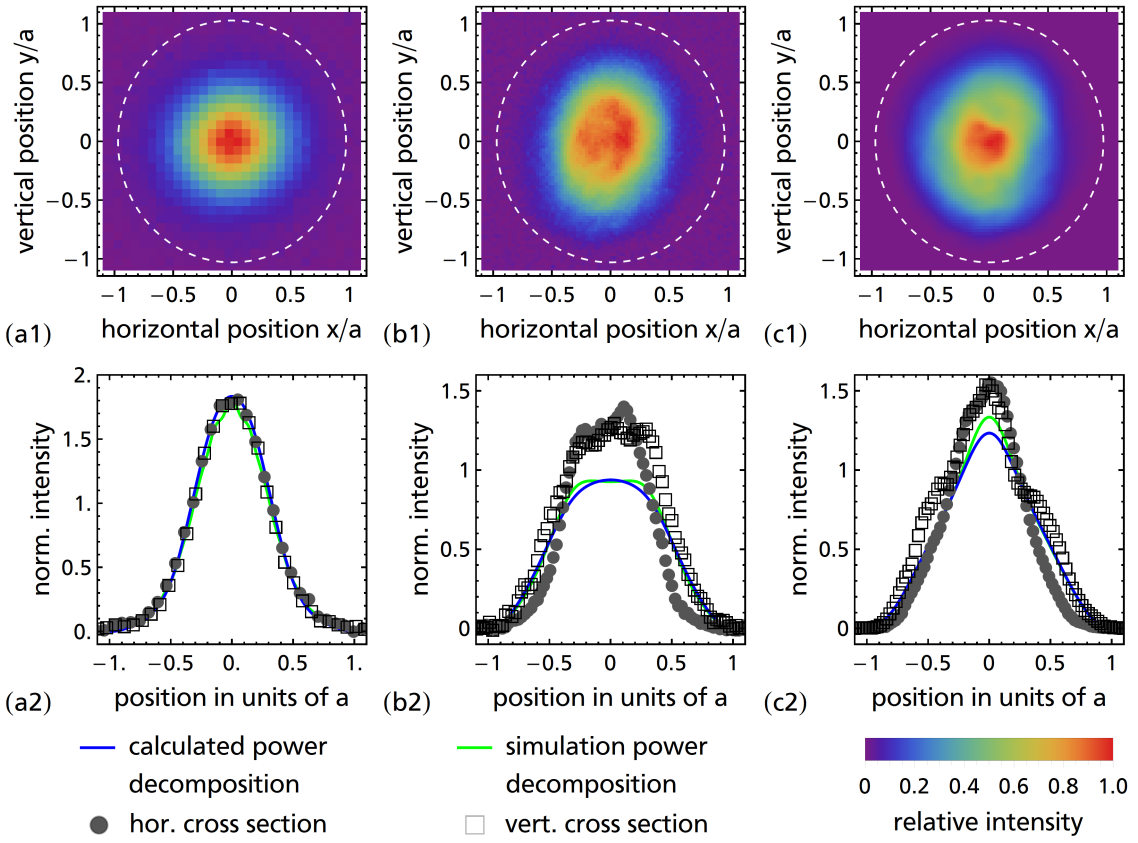

Figure 5.8: Beam intensity profiles at $\lambda_1 = 512\,\text{nm}$, before (a1) and after the waveguide of radius a =52 μm. (b1). White dashed lines show the waveguide aperture. (a2, b2) show horizontal and vertical cross-sections of the 2D intensity profiles compared with the calculated intensity distribution inside the waveguide as deduced from the experimental data (blue line), or with the slightly corrected mode amplitudes (green line) of Table 5.1. Figures (c1) and (c2) show the intensity distribution and cross sections at λ_1 =506 nm, displaying the different summation of the waveguide modes.

at all used wavelengths, as well as the effect of self-focusing in the 5 mm thick vacuum window (BK7 glass) in the beam path (see Fig. 5.7), possibly shifting the waist away from the waveguide entrance and enhancing the amplitude of the EH_{12} mode vs. EH_{11} and EH_{13}.

We will discuss below, that even these small contributions of higher order waveguide modes in the driving fundamental beam result in a (on the first glance) surprisingly large contribution to the generated harmonics. We note, that for the simulations we slightly varied the mode amplitudes, as derived from the measured beam profile, to better match the simulations with the experimental data discussed in the following section. As Table 5.1 shows, the required corrections are tiny and well within in the range of the possible self-focusing. In

mode	calculated from image	used in simulation
EH_{11}	94.5(+0.5 -0.69)	94.1
EH_{12}	1.5 (+5.9-0.6)	2.9
EH_{13}	0.6(+0.2-0.5)	0.2
EH_{14}	0.3(±0.1)	0.1

Table 5.1: Modal power coupling percentage. The coupling loss is 3 %.

Fig. 5.8 (a2) the two sets of power decomposition are compared, revealing only a marginal deviation in the intensity distribution. However at the exit of the waveguide the adjusted power decomposition with increased EH_{12} power already shows a significantly better consistency with the experimental data at all fundamental wavelength λ_1. Due to the slight ellipticity of the waveguide, the horizontal intensity distribution at the exit is shallower, which enhances the peak intensity compared to the simulation without taking the ellipticity into account.

5.5 Experimental results

5.5.1 Pressure and intensity dependence of harmonic generation

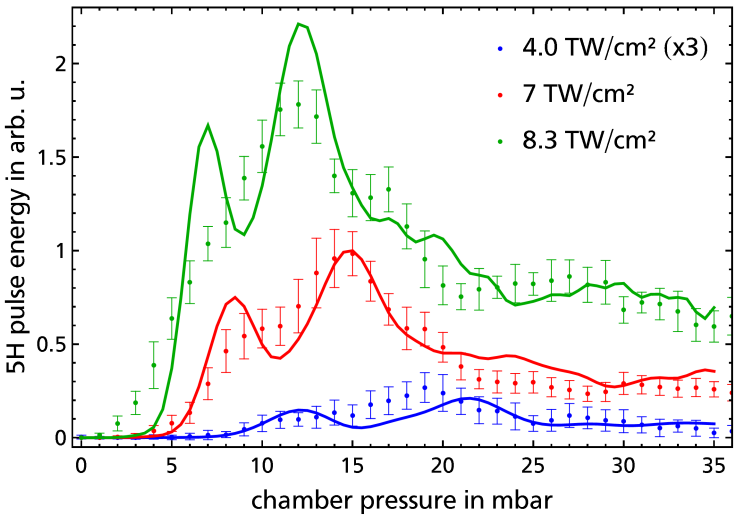

Figure 5.9: Fifth harmonic pulse energy versus chamber gas pressure at a fundamental pump peak intensity of 4 TW/cm² (blue dots), 7 TW/cm² (red dots), and 8.3 TW/cm² (green dots). The fundamental wavelength is $\lambda_1 = 512$ nm. Solid lines show numerical simulations averaged over 1 nm spectral width. Data and simulations are normalized to the peak harmonic yield at 7 TW/cm². The error bars represent the standard deviation of the single shot data at each given chamber pressure. [76]

In a first experiment we acquire the fifth harmonic pulse energy generated inside the waveguide at supply gas pressures up to 35 mbar. Fig. 5.9 shows the results at (4, 7 and 8.3) TW/cm² peak intensity at the input. We expect the conversion efficiency to reach a (local) maximum for an appropriately chosen argon pressure, satisfying the phase matching criterion $\Delta\gamma^{(5)}_{m,m'} = 0$ for each mode combination. In fact, for each pump intensity the harmonic signal reaches a maximum at a certain range of gas pressures, providing phase matched conditions. In our data, the phase matching pressure varies with laser intensity: At higher intensity, the phase matching pressure is substantially lower (i.e., with increasing intensity, the signal maxima shift to the left in Fig. 5.9. In the vicinity of the resonance we have a steep dispersion of the refractive index, thus the phase matching pressure changes with the detuning from the resonance at the harmonic wavelength λ_5

(compare Fig. 5.4 (a)). In the present situation, the laser frequency remains fixed, but the AC Stark shift drives the $4s'\,{}_2[1/2]^\circ_1$ level in argon towards higher energies. As a consequence, the magnitude of the detuning with respect to the level is reduced. The refractive index of argon decreases for the generated, single-photon resonant VUV radiation at $\lambda_5 = 102.4\,\mathrm{nm}$, while it remains almost constant at the single-photon far off-resonant pump wavelength $\lambda_1 = 512\,\mathrm{nm}$. To compensate the (positive) waveguide dispersion, we require smaller gas pressure of the (negative dispersive) argon, compared to frequency conversion at lower intensities and smaller Stark shift. The set of data enables us to determine the apparent AC Stark shift

$$\Delta\overline{W} = \Delta W_{4s\,{}_2[1/2]^\circ} - \Delta W_{3p6\,(^1S_0)} \approx 0.85\,\Phi_p$$

of the transition photon energy by a fit to the positions of maximum efficiency with respect to the fundamental intensity. This value includes the averaging over the transversal intensity profile across the fundamental beam diameter. As expected, the Stark shift is very close to the ponderomotive shift (see sect. 1.4 above). At a peak intensity of $7\,\mathrm{TW/cm^2}$ we get an "effective" shift of the exited level of $\Delta\overline{W}/h = 37\,\mathrm{THz}$ for the transition from the $4s'\,{}_2[1/2]^\circ_1$ level to the ground state. The energy shift is included in our numeric model for all (linear and nonlinear) polarizations. At each peak intensity, the harmonic pulse energy is calculated for all chamber pressures and the whole data set is normalized such, that the calculated harmonic pulse energy matches the measurement data at $7\,\mathrm{TW/cm^2}$ and 15 mbar chamber pressure. The simulation curves very well resemble the experimental data points in shape as well as the intensity dependence. At high laser intensity the optimal particle density decreases. Thus, increasing the pump intensity does not increase the fifth harmonic signal as much as if the gas pressure could remain fixed. For an estimation, we assume frequency conversion in the perturbative regime: The fifth harmonic intensity depends then upon the square of the particle density and the fifth power of the driving pump intensity: $I_5 \propto N^2 I_p^5$. Doubling the fundamental pump intensity from 4 $\mathrm{TW/cm^2}$ to 8 $\mathrm{TW/cm^2}$ should yield a fifth harmonic gain by a factor of $2^5 = 32$, but only at constant pressure (i.e. when the resonance frequency is fixed). In reality, the phase matching pressure of 12 mbar at an intensity of $8\,\mathrm{TW/cm^2}$ is only 60 % of the optimal pressure of 20 mbar at an intensity of $4\,\mathrm{TW/cm^2}$. Hence, the lower particle density yields a signal reduction by a factor of $0.6^2 = 0.36$, yielding a total signal gain of $0.36 \cdot 32 \approx 12$, confirmed by comparison of the maxima of the green and blue data points in Fig. 4. This already shows, that resonant multi-photon excitation enhances the conversion efficiency in harmonic generation, but AC Stark shifts limit the potential gain.

5.5.2 Contributions of higher waveguide modes to the harmonic yield

We will now have a closer look at the pressure dependence of the harmonic yield. As the data in Fig. 4 show, the signal maxima are rather broad, with a slow drop towards larger pressures, also exhibiting some residual oscillations. To study

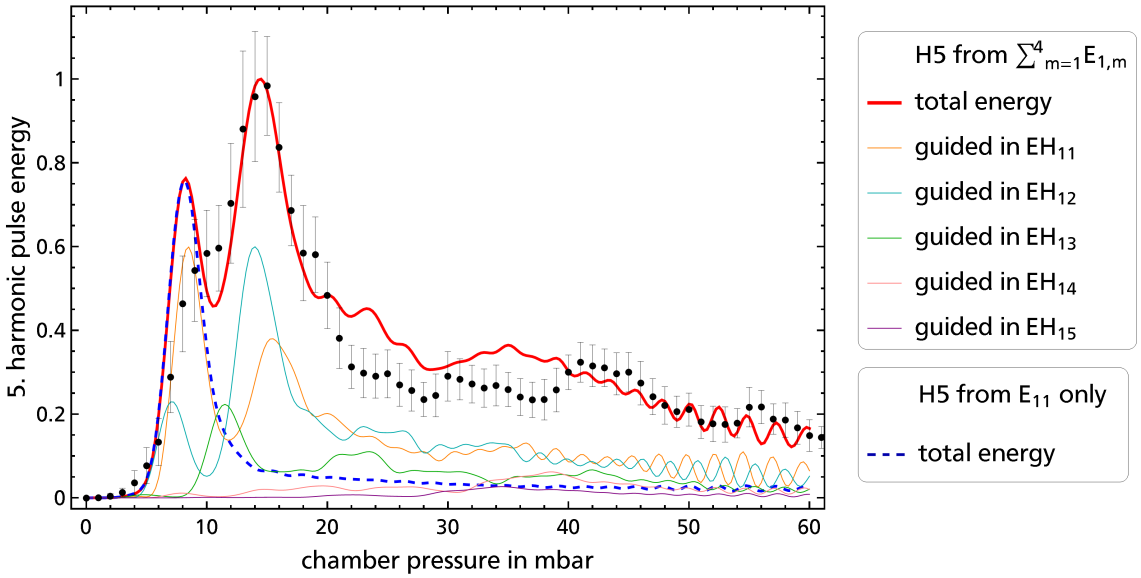

Figure 5.10: Fifth-harmonic pulse energy versus pressure. Pump peak intensity $I_1 = 7\,\mathrm{TW/cm^2}$, wavelength $\lambda_1 = 512\,\mathrm{nm}$, pulse bandwidth $\Delta\lambda_1 = 1\,\mathrm{nm}$. Experimental data (black dots) is compared to the numeric model with contributions from all waveguide modes $E_{1,1}..E_{1,4}$ (thick, solid red line) and a simulation assuming the full fundamental pulse energy to be in the lowest mode EH_{11} (thick, dashed blue line). Thin colored lines show the distribution of the generated fifth harmonic (H5) into the waveguide modes ($E_{5,1}..E_{5,5}$). [76]

details, Fig. 5.9 again depicts the harmonic signal for a fundamental intensity of $7\,\mathrm{TW/cm^2}$, along with numerical simulations of contributions from different waveguide modes to the harmonic yield, including averaged Stark shift $\Delta\overline{W}$ of the five-photon resonance.

We recall, that our fundamental beam profile is very close to the lowest order waveguide mode EH_{11} (see Table 5.1), with roughly 3 % contributions only from higher modes. Thus, on the first glance we would expect negligible contributions of the higher modes to the harmonic yield, The simple theory, based on a single waveguide mode EH_{11}(equation 5.10), would predict the sinc^2 dependence $I_5 \propto p^2\mathrm{sinc}^2(g \cdot L \cdot (p - p_{PM})/p_{PM})$, with the deviation $(p - p_{PM})$ from the phase matching pressure. It would yield a rather narrow peak around a low phase matching pressure of 8 mbar, and quick drop of the harmonic yield at higher pressures, followed by oscillations (see Fig. 5.2). The result of the numeric model with the fundamental guided in EH_{11} mode only is quite similar to this result (see blue, dashed line in Fig. 5.10). However the temporal shape of the pulse leads to harmonics generated at different fundamental intensities, and thus different detunings from the dynamically shifted resonance. This alters the phase mismatch and invokes a changed oscillation period of the generated harmonic energy vs. chamber pressure above the phase matching maximum. Consequently all features in the pressure dimension are broadened and the oscillations are averaged out. This broadening is further enhanced by the spectral intensity distribution of the pulse.

While the single mode approach describes the rise of the harmonic yield quite well for small pressures below 10 mbar, it does not fit at large pressures. We

now consider the harmonics generated in waveguide modes up to EH_{15} driven by fundamental radiation guided in higher hybrid waveguide modes up to EH_{14} (contributions given in Table 5.1). The calculated total harmonic signal shown as red line, describes the experimental data pretty well. The first maximum resulting from the phase matching of the harmonic generation $E_{1,1} \rightarrow E_{5,1}$ for the fundamental field in the EH_{11} mode around 8 mbar is still visible. In our numeric approximation, we can now study the contributions of the $E_{5,m}$ mode amplitudes to the total harmonic yield separately: The phase matching pressures (with respect to the fundamental guided in EH_{11}) for the higher order modes are smaller compared to the EH_{11} mode. Fifth harmonic generation towards the EH_{11} and EH_{13} mode is phase matched at 6 and 4 mbar chamber pressure, respectively (at 7 TW/cm²). This is the reason for the local maximum of the cyan line near 7 mbar in Fig. 5.10 and the maximum of the green line near 4.5 mbar (barely visible). The simulation also yields the larger maximum around 15 mbar, which comes from the contributions of the higher modes, although those are significantly phase mismatched with respect to the driving field at this pressure[19]. This shows, that the weak modes EH_{12}..EH_{14}, which guide only roughly 3 % of the total power, have a quite strong effect upon the total harmonic yield.

To understand this feature, in our simulations we investigate propagation along the waveguide. We find, that interference between the higher modes of the fundamental pump field strongly modulates the radial intensity distribution as well as the peak intensity at the waveguide center. This increases the overlap of the nonlinear polarization to higher modes in the fifth harmonic field, which modulates the overall harmonic gain, because most of the harmonic signal is generated in the center of the waveguide at maximal intensity.

We illustrate the effect in a simplified example: A 45 mm long waveguide with constant argon pressure is driven by cw radiation at 7 TW/cm² and the modal power decomposition of Table 5.1. The length is chosen to resemble the integrated number of argon atoms interacting with the laser field inside the experimentally realized 55 mm waveguide. We calculate the dependence of the fifth-harmonic yield with respect to the constant bore pressure p_b also for this hypothetical waveguide and extract the z-dependence of a given modal component $E_{5,m}$ at its respective maximum positions corresponding to the maxima of the cyan and orange curve in Fig. 5.10. Fig. 5.11 (b) shows the spatial variation of the fundamental intensity due to the different phase velocity of the four fundamental modes, along the propagation distance z. Three distinct regions of maximal fundamental intensity appear near z = 0, 18 and 36 mm. For the EH_{11} mode of the harmonic, frequency conversion is maximal at the phase matching bore pressure of 4.9 mbar. This corresponds to a chamber pressure $p_c = 8$ mbar for the ported waveguide. Thus, the accumulated phase difference

$$\Delta\phi^{(5)}_{1,m'}(z) = \int_0^z \Delta\gamma^{(5)}_{1,m'}(z')\,dz' \tag{5.15}$$

between fundamental and harmonic ($m' = 1$) remains close to zero along the

[19] If we would allow for a slightly larger amplitude of the EH_{12} mode in the simulation, the ratio of the two maxima at 15 mbar and 8 mbar would further increase and even better fit the exp. data.

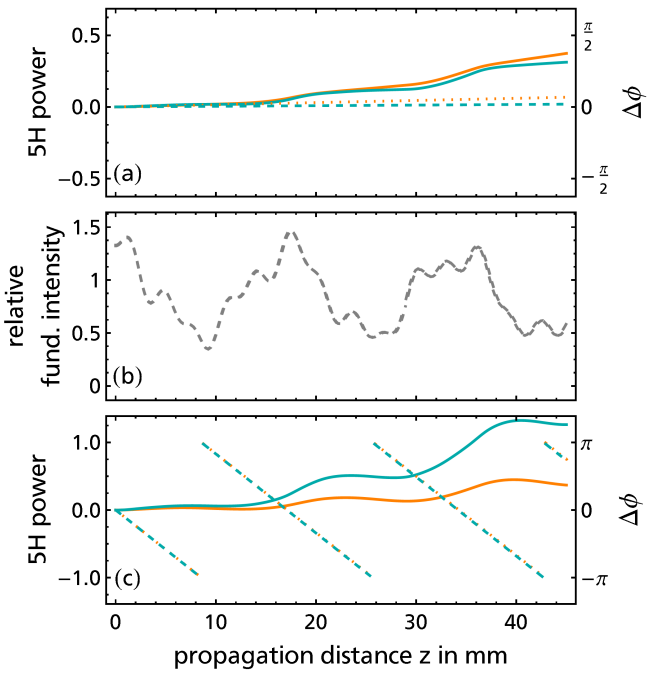

Figure 5.11: Model simulation of fifth-harmonic generation in a waveguide at constant argon pressure. (a) Solid lines show the fifth harmonic generated in mode EH_{11} at $p_b = 4.9$ mbar (orange) and EH_{12} (cyan) at $p_b = 4.0$ mbar. Dashed and dotted lines indicate the phase differences between the fundamental and the harmonic in EH_{11} ($\Delta\phi^{(5)}_{1,1}$, orange, dotted) and EH_{12} ($\Delta\phi^{(5)}_{1,2}$ cyan, dashed). (b) Fundamental intensity variation by mode beating in the waveguide; (c) phase differences and fifth-harmonic power, generated in a QPM scheme for the EH_{11} mode at $p_b = 9.3$ mbar or the EH_{12} mode at $p_b = 8.5$ mbar. [76]

waveguide (see dashed orange line in Fig. 5.11 (a)). However, the generated harmonic power of the EH_{11} mode does not simply rise quadratically (solid orange line in Fig. 5.11 (a)), as there are the three regions of maximal fundamental intensity. The effect is even more pronounced for the harmonics guided in EH_{12} mode at a phase matching pressure of $p_c = 6$ mbar ($p_b = 4.0$ mbar).

We return now to the experimentally observed and numerically confirmed efficiency maximum near a pressure of $p_c = 15$ mbar in Fig. 5.10. At a pressure of $p_c = 15$ mbar ($p_b = 9.3$ mbar) we estimate a phase difference $\Delta\phi^{(5)}_{1,1} = 5\pi$ between the fifth harmonic $E_{5,1}$ and the fundamental field $E_{1,1}$. Nevertheless, the conversion efficiency at remains high, comparable to the phase matched case. We attribute this to the modulation period of the pump peak intensity $\Lambda = 2\pi/\Delta k$ fulfilling a quasi phase matching (QPM) condition by polarization beating [88]. The intensity of the fundamental is low where back conversion occurs, reducing the loss of the harmonic significantly at $z = 9$ and 27 mm (see orange line in Fig. 5.11 (c)). The higher particle density leads to an increased nonlinear gain and compensates for the nonzero back conversion. The effect is even more pronounced for the fifth harmonic guided in the EH_{12} mode (cyan line). At $p_c = 14$ mbar ($p_b = 9.3$ mbar) the harmonic yield is more than twice the yield of the phase matched case at $p_c = 6$ mbar ($p_b = 4.0$ mbar, see Fig. 5.11 (a)), because the intensity modulation in the waveguide center enhances the nonlinear gain for this mode. In this case the ratio of the pressures would allow for more than four times stronger signal, but not the full length of the medium is efficiently applicable due to back conversion. Thus, when a laser with a beam waist (even only slightly) different from the ratio $w_0/a = 0.644$ is coupled to a hollow core waveguide, QPM can increase the harmonic yield. We note that if the beam exhibits a M^2 value bigger than unity, which leads to wave front distortion and imperfect coupling to the EH_{11} mode, the phase matching behavior can change significantly.

The effect of QPM by polarization mode beating was already demonstrated in high harmonic generation [86, 89–91]. Our numerical simulation predicts an increase by a factor of five in the conversion efficiency for coupling the waveguide with a beam waist of $w_0/a = 0.5$ instead of $w_0/a = 0.644$. However, as a drawback, the amplitudes for the first two waveguide modes are equal then, which causes strong interference to degrade the spatial harmonic beam profile. This disadvantage has to be taken in any case when the pump radiation is not coupled exclusively to the EH_{11} mode, as the gain of the harmonic guided in higher waveguide modes scales quite steep with the EH_{12} modal power (compare Fig. A.4 in Appendix). The only way to retrieve an almost Gaussian intensity distribution at the end of the waveguide in this case is to discriminate between the modes by choice of the gas pressure in a longer waveguide.

5.5.3 Wavelength dependence of the harmonic yield

We investigate now the harmonic yield vs. the wavelength of the driving pump laser, tuned in the vicinity of the $4s'^2[1/2]_1^\circ$ five-photon resonance in argon. The aim is to resonantly enhance the harmonic signal. As discussed above, the phase matching pressures for all modes are reduced when tuning the frequency of the pump laser ω_1 towards the five-photon resonance (see Fig. 5.4). Thus, we perform systematic measurements to monitor the harmonic signal vs. both the excitation wavelength as well as the pressure (see Fig. 5.12). The data show, that to every fundamental wavelength below 518 nm we can match a certain pressure to reach a maximum efficiency. The appropriate pressure decreases from 30 mbar at a fundamental wavelength of 506 nm to zero at a wavelength of 518 nm. Assuming the spatially averaged Stark-Shift of $\Delta\overline{W} = 0.85\Phi_p$, at a pump intensity[20] of 7(1) TW/cm² the $3p^6 \rightarrow 3p^5\,4s'^2[1/2]_1^\circ$. transition wavelength shifts from λ_5 =104.8 nm to 103.5 nm, resulting in a five-photon resonance moving to λ_1 = 517.5 nm. The shifted resonance position corresponds well with the strong decrease in the signal yield between 516 and 518 nm in Fig. 5.12. At fundamental wavelengths longer than 517.3 nm, the refractive index at the fifth harmonic flips from values smaller than unity towards normal dispersive behavior with values bigger than unity, thus preventing phase matching. Nevertheless, at lower intensities (i.e. in the wings of the pump beam profile) phase matching is still possible for quite small pressures, as the resonance shift is lower. The data confirm this expectation, as Fig. 5.12 still shows some signal above the noise background around λ_1 = 518 nm. To verify these experimental findings, we compare the data in Fig. 5.12 with a numerical simulation[21], shown in Fig. 5.12. The simulation fits very well with the experimental data. In particular the experimentally obtained VUV maxima (see black dots in Fig. 5.12) vs. pressure and wavelength are

[20] Due to dispersion of the mirrors and spectral gain differences in the amplifier, when varying the wavelength, the pulse duration of our laser system exhibited a statistical spread of $\sigma = 0.15$ ps around the mean value of τ_p =1.15 ps. To compensate for the effect, at each wavelength the pulse duration is deduced from a FROG trace. We compensate the variation in the pulse duration by slightly increased pulse power to acquire data at constant pump peak intensity, and normalize with respect to pulse area.

[21] For details on the calculation parameters see appendix A.3.1.

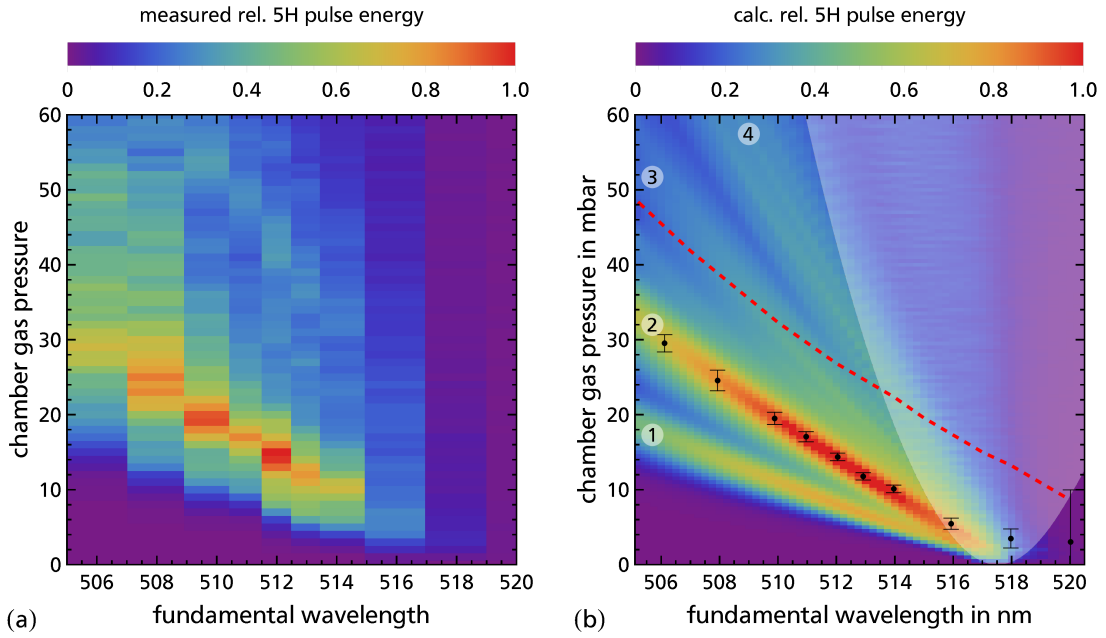

Figure 5.12: (a) Fifth-harmonic pulse energy (experimental data) versus pump fundamental wavelength and argon pressure at a pump intensity of $I_p = 7\,\mathrm{TW/cm^2}$. Compared with the simulation result (b). We assumed a fundamental peak intensity of $I_p = 7\,\mathrm{TW/cm^2}$ and averaged over a laser bandwidth of 1 nm. Black dots with error bars depict the pressures of maximal efficiency from (a). The red dashed line represents the pressure of maximal efficiency, neglecting the resonance shift. The region where the group delay at the peak intensity is larger than half the pump pulse length is shaded in gray. [76]

well described. We obtained these data by fitting to the areas of large signal in Fig. 5.12. To visualize the importance of the AC Stark shift,we also run a simulation without the energy correction $\Delta\overline{W}$. The VUV maxima of this simulation are also extracted and superimposed in Fig. 5.12 as red, dashed line. The results of the incomplete simulation strongly deviate from the experimental data. This confirms the importance of the Stark shifts upon resonance enhancements and phase matching pressures.

We note the fan-like sub-structures with four branches in the numerical simulation (see labels 1-4 in Fig. 5.12). These cannot be observed with great detail in the experimental data, as the signal "sidebands" are rather weak.

The experimental data clearly reveal the strong branch (2), resulting from the quasi phase-matching discussed above. There is evidence for branches (3) and (4) in the broader spreading of the data points at wavelengths below 508 nm and the local maxima at pressures above 40 mbar. The first maximum of the signal (branch (1)), resulting mainly from $E_{1,1} \rightarrow E_{5,1}$ phase matching, is only evident in the simulation results. This is, because the actual modal amplitudes might exhibit even higher EH_{12} coupling than supported from the focal spot images, leading to stronger QPM and thus a more pronounced second maximum masking branch (1).

At fundamental pump wavelengths above 514 nm the pulse bandwidth ap-

proaches the phase matching bandwidth

$$\Delta\omega_1 = \frac{2.78}{|v_g(\omega_1)^{-1} - v_g(\omega_5)^{-1}|L}$$

for the high intensity parts $I \approx 7\,\mathrm{TW/cm^2}$ of the laser pulse. At 517 nm, the phase matching bandwidth of $\Delta\lambda_{PM} = \Delta\omega_1 \cdot \frac{2\cdot\pi c}{\omega_1^2}$ =0.15 nm is already much smaller than the pulse bandwidth. At a given pressure p, only parts of the spectral bandwidth of the fundamental pulse are efficiently converted, reducing the harmonic yield. In our simulation at λ_1 =517 nm, the pulse bandwidth covers the pressure regions of all four branches, resulting in a single, averaged maximum at lower conversion efficiency. This explains the drop in harmonic pulse energy towards In the experimental data (and the spectrally averaged simulation) this is only evident in a smoothing of the four branches towards the single maximum at lower conversion efficiency. For small detuning from the resonance, the dispersion at the fifth harmonic also gives rise to a group delay $\Delta\tau_G^{(j)} = L(v_g(\omega_j) - v_g(\omega))$, shifting the harmonic pulse away from the pump pulse. Both effects occur simultaneously, resulting in longer generated pulses at the harmonic frequency.[22].While our model numeric model can to some extent account for the spectral narrowing, the lack of the temporal dimension in the calculation might lead leads to an overestimation of the harmonic yield, when the group delay is no longer negligible. We indicate the parabolic region where the group delay at the peak intensity is larger than half the pump pulse length by a gray shading in Fig. 5.12. For the interpretation of the experimental data this imposes no serious limit, as in the shaded area no large signal or specific features are observed (compare Fig. 5.12). Qualitatively the simulation still fits well also in the shaded area.

We now have a closer look into the data and simulation. In Fig. 5.13 (b) we plot the fifth harmonic signal maxima from Figs. 5.12 (a) and (b) vs. fundamental wavelength. The VUV yield increases with decreasing detuning from the Stark shifted resonance, till it reaches a broad maximum around 512 nm, and quickly drops for larger wavelengths afterwards. As in Fig. 5.12, the possible resonance enhancement is visible. The full numerical simulation (see green line in Fig. 5.13(b)) shows a similar behavior, exhibiting a smooth increase towards a broad maximum and a sharp drop for long wavelengths. However, compared to the experimental data, the wavelength position of the steep falling slope is shifted towards longer wavelength in the simulation.

Our numerical simulation permits us to study the effect of different contributions to the spectral dependence in Fig. 5.13. We start with a calculation of the fifth order susceptibility[23] for fifth harmonic generation $\chi^{(5)}_{(5\omega)}$ at low constant pressure, neglecting phase matching requirements (see gray, dotted line in Fig. 5.13(a)). The susceptibility shows a typical resonance line profile, as expected.

[22]At lower intensities in the wings of the pulse, the dispersion is much weaker, so the high group delay occurs only during a very short part of the pump pulse. This transient change in group velocity at the peak intensity is expected to modify the pulse shape of the fifth harmonic. Effectively we expect the harmonic pulse at the output of the waveguide to succeed the pump pulse by about one pulse length.

[23]For details on the calculation see appendix A.3.1.

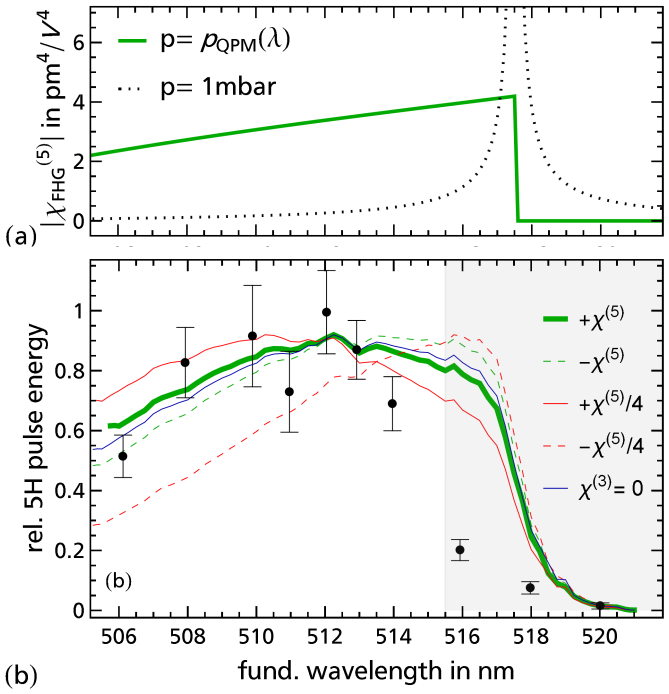

Figure 5.13: (a) Dependence of $\chi^{(5)}$ versus wavelength for a low, constant argon pressure (gray dotted line) and at the corresponding QPM argon pressure (green solid line). (b) Fifth-harmonic signal maxima versus wavelength (black dots), extracted from experimental data (Fig. 5.12 (a)). The green thick line shows the results of the full numerical simulation (Fig. 5.12 (b)). Thin lines show numerical simulations of normalized dependencies for different possible values of $\chi^{(5)}$ and without $\chi^{(3)}$ (gray). The shaded area indicates the wavelength region, where pulse propagation effects may occur (neglected in the simulations). [76]

We compare this with the spectral behavior of $\chi^{(5)}_{(5\omega)}(p_{QPM})$ at the corresponding QPM pressures p_{QPM} (see green, solid line in Fig. 5.13 (a)). The additional requirement of phase matching changes the functional dependence of $\chi^{(5)}_{(5\omega)}(p_{QPM})$ quite substantially when compared to the low pressure case. This consideration of the susceptibility $\chi^{(5)}_{(5\omega)}$ only, already reveals a qualitatively similar behavior as the experimental data in Fig. 5.13 (b). We observe, that for the QPM case, the higher possible phase matching pressure (caused by the drop of the linear index of refraction for the fifth harmonic) almost compensates the decrease of the atomic polarizability $\alpha^{(5)}_{(5\omega)}$) when the detuning from resonance increases. Nevertheless, still substantial resonance enhancement in the fifth harmonic yield remains.

To understand the actual envelope of the maximal harmonic intensity with respect to fundamental wavelength in more details, we again have to consider the phase matching bandwidth. As long as the phase matching bandwidth is sufficiently large to support the full pulse spectrum, the harmonic yield is enhanced by tuning towards the (shifted) five-photon resonance. The phase matching bandwidth (FWHM) drops from $\Delta\lambda_{PM} = 3.5$ nm at $\lambda_1 = 500$ nm to $\Delta\lambda_{PM} = 1$ nm at 514.5 nm. For smaller detunings, the conversion efficiency suffers from spectral narrowing. Thus, the simulation (see green line in Fig. 5.13 (b)) shows a deviation from the rising slope about at 513 nm and strong drop of the VUV yield beyond wavelengths of 515 nm. The experimental data data reveal a similar shape, however, the VUV signal exhibits a much stronger drop at wavelengths beyond 513 nm. The deviation between experiment and simulation is most probably caused by the additional group velocity mismatch, not accounted for in the model. It is stretching the harmonic pulse and temporally shifting it away from the pump pulse, thus further reducing the conversion efficiency. The calculated phase matching bandwidth $\Delta\lambda_{PM} = 3.5$ nm at 500 nm corresponds to a laser pulse duration in the regime of

100 fs. Thus, though we implemented our experiment with (ps) pulses, resonance enhancements in argon are possible also for shorter (fs) laser pulses.

We finally address the question, whether the fifth harmonic generation is dominated by a direct $\chi^{(5)}$ process, adding up five fundamental photons in a single step or by cascaded frequency conversion in two $\chi^{(3)}$ processes by third harmonic generation (THG) $\omega_3 = 3\omega_1$ followed by sum-frequency mixing (SFM) $\omega_5 = \omega_3 + 2\omega_1$ with two additional fundamental photons. The cascaded effect has been reported to significantly enhance efficiency [74, 92].
Our numerical simulation includes both contributions to the fifth harmonic yield. The exact results depend upon the ratio of the two conversion channels, i.e. the relative magnitudes of $\chi^{(5)}_{(5\omega)}$ and the susceptibilities for THG and FWM $\chi^{(3)}_{(3\omega)} \cdot \chi^{(3)}_{(5\omega,\omega,\omega\omega_3)}$. Our simple modeling of the fifth order nonlinearity via a generalized Miller's formula [71] can only resemble the functional behavior near the five-photon resonance. However the sign and absolute magnitude of $\chi^{(5)}$ and $\chi^{(3)}$ is only approximated. Therefore we now analyze the effect of a variation in $\chi^{(5)}$ at constant $\chi^{(3)}$. Below λ=106.6 nm, argon is positive dispersive, hence THG in our waveguide exhibits a finite phase mismatch. The third harmonic field in our waveguide yields three local maxima and minima. The average third harmonic power inside the waveguide however still scales quadratic with the argon pressure, so at high phase matching pressures (lower fundamental wavelength) the contribution of the cascaded process is bigger. The relative sign between $\chi^{(5)}_{(5\omega)}$ and $\chi^{(3)}_{SFM} \cdot \chi^{(3)}_{(5\omega,\omega,\omega\omega_3)}$ determines whether this contribution adds constructively (different sign) or destructively (same sign) to the direct fifth order process. In Fig. 5.13 (b) we show the resulting maximal harmonic pulse energies for constructive (lines) and destructive (dashes) interference, as well as a simulation without cascaded mixing ($\chi^{(3)} = 0$, blue line). If we reduce the magnitude of $\chi^{(5)}$ by a factor of 4 (i.e. a ratio of $|\chi^{(5)}_{(5\omega)}/\chi^{(3)}_{SFM}|$ <350 pm²/V²), the simulation yields a significant change of the envelope at maximum VUV energy (compare orange dashed and solid lines in Fig. 5.13 (b)), which in both cases reduces the consistency with the experimental data. Furthermore we calculate a second increase in VUV yield near 120 mbar argon pressure due to sum-frequency mixing that is not observed experimentally. No matter, which sign for $\chi^{(5)}$ we choose, the shape of the experimental data can be already well described by direct fifth harmonic generation (compare green solid and dashed line vs. blue line in Fig. 5.13 (b)). Hence for all calculations above, we used $\chi^{(5)}$ with positive sign. We conclude that in the present case the contribution of cascaded processes to the VUV power is in the range of 10% at the QPM-pressure. A much higher contribution is only expected when the strong phase mismatch of the third harmonic can be reduced.

In summary, the data in Fig. 5.12 and Fig. 5.13 clearly demonstrate resonantly enhanced harmonic generation, even when the multi-photon transition is effected by strong AC Stark shifts.

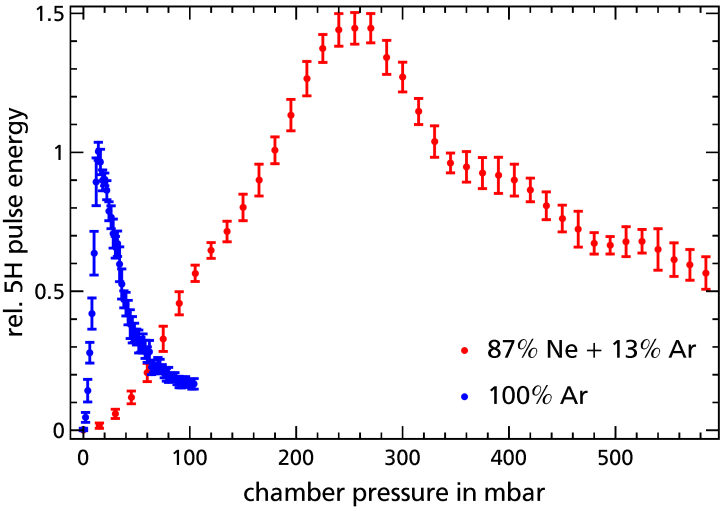

Figure 5.14: Fifth-harmonic pulse energy versus pressure in a mixture of argon with neon (blue data points), compared to pure argon (orange data points). Data taken at a fundamental peak intensity of 7.5 TW/cm² and a wavelength of λ_1 =512 nm. [76]

5.5.4 Buffer gas admixture

The possible VUV signal enhancements are limited by the rather low phase matching pressures in the regime of 10 mbar. As shown in Fig. 5.5 it is possible to further increase the signal yield by using higher intensities in tighter waveguides, increasing the waveguide dispersion and group delay proportional to $1/a^2$. However, the signal yield is limited by damping in the waveguide, scaling with $1/a^3$ [24], additional plasma dispersion, and very strong Stark shifts at high intensities. Therefore, it is convenient to fill a buffer gas in the waveguide to tailor the refractive index of the medium in favor of higher phase matching pressures. Fig. 5.5 shows the VUV signal in our waveguide, using a mixture of 13(3) % argon and 87(3) % neon. Neon offers positive dispersion to compensate the negative dispersion of argon for fifth-harmonic generation. The total phase matching shifts to 250 mbar, corresponding to a partial pressure of 32(7) mbar in argon. This permits a further signal gain of roughly 50 %.

5.5.5 Comparison with gas jet and absolute efficiency

To quantify the enhancement achieved by phase matched harmonic generation we now compare harmonic generation inside the 55 mm long waveguide with frequency conversion in our atomic jet. Figure 5.15 shows the phase matching curve for the fifth harmonic at a fundamental wavelength of $\lambda_1 = 512$ nm, as already discussed in the previous sections[25]. Superimposed is the fifth-harmonic power generated inside the atomic jet as a function of the stagnation pressure of the nozzle. For the same focus size and peak intensity of $I_1 = 7.6(2)$ TW/cm², the efficiency of the waveguide is a factor of 860(100) higher compared to the jet. We then exploit the possibility to freely reduce Gaussian spot size inside the gas jet down until $w_0 = 11\,\mu$m, to gain efficiency by the nonlinear dependence of the

[24] which could be overcome in photonic crystal fibers [33]

[25] In this experiment, a small shift in longitudinal focus position leads to lower power inside the EH_{12} mode, resulting in a slightly different shape of the curve towards higher pressure. The experimental data was acquired and processed by Maximilian Schilder, see [M4] for details.

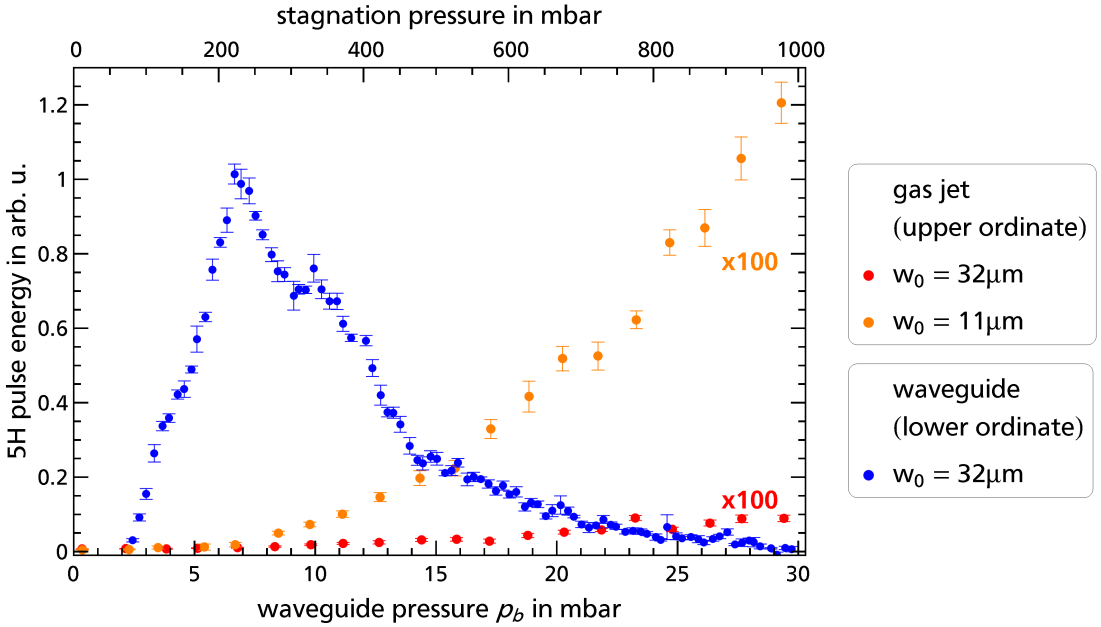

Figure 5.15: Fifth harmonic pulse energy generated inside the 55 mm long waveguide (blue data points) compared with the pulse energy generated inside an atomic jet at the same (red data points) and the maximum possible (orange) intensity, both magnified by a factor of 100. The fundamental wavelength is $\lambda_1 = 512$ nm. (Adapted from [M4])

harmonic intensity on the increased peak intensity of $I_1 = 64(1)$ TW/cm². Still, the efficiency of the waveguide is higher by a factor of 64(4).

In this work, no absolute conversion efficiencies are given, as the VUV detection setup is not absolutely calibrated. We now derive at least a lower limit for the achieved conversion efficiencies by means of an order of magnitude calculation from known values. For phase matched harmonic generation inside the waveguide at 7 TW/cm², we record about 2.5 pC of integrated charge at the anode of the EMT. With the gain $g \leq 2 \cdot 10^4$ (derived in appendix A.2.2) we calculate a number of $n_e \geq 845$ primary electrons on the cathode of the EMT. Even assuming the maximum possible diffraction efficiency of the VUV monochromator grating combined with the maximum quantum efficiency of the first EMT dynode at $\lambda_5 = 102.4$ nm (see Fig. A.2), we derive an efficiency of only $\eta_q = 1/480$ to generate a primary electron from a VUV photon. This relates to a minimum amount of $n_p \geq n_e/\eta_q = 4 \cdot 10^6$ generated VUV photons per pulse. Given the input pulse energy of 150 µJ, we achieve a minimum conversion efficiency of $\eta_{conv} \geq 5.5 \cdot 10^{-9}$. The uncertainties involved in the calculations alone allow for more than two orders of magnitude variation towards a higher efficiency. So in reality the efficiency might be of the order of $10^{-7} - 10^{-8}$.

The demonstrated efficiency is still significantly smaller than other published values, because we did not completely exploit the limits in terms of the longest waveguide for the given radius a. From our systematic studies, we conclude that in the present experiment a waveguide with a constant pressure section of $L_c = 30$ cm (compared to $L_c = 3.5$ mm) could be used, still satisfying the precondition of sufficient phase matching bandwidth ($\Delta\lambda_1 = 0.7$ nm) at a fundamental wavelength of $\lambda_1 = 505$ nm. Due to the L^2 dependence of the harmonic intensity, the efficiency

could rise by an additional factor of ≈60.

5.6 Conclusion

We presented experimental data and a numeric model, on phase matched fifth harmonic generation of (ps) laser pulses. By tuning the center frequency of the fundamental pulses close to the five-photon resonance between the ground state and the excited state $3p^5\,4s'\,^2[1/2]^\circ_1$ of argon. The AC Stark shift of the $3p^6 \rightarrow 3p^5\,4s'\,^2[1/2]^\circ_1$ transition frequency was evident by a pronounced shift of the phase matching pressure with respect to the fundamental intensity at constant fundamental wavelength $\lambda_1 = 512\,\mathrm{nm}$. Comparison with a model of the linear dispersion at the fifth harmonic frequency, an (averaged) energy shift of $0.85\Phi_p$was determined. This value is in good agreement with numerical calculations of argon level shifts above $4\,\mathrm{TW/cm^2}$.
In a systematic study of the VUV yield versus driving wavelength, and argon pressure, we demonstrated the possibility of resonance enhancement in phase matched harmonic generation. With the model well resembling the experimental data in all dimensions, we extracted the dependence of the enhancement with respect to the fundamental wavelength from experimental and simulation data and concluded a nearly linear dependence of the enhancement with the inverse of the detuning $1/|\Delta^{(5)}|$ due to the additional phase matching precondition, reducing the usable number density of argon when approaching the resonance. The spectral position of maximal efficiency, slightly detuned from the shifted resonance frequency was explained by also considering the necessary phase matching bandwidth for the given pulse length. Furthermore, we revealed a factor of two higher conversion efficiency in quasi-phase matching by fundamental mode beating, even with only less than 3 % of the fundamental radiation guided inside modes higher than EH_{11}. On the contrary, the effect of cascaded frequency mixing is estimated to only about 10 % of the absolute yield, because of strong phase mismatch of the third harmonic.

The realized phase matched geometry is found in excess of a factor of 800 more efficient than harmonic generation inside an atomic jet at a stagnation pressure of 1000 mbar. An advantage of more than a factor of 60 in efficiency persists even when the jet is driven at much higher intensity by reducing the waist of the laser in the interaction region by a factor of three. Further efficiency enhancement was demonstrated by admixture of neon gas inside the waveguide, enabling phase matching at higher number density of argon atoms.

Conclusions and future work

In the present work the frequency up-conversion of (ps) laser pulses towards the EUV spectral regime was investigated. We addressed the problem of limited conversion efficiency in prevalent gaseous nonlinear media by three approaches. On the atomic scale, the source term for the harmonic generation in form of the nonlinear polarizability was strongly enhanced by tuning the laser frequency in the vicinity of a five-photon resonance in argon. By monitoring the relative conversion efficiency for fifth harmonic generation versus the multi-photon detuning for several laser intensities of the visible driving laser, we identified pronounced AC Stark shifts of the transition frequency in excess of 50 THz, exceeding the pulse bandwidth by more than one order of magnitude already at an intensity of the order of 10 TW/cm². We concluded, that for a given peak intensity, due to the strong level shifts a transient enhancement is achieved. This enhancement occurs when the laser is tuned to a wavelength such, that the dynamically shifted level comes in resonance at intensities slightly lower than the peak intensity of the pulse. By tuning the laser accordingly, we achieved an enhancement of about one order of magnitude for the fifth harmonic and also strong enhancements of the seventh and ninth harmonic generated simultaneously. This form of resonance enhancement of multiple harmonics emphasizes the importance of intermediate resonances also in higher harmonic generation.
In a second approach, we focused on coherent control of frequency up-conversion towards the EUV regime by actively controlling the nonlinear polarization in a bi-color laser field. A four photon transition to the $5p^5\,6p\,^2[^5/_2]_2$ level in xenon is driven by intense laser pulses in the visible regime around 512 nm and can interfere with a two-photon transition, driven by the second field at a wavelength of 256 nm. By tuning the relative phase φ_F between the two fields, we achieve control of the excitation probability as confirmed by a pronounced modulation of the laser-induced fluorescence from the $5p^5\,6p\,^2[^5/_2]_2$ level. A further photon at 512 nm serves to drive fifth harmonic generation and simultaneous four-wave mixing with the UV photons, both yielding radiation at 102 nm wavelength. In systematic measurements, we examined the several preconditions to achieve maximum control in an experiment involving high nonlinear orders and ultra-short laser pulses at intensities around 1 TW/cm². As a result, we gained a visibility of 90 % in the interference of the two conversion pathways - to our knowledge the highest achieved visibility in phase control of harmonic generation so far. While coherent control can only gain a limited enhancement of less than a factor of 4, the data exhibit a convincing demonstration of the feasibility of coherent control also with ultra-short pulses at TW/cm² intensity, gaining a factor of 18 in modulation between destructive and constructive interference. Furthermore, we examined the dependence of absolute signal and control strength (visibility) concerning the

detuning from the resonance and showed a change in the temporal modulation period with respect to the detuning. In a simultaneous measurement of the excited state population and frequency conversion, both processes show similar interference with equal modulation period and large modulation depth, but phase lag of $\Delta\varphi_F = 0.03\,\pi$ between the two interferograms. We attributed this phase lag to the contribution of further atomic levels (in this case especially the Rydberg levels and the ionization continuum) to the nonlinear polarization, possibly introducing additional phase compared to the excitation channel.
We finally enhanced the $N \cdot L$ product of number density and interaction length by about a factor of 1000 by confining the gas medium inside a hollow core waveguide and balancing the gas dispersion with the waveguide dispersion. We showed that the combination of resonance enhancement and phase-matched harmonic generation at high $N \cdot L$ is possible in argon in the vicinity of the strong $3p^6 \rightarrow 3p^5\,4s'\,^2[1/2]_1^\circ$ transition. Because of the effect of the AC Stark shift of the transition frequency on the refractive index of argon at the fifth harmonic frequency, the Stark shift could be determined directly by analyzing the shift in phase matching pressure at a constant fundamental wavelength. The obtained (averaged) energy shift of $0.85 \cdot \Phi_p$, is close to the ponderomotive energy Φ_p and in good agreement with recent publications. In comparing the relative experimental conversion efficiency versus gas pressure and resonance detuning with an extensive numerical simulation, we unveiled the important contribution of a quasi-phase matching scheme resulting from the mode beating at the fundamental frequency, even with only less than 3% of power guided in modes higher than EH_{11}. Furthermore, we reproduced the resonance enhancement, which is significantly detuned even from the shifted resonance and explained the detuning and enhancement lineshape by the phase matching precondition and the required phase matching bandwidth to convert the full spectrum of the pulses. Within these constraints, we rate the investigated coupling scheme capable of resonantly enhanced frequency up-conversion of pulses as short as 100 fs. At optimal conditions, we achieved more than a factor of 800 higher conversion efficiency compared with an atomic jet operated at 1 bar of stagnation pressure and could even enhance this efficiency by another factor of 1.5 in admixing a positively dispersive buffer gas.

As a limiting factor for any resonance enhancement, we could identify the AC Stark shifts of the atomic energy levels. In a harmonic generation scheme with radiation of a Gaussian envelope in spatial and temporal dimension, the resonance condition can only be met for at a particular time and position in the intensity distribution. This change of the enhancement to a transient type strongly limits the amount of enhancement possible. When aiming for even higher efficiency in a phase-matched geometry, the shift of the excited state also affects the phase mismatch by changing the index of refraction at the harmonic wavelength. As a result, now the laser wavelength, as well as the gas pressure, has to be tuned for a given intensity. This furthermore projects the conditions of efficient conversion onto a specific transient intensity, further reducing the potential gain. To eliminate this limitation, the Stark shift of the multi-photon resonance must be compensated. One approach is to modulate the central frequency of the laser pulse according to

the intensity-dependent shift of the five photon resonance. To gain a pulse that covers the resonance shift of 7 nm at the fundamental wavelength observed at 7 TW/cm^2 inside the waveguide, a pulse with a Fourier limited length of less than 60 fs is necessary, to deliver the required bandwidth for the chirp range. A Fourier transform pulse shaper with freely adjustable spectral phase [93] could serve to obtain the matching dependence of the instantaneous frequency to "follow" the resonance shift. This setup however, can only compensate for the temporal dimension of the intensity averaging, with the spatial averaging effects remaining, which could be addressed by spatial beam-shaping to yield a super-Gaussian intensity distribution. Still, the resulting pulse would exhibit a strong chirp, that is challenging to remove especially in the EUV spectral regime.
Compensation of the resonance shift on the atomic level seems more promising. Numeric calculations in helium have recently revealed a split enhancement near the 3p level, that is attributed to a strong Autler-Townes splitting. The authors identify a strong single photon coupling between the 3p and the 2s level, leading to an Autler-Townes doublet, separated by more than 100 THz at 40 TW/cm^2 intensity. One part of the doublet is shifted below the unperturbed energy of the 3p level (i.e. overcompensating the Stark shift with respect to all other levels). This shows that tuning a second laser close to a single photon resonance between the desired level for resonance enhancement and another excited level in the atom could lead to a reduction or even a compensation of the Stark shift caused by the first laser. For perfect mode-matching, the resonance condition could be met at all positions in space and time, magnifying the enhancement effect. Unfortunately strong population dynamics driven by the second laser in such a scheme can nullify the advantages of the compensation technique on the absolute efficiency scale. The length of our waveguide was chosen to be universal for several types of experiments. With the insight of chapter 5, a six times longer waveguide could be used resulting in more than an order of magnitude increase in conversion efficiency.
Another approach towards higher efficiency is the implementation of a two-photon resonant sum-frequency mixing scheme, proven for very efficient conversion of (ns) pulses towards the EUV spectral regime [16] in a phase-matched waveguide geometry. This coupling scheme relies on a third order nonlinear susceptibility and is automatically more efficient as long as the electric field of the laser is weaker than the field inside the atom. The high frequency fundamental pulses can be generated by sum frequency mixing (SFM) and second harmonic generation in commercially available nonlinear crystals down to a minimum wavelength of 189 nm. This enables addressing the 6p levels in Xenon (as demonstrated in chapter 4) and Krypton. The resulting wavelength could be either the third harmonic or freely tunable by SFG with a tunable second laser. At higher fundamental frequency ω, due to the $1/\omega^2$ proportionality of the ponderomotive potential also the AC Stark shifts of the two-photon resonance could be much weaker. This reduces intensity dependence of the optimal experimental parameters. In the case of SFG, the long lifetime of the first excited p-levels can be even used to implement frequency mixing even after a delay of several picoseconds, completely decoupling the two-photon excitation from potential level shifts introduced by the second laser [94].

Zusammenfassung

In dieser Arbeit wurde die Frequenzvervielfachung von (ps) Laserpulsen in den EUV Spektralbereich untersucht. Wir begegneten dem Problem der geringen Konversionseffizienz in weitverbreiteten gasförmigen nichtlinearen Medien mit drei Ansätzen.
Auf der atomaren Ebene überhöhten wir die nichtlineare Polarisierbarkeit als Quellterm der Oberwellenerzeugung in großem Maße. Dies wurde erreicht, indem die Laserfrequenz in die Nähe einer Fünfphotonen-Resonanz im Edelgas Argon abgestimmt wurde. Durch systematische Untersuchung der relativen Konversionseffizienz zur fünften Harmonischen als Funktion der Mehrphotonen-Verstimmung bei verschiedenen Fundamentalintensitäten zeigten wir eine ausgeprägte Stark-Verschiebung der Resonanzfrequenz von mehr als 50 THz auf. Schon bei einer Intensität in der Größenordnung von 10 TW/cm² überschreitet diese Verschiebung die Frequenzbandbreite der anregenden Laserpulse um mehr als eine Größenordung. Daraus konnte abgeleitet werden, dass für eine eingestellte Spitzenintensität der Laserpulse durch die starken, intensitätsabhängigen Niveauverschiebungen eine vorübergehende Resonanzüberhöhung erreicht wird. Diese Überhöhung wird erzielt, wenn die Laserwellenlänge so abgestimmt wird, dass das die Niveauverschiebung bei Intensitäten knapp unter der Spitzenintensität des Laserpulses zum Erreichen der Resonanzbedingung führt. In einer experimentellen Demonstration unter diesen Bedingungen erreichten wir eine Effizienzüberhöhung von circa einer Größenordnung für die Erzeugung der fünften Harmonischen und gleichzeitig starke Überhöhungen der siebten und neunten Harmonischen. Diese gleichzeitige Resonanzüberhöhung von mehreren Harmonischen hebt die Bedeutung von Resonanzen niedriger Ordnung auch für die Erzeugung höherer Harmonischer hervor.
In einem zweiten Ansatz demonstrierten wir die Strategie der „kohärenten Kontrolle“ angewandt auf die Frequenzvervielfachung in den EUV Spektralbereich durch aktive Kontrolle der nichtlinearen Polarisation in einem zweifarbigen Laserfeld. Hierzu wurde eine Vierphotonen-Anregung des $5p^5\,6p\,^2[^5/_2]_2$ Energieniveaus in Xenon mit ultrakurzen Laserpulsen im sichtbaren Spektralbereich bei einer Wellenlänge von512 nm realisiert. Dieser Anregungspfad kann mit einer Zweiphotonen-Anregung durch Laserpulse bei einer Wellenlänge von 256 nm interferieren. Durch Variation der relativen Phase φ_F zwischen den beiden Laserfeldern konnte eine Kontrolle der Anregungswahrscheinlichkeit des $5p^5\,6p\,^2[^5/_2]_2$ Niveaus in der starken Modulation der laserinduzierten Fluoreszenz-Intensität nachgewiesen werden. Durch Aufmischen eines weiteren Photons mit einer Wellenlänge von 512 nm können in diesem Kopplungsschema gleichzeitig die Erzeugung der fünften Harmonischen und ein Vierwellenmischprozess aus zwei Photonen bei 256 nm und einem Photon bei 512 nm beobachtet werden, welche beide Strahlung

bei einer Zielwellenlänge von 102 nm erzeugen. In systematischen Messungen untersuchten wir die vielfältigen Voraussetzungen um maximale Kontrolle in diesem Experiment von hoher nichtlinearer Ordnung unter Verwendung ultrakurzer Laserpulse bei Spitzenintensitäten um 1 TW/cm² zu erreichen. Schließlich konnte ein Interferenzkontrast von 90 % in der EUV Pulsenergie erreicht werden. Dies ist nach unserem Kenntnisstand der höchste bisher erreichte Kontrast in einem Frequenzkonversions-Experiment durch kohärente Kontrolle. Die durch kohärente Kontrolle erreichbare Effizienzsteigerung ist zwar auf einen Faktor kleiner vierbegrenzt, jedoch konnte in diesem Experiment gezeigt werden, wie das Konzept auch mit ultrakurzen Laserpulsen bei Intensitäten im Bereich von TW/cm² angewandt werden kann. Hierbei konnte eine Modulation um den Faktor 18 zwischen konstruktiver und destruktiver Interferenz erreicht werden. Ferner untersuchten wir die Abhängigkeit der EUV-Pulsenergie, sowie der Kontrollstärke als Funktion der Verstimmung vom atomaren Übergang. Hierbei konnte gleichzeitig die Proportionalität der zeitlichen Modulationsperiode zur Laserwellenlänge bestätigt werden. In einer simultanen Messung der Besetzung im angeregten Zustand und der Pulsenergie der fünften Harmonischen zeigten beide Prozesse ähnliche Interferenzstruktur mit gleicher Periode und ausgeprägter Modulation, jedoch einer Phasenverschiebung von 0.03π zwischen den beiden Interferogrammen. Wir schrieben diese Phasenverschiebung auf den Einfluss weiterer atomarer Zustände (in diesem Fall vor allem der Rydberg-Zustände und des Ionisationskontinuums) auf die nichtlineare Polarisation zu. Diese zusätzlichen Kopplungen prägen dem Frequenzkonversionsprozess offenbar zusätzliche Phase gegenüber dem Anregungsprozess auf.
Schließlich konnte im dritten Ansatz in einem gasgefüllten Hohlkernwellenleiter eine Vergrößerung des $N \cdot L$ Produkts aus Teilchenzahldichte N und Wechselwirkungslänge L um circa einen Faktor 1000 erreicht werden. Durch Kompensation der Wellenleiterdispersion mit der Gas-Dispersion konnte eine resonante Überhöhung in der Nähe des starken $3p^6 \rightarrow 3p^5\,4s'^2[1/2]_1^\circ$ Übergangs in Argon unter phasenangepassten Bedingungen bei hohem $N \cdot L$ realisiert werden. Aufgrund der Auswirkung des Stark-Shift der Übergangsfrequenz auf den Brechungsindex von Argon im EUV konnte der Stark-Shift in diesem Fall aus der intensitätsabhängigen Verschiebung des Phasenanpassungsdruckes bei konstanter Wellenlänge bestimmt werden. Die errechnete (gemittelte) Energieverschiebung von $0.85 \cdot \Phi_p$ist vergleichbar mit dem ponderomotiven Potential Φ_p und damit in guter Übereinstimmung mit aktuellen Veröffentlichungen. Durch einen Vergleich der relativen experimentellen Konversionseffizienz als Funktion der Verstimmung und des Gasdrucks mit einer umfassenden numerischen Simulation konnte der wichtige Beitrag von quasi-phasenangepasster Frequenzkonversion zur erreichten Absolut-Effizienz aufgezeigt werden. Durch die verschiedenen Propagationsgeschwindigkeiten findet bereits bei Leitung von weniger als 3% der Pulsenergie in Moden höher als EH_{11} eine starke Modulation der Spitzenintensität im Wellenleiter statt, welche zu diesem Effekt führte. Weiterhin konnte auch im Wellenleiter eine resonante Überhöhung erreicht werden, welche jedoch eine signifikante Verstimmung, selbst von der verschobenen Resonanzfrequenz aufweist. Diese Verstim-

mung führten wir auf die notwendige Phasenanpassung unter Berücksichtigung der Frequenzbandbreite der verwendeten Laserpulse zurück. Innerhalb dieser Einschränkungen können im verwendeten Kopplungsschema Laserpulse bis zu einer minimalen Pulsdauer von 100 fs effizient frequenzverfünffacht werden. Unter Ausnutzung von Phasenanpassung und resonanter Überhöhung wurde schließlich die Konversionseffizienz gegenüber einem atomaren Gasstrahl mit einem Stagnationsdruck von 1 bar um mehr als einen Faktor 800 gesteigert und durch Beimischung eines positiv dispersiven Puffergases um einen weiteren Faktor 1,5 überhöht.

Appendix A

Appendix

A.1 FROG signal deformations by the nonlinear medium

During the implementation of the FROG setup [30] and the development of the reconstruction code, the FROG setup was operated with chlorobenzene as a nonlinear medium. It was chosen in favor of an high nonlinear refractive index $n_2 \approx 10^{-14} cm^2\,W^{-1}$ [95] (more than a factor of 20 higher than the value of fused silica (UVFS)). While later measurements with UVFS as medium can always be reconstructed down to G errors in the range of $(1...4) \cdot 10^{-3}$, the reconstruction of traces recorded with chlorobenzene do not converge properly. They are asymmetric and have a much longer falling slope (negative delays) as shown in Fig. A.1.

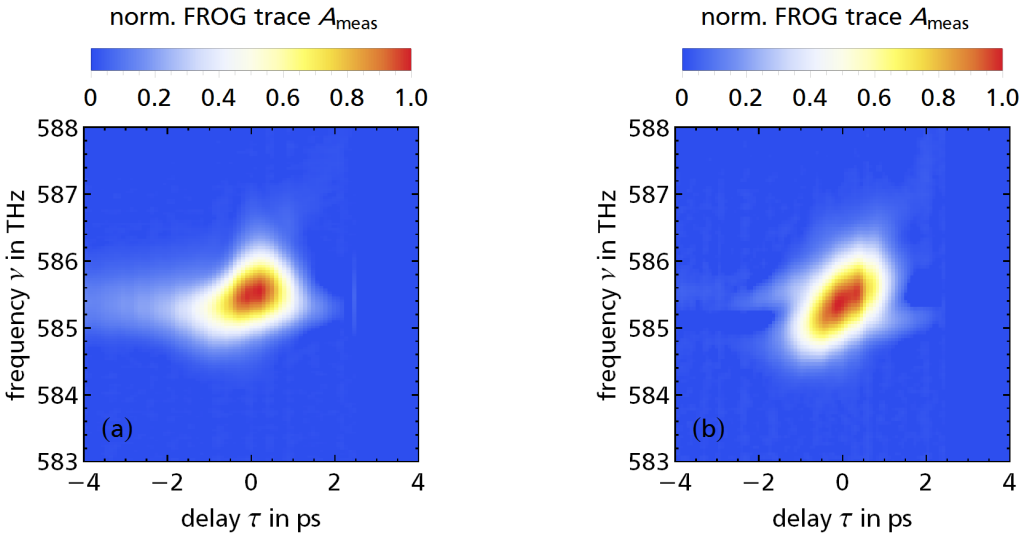

Figure A.1: FROG spectrogram with (a) chlorobenzene and (b) UVFS as nonlinear medium.

Chlorobenzene has a orientation relaxation time of $\tau_{or} = 6.3(3)\,\text{ps}$ and two additional relaxation times, $\tau_2 = 80(20)\,\text{fs}$, $\tau_3 = 400(65)\,\text{fs}$ for the nonlinear index of refraction. These decay times are shown to prolong the autocorrelation of a 100 fs (FWHM) pulse towards a FWHM of about 600 fs [96]. In our case the orientation decay time is responsible for the long tail of the spectrogram as visible in Fig. A.1 (a). This hysteresis significantly deforms the spectrogram. As a result, the FROG algorithm (assuming an instantaneous response) can not reconstruct the laser pulse. Any pulse parameters as pulse length or chirp rate deduced from

a reconstruction have an error in excess of 10 %. For pulses that have a Gaussian spectrum however it is possible to derive the pulse length from the FWHM of a fit to the autocorrelation trace multiplied by a numeric deconvolution factor [M2]. The two shorter decay times appear to not prolong this quantity more than 10 % and the longer decay time produces a rater low and asymmetric signal amplitude that does not affect the symmetric fit function too much. This is confirmed by less than 10 % positive deviation in TBP of measured Fourier limited pulses.
So the FWHM is a good measure, resulting in an uncertainty of below 10 % for the derived pulse length. For Chapter 4 and 3 all measurements were done with chlorobenzene we thus calculate the pulse length from the autocorrelation only.

A.2 Signal detection

To determine the VUV pulse energy, we use a constant deviation vacuum monochromator to separate the individual harmonics in combination with a VUV sensitive electron multiplier for detection. We now estimate the maximum possible detection efficiency of the system to derive a minimal detected photon number and hence a lower border for the conversion efficiency towards the VUV.

A.2.1 The vacuum monochromator

The vacuum spectrometers used in this work are a commercial[1] and a home made constant deviation monochromator with an opening angle $2K = 64°$. As single active element an aberration corrected concave holographic grating is used. Both monochromators share the same optical design with a groove density of $n = 1200/\text{mm}$ and operate in the $k = +1$ diffraction order[2]. For the results presented in chapter 3, the monochromator was equipped with an iridium coated grating[3] with minimal slit size for high spectral resolution. A reliable value for the total quantum efficiency of the detection system can not be given.

For the results of chapters 4 and 5 a 1200 l/mm aluminium coated grating was used[4] inside the home made monochromator with the laser focus in the object plane and a

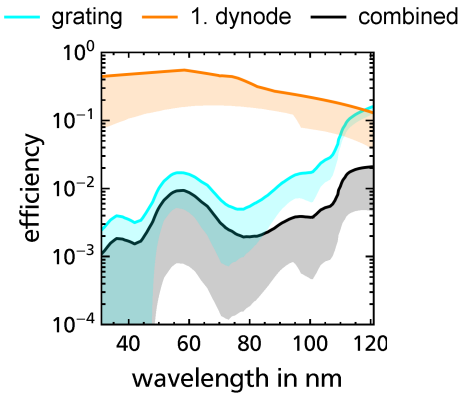

Figure A.2: Maximum efficiency of the holographic grating towards the $k = -1$ diffraction order (cyan) and quantum efficiency of the Cu-BeO dynode (orange). The combined efficiency η_q is shown in black. Shaded areas are $\pm 1\sigma$ intervals.

[1] Princeton Instruments (ACTON) Model VM-502 0.2 meter Vacuum Monochromator

[2] Optically the home made setup is identical to the ACTON design, but it incorporates removable slit assemblies to directly use the laser focus as an object, imaged onto the exit slit [M3-M4].

[3] Princeton Instruments 02-120H-03 holographic, iridium coated grating, dispersion 4 nm/mm

[4] HORIBA Scientific 522-00-250, holographic grating Al + 25 nm MgF_2 coating, dispersion 4 nm/mm. Theoretical absolute efficiency in $k = -1$ diffraction order published in [97]

1 mm wide slit in the imaging plane. The wide open slit allows all photons to enter the detector, so the transmission of the monochromator equals the absolute grating efficiency. For the $k = 1$ order we calculate the absolute efficiency by multiplying the reflectance R of the coating [98] with the calculated relative efficiency η_{rel} of the groove profile published by Carman et. al. [99]. The resulting maximal efficiency ($+1\sigma$) is shown in Fig. A.2 by the cyan line, together with the $\pm 1\sigma$ confidence interval[5]. Below 100 nm the reflectance of the coating drops to about 20 %, further decreasing towards shorter wavelength. This decrease together with strong diffraction efficiency modulations(exhibiting the first minimum at 80 nm) limit theuse of the grating to the wavelength range above 30 nm.

A.2.2 The electron multiplier tube

To detect the VUV radiation and simultaneously suppress background signal from stray light of the visible radiation we use a solar-blind electron multiplier tube[6] (EMT). It employs 20 dynodes of CuBe alloy, with the first dynode exposed to the VUV light. The quantum efficiency of this dynode is dependent on the surface oxidation, forming a thin film of beryllium oxide [100]. The pure alloy exhibits the lowest quantum efficiency, with a maximum of 17 % at about 70 nm [101]. Different oxidation methods produce a coating of up to a factor three higher efficiency [100, 101] and a more complex spectral dependence. In Fig. A.2 we show the highest possible efficiency of those data sets (orange line) together with the possible variations (shaded region). Combined with the grating efficiency we can estimate the maximum and minimum spectral quantum efficiency of the detection system η_q (black). It only varies about one order of magnitude within the spectral regime (50-120 nm) concerned in this work.

In general EMTs are designed to amplify small $< 10\mu$A DC currents [102]. In this work per pulse up to 10^4 electrons are generated from the first dynode and multiplied to yield a charge of up to 20 pC, resulting in a peak current exceeding the supply current of the voltage divider by more than a factor of 10. Consequently, electric field between the last dynodes drops, leading to saturation of the gain at high currents. Additionally the electron cloud is diffused due to “space charge effects” [102]anode. We compensate the latter by applying a negative bias voltage to the shield of the anode (resistor R21 see Fig. A.3(c)), refocusing the electrons. This results in about a factor of five higher output signal. The gain saturation was discovered after publication of the results of chapter 3 and compensated for the results of chapter 4 by calibrating the EMT versus a linear photoreceiver[7] using laser pulses at $\lambda_2 = 256$ nm for each supply voltage used in the experiment. Fig. A.3(a) shows the saturation behavior of the EMT at three supply voltages[8].The

[5]Error bars include two sharp transmission features of the coating near 100 nm and 120 nm, that appear in the $k = -1$ efficiency curve [97] and are unresolved in the reflectance data.

[6]Hamamatsu R595, older than 6 years, has been stored in ambient air several times.

[7]Becker&Hickl PDI-400 UV

[8]Due to the additional 10MΩ resistor R21 the effective supply voltage to the electron multiplication stage is only 2/3 of the supply voltage applied.

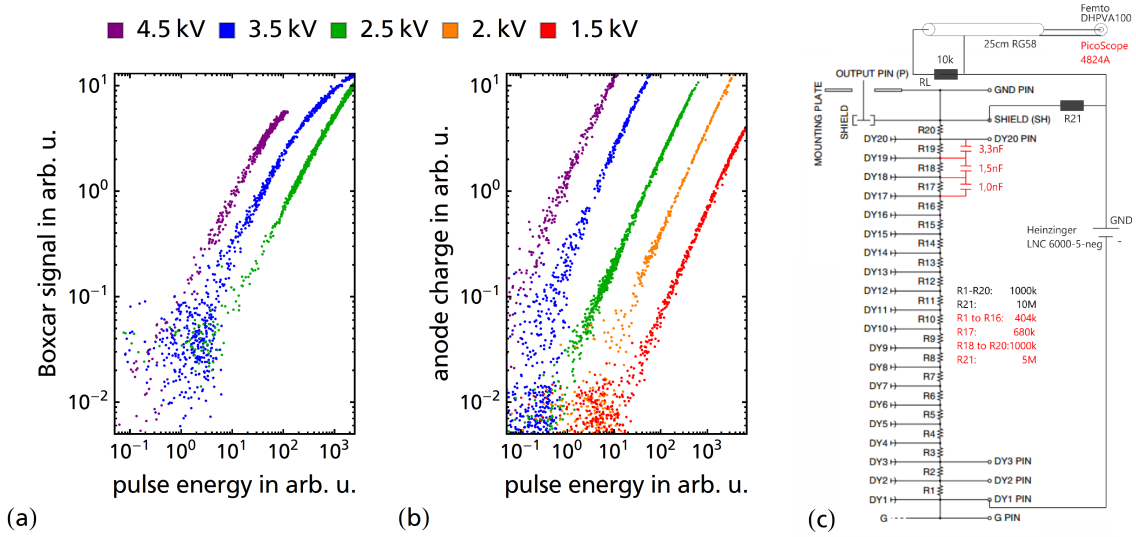

Figure A.3: Linearity of the EMT signal (a) with the stock voltage divider and additional R21 (see Fig (c) in black), amplified by 10dB and sampled with a Boxcar gated integrator; (b) with optimized tapered voltage divider and capacitors (see Fig. (c) in red). (c) Voltage diver, power supply and readout electronics of the R595 electron multiplier as used throughout this work. Resistors marked by a saw-tooth symbol are inside the vacuum system.

signal from the EMT is amplified, and sampled by boxcar gated integrator[9].

For the much higher photon numbers expected from the waveguide, we improve the linearity of the EMT by applying an optimized tapered voltage divider to the dynodes (red resistance values in Fig. A.3(c)), simultaneously increasing the supply current by a factor of two. Furthermore, decoupling capacitors are added to the last three dynodes as suggested by the manufacturer [101]. The boxcar gated integrator is replaced by a digitizer[10]. The exponential discharge of the capacitor consisting of anode and the short BNC cable is integrated to yield the generated anode charge shown in Fig. A.3(b) vs. the UV pulse energy at 256 nm. This signal exhibits virtually no saturation for output charges below 20 pC (equivalent to a signal of about 10 in Fig. A.3(b) ff.). The calibration process is omitted for the results of chapter 5 as UV pulses of known energy for calibration are not available.

We now use two ways to estimate the EMT electron gain:

1) At the highest supply voltage U_{CG} between cathode and ground, we assume the maximum shot noise acquired within the e^{-1} fall time of the EMT output voltage of $t_e = 463$ ns to correspond to one primary electron. The integrated charge $q_n = 13$ fC corresponds to $g_{SH}(4.5\,\text{kV}) = 7.8 \cdot 10^4$ secondary electrons generated and hence is the maximum gain of the EMT. From the measurements of A.3(b) we can derive the gains at the other supply voltages U_{CG} between the cathode (DY1) and ground (GND) The values calculated are much lower than the specifications. We attribute the lower gain to degradation of the dynodes by air and moisture, as well as degradation due to photon and electron bombardment [101].

2) We adapt the specified gain curve $g_M(U)$ with respect to the supply voltage

[9] amplifier: FEMTO DHPVA-100, 10dB; integrator: SRS SR250

[10] Pico Technology PicoScope 4824 terminated with a load of 10kΩ

supply voltage U_{CG}	1.5 kV	2 kV	2.5 kV	3.5 kV
from shot noise	57	341	$1.8 \cdot 10^3$	$2.0 \cdot 10^4$
$g_M(U_{CS})^{0.57}$	10	71	344	$3.8 \cdot 10^3$
$g_M(U_{CS})$	53	$1.8 \cdot 10^3$	$2.8 \cdot 10^5$	$1.9 \cdot 10^6$

Table A.1: Gain of the linearized electron multiplier R595 estimated from different sources

between the cathode (DY1) and ground (GND) given in [102]. In our case the effective supply voltage for the acceleration is $U_{CS} = 0.67 \cdot U_{CG}$ between cathode and shield. The calculated gains $g_M^d(U_{CS})$ at several U_{CG} voltages are given in Table A.1. We can reproduce the measured relative gains of Fig. A.3 (b) best, when a degradation factor of $d = 0.57$ is assumed. From the adjusted function, we calculate an estimated gain of $g_M^d(4.5\text{kV}) = 2.2 \cdot 10^5$. This value is of the same order of magnitude as the gain estimated from the shot noise. The same holds true for the gains computed at other U_{CG} voltages presented in Table A.1.

A.3 Model for harmonic generation in a waveguide

A.3.1 Calculation of the nonlinear polarization

To calculate the harmonic electric field in each mode, equation 5.7 has to be solved. To obtain a solution, we require the nonlinear polarization $\bar{P}_{j,m}^{NL}$, oscillating at frequency ω_j , that is coupled to the m^{th} mode. We first calculate the total polarization arising from the total of the electric fields $\overline{\overline{E}}_j = \sum_m \bar{E}_{j,m}(r,z)$ at frequencies ω_j, including the different modal propagation constants $\gamma_{(j,m)}$. We reduce the nonlinear polarization to the terms at highest amplitude (i.e. the highest powers of the fundamental field $E_{(1,m)}$). This simplification (as presented below) was compared to the versus the full polarization model and found to differ less than 10% for each data point. For the fifth harmonic frequency we consider direct fifth harmonic generation via$\chi^{(5)}$ as well as cascaded generation of the fifth harmonic from a field at $\omega_3 = 3\omega_1$, generated in the waveguide at shorter propagation distances. We obtain the nonlinear polarizations $\overline{P}_{j,m}^{NL}$ at the three frequencies by setting the source in the coupling relation to:

$$\overline{\overline{P}}_1^{NL}(r,z) = \epsilon_0 \left(3\chi^{(3)}_{(\omega,\omega,-\omega,\omega)} \overline{\overline{E}}_1 |\overline{\overline{E}}_1|^2 + 10\chi^{(5)}_{(\omega,\omega,-\omega,\omega,-\omega,\omega)} \overline{\overline{E}}_1 |\overline{\overline{E}}_1|^4 \right) \tag{A.1}$$

for the fundamental, only taking self-phase modulation into account. For the third harmonic, despite of THG, we also include cross phase modulation:

$$\overline{\overline{P}}_3^{NL}(r,z) = \epsilon_0 \left(3\chi^{(3)}_{(3\omega\omega,\omega,\omega)} \overline{\overline{E}}_1^3 + 5\chi^{(5)}_{(3\omega,-\omega,\omega,\omega,\omega)} \overline{\overline{E}}_1^3 |E_1|^2 \right) \tag{A.2}$$

The fifth harmonic nonlinear polarization is simplified to:

$$\overline{\overline{P}}_5^{NL}(r,z) = \epsilon_0 \left(3\chi^{(3)}_{(5\omega.\omega,\omega,3\omega)} \overline{\overline{E}}_1^2 \overline{\overline{E}}_3 + \chi^{(5)}_{(5\omega,\omega,\omega,\omega,\omega,\omega)} \overline{\overline{E}}_1^5 \right) \tag{A.3}$$

From these radially dependent polarizations we finally calculate the complex nonlinear polarization amplitude to insert in equation 5.7 by the overlap integral

$$\overline{P}^{NL}_{j,m}(z) = \frac{\int_0^a J_0(u_{1m} r \cdot a^{-1}) \cdot \overline{\overline{P}}_j(r,z) r \, \mathrm{d}r}{\int_0^a J_0^2(u_{1m} r \cdot a^{-1}) r \, \mathrm{d}r},$$

in analogy to eq. 5.6. The square modulus of the relative nonlinear gain

$$\eta_m^{(5)} = \frac{\left| \int_0^a P^{NL}_{5,m} J_0(u_{1m} r \cdot a^{-1}) r \, dr \right|^2}{\int_0^a |\overline{\overline{P}}_5(r)|^2 |^2 r \, \mathrm{d}r \cdot |J_0(u_{1m} r \cdot a^{-1})|^2 r \, \mathrm{d}r}$$

of each waveguide mode is shown in Fig. A.4 for the fundamental radiation coupled to the lowest two modes EH_{11} and EH_{12}. The potential harmonic yield of mode m at phase matched conditions is roughly proportional to $\eta_m^{(5)}$. When the fundamental is perfectly coupled to the EH_{11} mode, the most pure modal decomposition of the harmonic beam is to be expected, but still almost 35 % of harmonic power can potentially be generated in the EH_{12}mode. With increasing relative amplitude $E_{1,2}/E_{1,1}$, the possible contribution of higher waveguide modes to the fifth harmonic power increases quite rapidly.

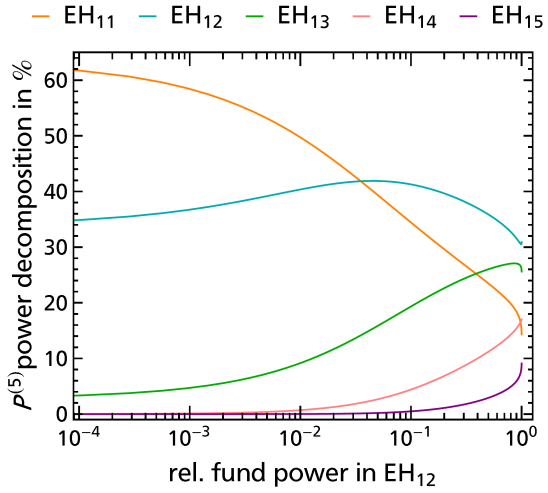

Figure A.4: Coupling efficiency $\eta_m^{(5)}$ of the fifth order polarization $P^{(5)}(5\omega)$ towards the waveguide modes versus the fraction of pump power coupled to the EH_{12} mode.

A.3.2 Calculation of the nonlinear polarizability

We calculate the nonlinear susceptibilities from the generalized Miller's formula [103], an empiric model only requiring knowledge of one-photon dipole transition moments. The susceptibilities are characterized by a factor $A_p$derived from known values [104–108] of the susceptibility $\chi^{(3)}_{(\omega,\omega,-\omega,\omega)}$ and $\chi^{(5)}_{(5\omega,\omega,-\omega,\omega,-\omega,\omega)}$ for the nonlinear refractive index n_2 [42, 109, 110] and n_4 [105, 106, 109] in the infrared and the extrapolated towards the visible spectral regime.

$$\chi^{(3)}_{(\omega_1,\omega_2,\omega_3,\omega_4)} = A_p^{(3)} \cdot N(p) \cdot \epsilon_0^{-1} \prod_{i=1}^{4} \alpha^{(1)}(\omega_i),$$

$$\chi^{(5)}_{(\omega_1,\omega_2,\omega_3,\omega_{4,}\omega_5)} = A_p^{(5)} \cdot N(p) \cdot \epsilon_0^{-1} \prod_{i=1}^{6} \alpha^{(1)}(\omega_i)$$

These simple model functions rely only on the linear susceptibility. The spectral dependence of the fifth order susceptibility $\chi^{(5)}_{(5\omega,\omega,\omega,\omega,\omega)}$ will therefore quite accurately resemble one-photon and five-photon resonances[11], but fail to exhibit intermediate two-photon, three-photon and four-photon resonances, that would appear in the full quantum mechanical calculation. For the case of our coupling scheme we expect these resonances to only contribute a nearly frequency independent factor (accounted for by a pre-factor A_p), as the detuning to the lowest two photon allowed transition is more than 3 fundamental photon energies. The obtained values of the nonlinear susceptibilities used in the simulation are given in Table A.2. Sign and absolute magnitude of n_4 at infrared and mid infrared wavelength are still a matter of debate in the literature [104–108]. Hence our value of $\chi^{(5)}$has a large uncertainty. We show and discuss the potential variations in relative magnitude and sign of $\chi^{(5)}$ vs. $\chi^{(3)}$ in Fig. 5.13.

nonlinear susceptibility	calculated value (λ_1 =512 nm)
$\chi^{(3)}_{(3\omega\omega,\omega,\omega)}$	$5\cdot10^2\,\mathrm{pm^2V^{-2}}$
$\chi^{(3)}_{(\omega,\omega,-\omega,\omega)}$	$4\cdot10^2\,\mathrm{pm^2V^{-2}}$
$\chi^{(3)}_{(5\omega.\omega,\omega,3\omega)}$	$-7\cdot10^2\,\mathrm{pm^2V^{-2}}$
$\chi^{(5)}_{(5\omega,\omega,\omega,\omega,\omega,\omega)}$	$1\cdot10^2\,\mathrm{pm^4V^{-4}}$

Table A.2: Nonlinear susceptibilities applied in our numerical simulation [76]

A.3.3 Harmonic generation from a single fundamental mode

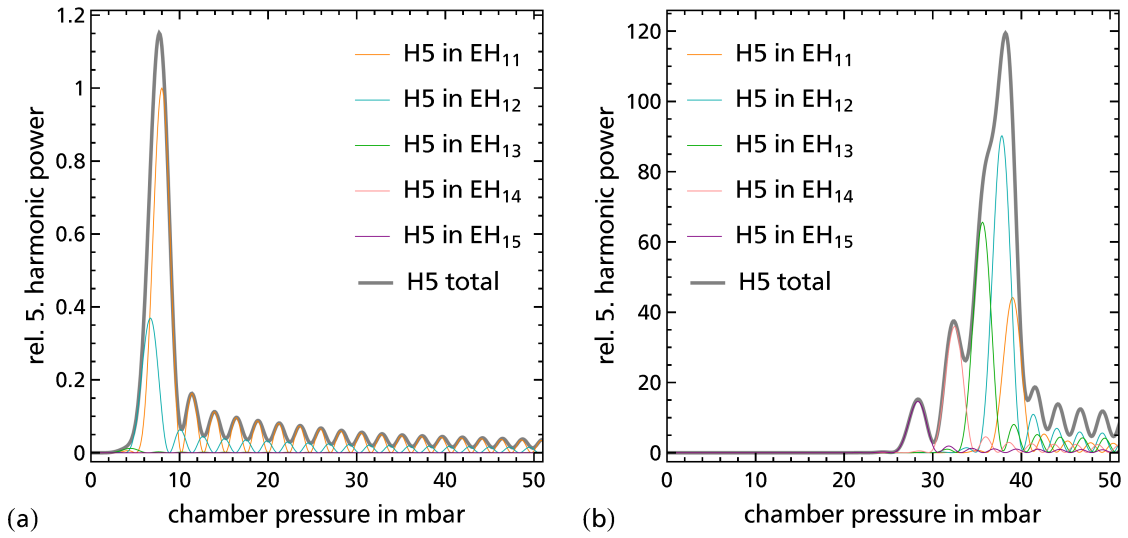

Figure A.5: Harmonic power generated from a cw pump field ($\lambda_1 = 512\,\mathrm{nm}$) coupled to the (a) EH_{11} mode or (b) EH_{12} mode of the 55 mm long waveguide (chapter 1.1) at 7 TW/cm².

To visualize the effects of input coupling and the temporal pulse shape, Fig. A.5 (a) shows the calculated harmonic power of a hypothetical cw pump laser perfectly coupled to the EH_{11}waveguide mode. The intensity is chosen to resemble the peak intensity of 7 TW/cm² for the EH_{11} mode as used in chapter 5. All phase

[11] as our refractive index mode is in very good agreement with experimental data

matching pressures are comparable to those of section 5.5.1). In this case however the detuning is fixed because of the constant intensity. The harmonic power is maximal a the phase matching pressure of $p_c = 8\,\mathrm{mbar}$ for $EH_{11} \rightarrow EH_{11}$ fifth-harmonic generation. For higher pressures, pronounced oscillations in harmonic power are evident when the accumulated phase mismatch $\Delta\phi^{(5)}_{1,1}(z)$ of the harmonic $E_{5,1}$ increases above the phase matching pressure (orange line in Fig. A.5 (a)). In a Gaussian laser pulse the intensity is a function of time t, so these oscillations average out due to the intensity dependent phase matching pressure. The finite spectral distribution of a laser pulse leads to further smoothing of the oscillations due to the wavelength dependence of the phase matching pressure.

When the pump laser of the same power is perfectly coupled to the EH_{12} mode, phase matching occurs at much higher pressures because of the stronger waveguide dispersion at the fundamental frequency ω_1 to be compensated by the negative gas dispersion. The different shape of the generated fifth harmonic polarization $\overline{\overline{P}}^{NL}_5(r) \propto J_0\left(u_{12}\frac{r}{a}\right)^5$ (compare Fig 5 (a) red line) now distributes gain to all higher modes (compare Fig. A.4). The power generated within each individual mode is then approximately proportional to $(\overline{P}^{NL}_{5,m})^2$ (as shown in relative scale in Fig. A.4 at the right end of the graph) and the squared phase matching pressure p^2_{PM} of each individual mode of the harmonic m (compare the maxima of the colored lines in Fig. A.5 (b)). Because of the approximately five times bigger phase matching pressures, the harmonic yield in this coupling case can be about $5^2 = 25$ times larger than for coupling to the lowest waveguide mode, as long as the waveguide is much shorter than the damping length of the EH_{12} mode at the fundamental wavelength (compare 5.4). The additional factor of foru missing to explain the approximately 100 times bigger yield shown in Fig. A.5 (b) arises from the 1.5 times higher peak intensity of the EH_{12} mode at constant input power, enhancing the nonlinear polarization.

A.3.4 Pulse propagation effects

In frequency conversion of ultra-short pulses, also the temporal pulse shape is important. In our case temporal "walk-off" $\Delta\tau^{(j)}_G = L(v_g(\omega_j) - v_g(\omega))$ between the harmonic j and the fundamental pulse is the dominating pulse propagation effect. It is proportional to the interaction length L and the dispersion of γ. For picosecond pulses, the dispersion of a bare waveguide with $a = 50\,\mu\mathrm{m}$ is negligible for L <1 m, however in the present case, when the fundamental is tuned very close to the five-photon resonance, the refractive index of the gas exhibits a strong dispersion at the fifth harmonic (compare Fig. 1.1). As a result, the harmonic pulse is prolonged by about $|\tau^{(5)}_g|$. The group delay is strongly intensity dependent due to the Stark shift of the excited state and therefore changes in radial as well as temporal dimension of the Gaussian laser pulse, having the maximal value at the peak intensity, when the five-photon detuning to the 4s level minimal. Only a more advanced model (e.g. [78]) could account for this, but would require very much longer calculation time. In our simpler model we monitor the maximal (worst

case) group delay. For our investigations at 512 nm fundamental wavelength, we estimate a maximal group delay of 0.21 ps at the largest argon pressure used in our measurements. This is much less than half the pump pulse length and therefore imposes no severe limit on the numerical results. Pulse propagation due to self-phase modulation is neglected, as the nonlinear refractive index at an intensity of 7 TW/cm^2 and the maximum considered pressure of 60 mbar in our experiments at 512 nm fundamental wavelength yield a phase shift below 0.02 rad only, which does not alter the pulse envelope. Also the waveguide modal dispersion produces a negligible group delay around 0.04 ps only (compared to $\tau_p > 1$ ps).

A.3.5 Rarefied gas flow in a microchannel

For precise control of this phase matching condition, we require the dependence of the gas pressure between the two supply holes on the (experimentally accessible) pressure applied to the chamber. We develop model of the particle density of the gas atoms, to determine the mismatch in propagation constants $\Delta\gamma_{j,m'}(z)$.

Inside the waveguide the mean free path of an atom at atmospheric pressure is already only 100 times smaller than the capillary radius. The fraction of wall collisions per molecular collision approaches unity between 1 and 10 mbar static pressure. Therefore the flow inside our waveguide must be modeled by the Burnett equation instead of continuum flow equations below 100 mbar [111]. With an experimentally determined hole radius of $r_H = 33(3)\,\mu$m and a radius of $a = 52(2)\,\mu$m deduced from microscope images, the gas flow from the inlet inside of the chamber at a static pressure p_c towards the outlet inside the vacuum setup ($p_v < 0.1$ mbar) is modeled. We use the model of rarefied flow inside a microtube, valid for pressures from vacuum up to atmospheric pressure [112].

The computation starts at the input of the supply hole inside the chamber at static pressure p_c. The boundary conditions for the gas flow inside the channel are $p_i + q_i = p_c$ with the dynamic pressure $q = p\,u^2(2R_sT)^{-1}$ of the gas atoms traveling at a mean streamwise velocity u. Here R_s is the specific gas constant of Argon. We assume the flow and expansion to be isotherm with T = 25 °C due to the above mentioned dominance of wall collisions. At the output inside the vacuum setup we determine a static background pressure p_v. For the boundary at the microtube output, we thus set the condition $p_o + q_o = p_v$. The capillary is treated as micro channel with sudden expansion, so at the intersection between the bore and the supply hole the static pressure p_b is constant and only the velocity u changes between the two tube sections [113]. By the continuity equation we can then numerically determine a mass flow rate that is invariant along the streamwise coordinate and fulfills the boundary conditions. The pressure at each position inside the channel is then calculated in the segmented pipe model [112].

We assume the capillary bore section (i.e. the phase matching region) between the supply holes to have the same static pressure p_b as the junction point between supply hole and outward facing bore. Fig. A.6 shows the computed static pressure $p_b(p_c, z)$ along the propagation direction. Due to the transition through different flow regimes from 1 to 60 mbar, the the ratio $b = p_b/p_c$ between (mea-

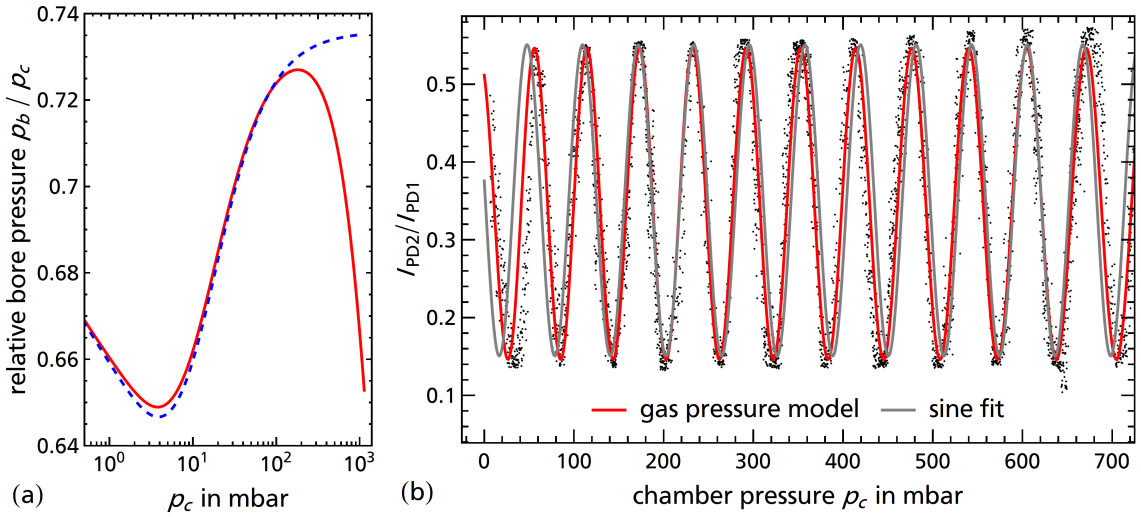

Figure A.6: (a) Calculated dependence of the waveguide bore pressure p_b vs. the chamber pressure p_c including (red line) and neglecting (blue dashed line) the dynamic pressure inside the channels. (b) Measured (black dots) interference signal caused by the pressure dependent phase change inside the waveguide, compared with a sinusoidal fit (gray) and the calculation from the spatial pressure model (red line).

sured) chamber pressure p_c and actual phase matching pressure p_b rises from 0.65 at $p_c = 1$ mbar to 0.73 at $p_c = 60$ mbar (compare Fig. A.6 (a)). The decrease in relative bore pressure near $p_c \approx 100$ mbar originates from the dynamic pressure drop at high flow velocity inside the supply channel and vanishes, when dynamic pressures are neglected (blue dashed line). We check our model by an interference measurement[12] of the phase shift inside the waveguide with increasing argon pressure p_c inside the chamber. Each of the interference fringes in Fig. A.6 (b) represents a change in arm length l of

$$\Delta l(p_c) = \int_0^L (n_{Ar}(T, \lambda_{cw}, p_b(p_c, z)) - 1)\, dz = \lambda_{cw} = 532.1(1)\text{nm}. \tag{A.4}$$

Compared to the assumption of a constant factor b as depicted by a simple sinusoidal fit (gray line in Fig. A.6 (b)), the interferogram exhibits a periodicity that is first decreasing until $p_c \approx 100$ mbar. This is caused by the increase in b and the change of the slopes towards vacuum from concave to convex shape, increasing the effective, gas-filled length. The increase in periodicity above 600 mbar finally is due to the dynamic pressure at the input. All features are well resolved by the interferogram signal calculated from the path difference $\Delta l(p_c)$ of equation A.4 for a waveguide of a =52 μm and r_H =30.1(3) μm. The model is sensitive on the fraction r_H/a, so the value of the hole radius was optimized within the error margins of the microscope measurement.[13].

[12]The experimental data was acquired by Mario Hilbig [M6].

[13]We note that intersection between the supply holes and the capillary bore represents a 90° bend in the gas flow. The increased pressure drop on (fixed bore) bends might increase the static pressure at the intersection by up to 15 %. [114] So dispute the good agreement, the local pressure might be only correct within about 15 % relative deviation.

Bibliography

[1] Technical Committee ISO/TC 20. *ISO 21348:2007(E) - Space enviroment (natural and artificial) - Process for determining solar irradiances.* ISO copyright office, Geneva, first edit edition (2007). URL https://iso.org/standard/39911.html

[2] P. Rupper. *Erzeugung von schmalbandiger Laserstrahlung bis 20 eV und Anwendungen in der Photoelektronenspektroskopie*. Ph.D. thesis, ETH Zürich (2005). URL https://doi.org/10.3929/ethz-a-004904642

[3] J. L. Ellis, D. D. Hickstein, W. Xiong, F. Dollar, B. B. Palm, K. E. Keister, K. M. Dorney, C. Ding, T. Fan, M. B. Wilker, K. J. Schnitzenbaumer, G. Dukovic, J. L. Jimenez, H. C. Kapteyn, and M. M. Murnane. *Materials Properties and Solvated Electron Dynamics of Isolated Nanoparticles and Nanodroplets Probed with Ultrafast Extreme Ultraviolet Beams*. The Journal of Physical Chemistry Letters **7**(4) 609 (2016). URL https://doi.org/10.1021/acs.jpclett.5b02772

[4] B. Winter, R. Weber, I. V. Hertel, M. Faubel, P. Jungwirth, E. C. Brown, and S. E. Bradforth. *Electron Binding Energies of Aqueous Alkali and Halide Ions: EUV Photoelectron Spectroscopy of Liquid Solutions and Combined Ab Initio and Molecular Dynamics Calculations*. Journal of the American Chemical Society **127**(19) 7203 (2005). URL https://doi.org/10.1021/ja042908l

[5] F. Krausz and M. I. Stockman. *Attosecond metrology: from electron capture to future signal processing*. Nature Photonics **8**(3) 205 (2014). URL https://doi.org/10.1038/nphoton.2014.28

[6] C. Wagner and N. Harned. *Lithography gets extreme*. Nature Photonics **4**(1) 24 (2010). URL https://doi.org/10.1038/nphoton.2009.251

[7] T. Harada, M. Nakasuji, Y. Nagata, T. Watanabe, and H. Kinoshita. *Phase Imaging of Extreme-Ultraviolet Mask Using Coherent Extreme-Ultraviolet Scatterometry Microscope*. Japanese Journal of Applied Physics **52**(6S) 06GB02 (2013). URL https://doi.org/10.7567/JJAP.52.06GB02

[8] M. D. Seaberg, B. Zhang, D. F. Gardner, E. R. Shanblatt, M. M. Murnane, H. C. Kapteyn, and D. E. Adams. *Tabletop nanometer extreme ultraviolet imaging in an extended reflection mode using coherent Fresnel ptychography*. Optica **1**(1) 39 (2014). URL http://arxiv.org/abs/1312.2049

[9] T. Mey. *Radiation characteristics of extreme UV and soft X-ray sources*, volume 15 of *Göttingen Series in X-ray Physics*. Göttingen University Press, Göttingen (2015). URL https://doi.org/10.17875/gup2015-817

[10] T. Nakazato, I. Ito, Y. Kobayashi, X. Wang, C. Chen, and S. Watanabe. *149.8 nm, the shortest wavelength generated by phase matching in nonlinear crystals*. In K. L. Vodopyanov and K. L. Schepler, eds., *Nonlinear Frequency Generation and Conversion: Materials and Devices XVI*, 1008804 (2017). URL https://doi.org/10.1117/12.2249976

[11] P. Trabs, F. Noack, A. S. Aleksandrovsky, A. I. Zaitsev, and V. Petrov. *Generation of coherent radiation in the vacuum ultraviolet using randomly quasi-phase-matched strontium tetraborate*. Optics Letters **41**(3) 618 (2016). URL https://doi.org/10.1364/OL.41.000618

[12] B. Dromey, M. Zepf, A. Gopal, K. Lancaster, M. S. Wei, K. Krushelnick, M. Tatarakis, N. Vakakis, S. Moustaizis, R. Kodama, M. Tampo, C. Stoeckl, R. Clarke, H. Habara, D. Neely, S. Karsch, and P. Norreys. *High harmonic generation in the relativistic limit*. Nature Physics **2**(7) 456 (2006). URL https://doi.org/10.1038/nphys338

[13] R. A. Ganeev. *High-order harmonic generation in a laser plasma: a review of recent achievements*. Journal of Physics B: Atomic, Molecular and Optical Physics **40**(22) R213 (2007). URL https://doi.org/10.1088/0953-4075/40/22/R01

[14] A. L. Huillier and P. Balcou. *High-order harmonic generation in rare gases with a 1-ps 1053-nm laser*. Physical Review Letters **70**(6) 774 (1993). URL https://doi.org/10.1103/PhysRevLett.70.774

[15] R. Hilbig, G. Hilber, A. Lago, B. Wolff, and R. Wallenstein. *Tunable Coherent VUV Radiation Generated by Nonlinear Optical Frequency Conversion in Gases*. volume 613, 48 (1986). URL https://doi.org/10.1117/12.960383

[16] P. Rupper and F. Merkt. *Intense narrow-bandwidth extreme ultraviolet laser system tunable up to 20 eV*. Review of Scientific Instruments **75**(3) 613 (2004). URL https://doi.org/10.1063/1.1646744

[17] L. V. Keldysh. *Ionization in the field of a strong electromagnetic wave*. Soviet Physics JETP **20**(5) 1307 (1964)

[18] E. Mevel, P. Breger, R. Trainham, G. Petite, P. Agostini, A. Migus, J.-P. Chambaret, and A. Antonetti. *Atoms in strong optical fields: Evolution from multiphoton to tunnel ionization*. Physical Review Letters **70**(4) 406 (1993). URL https://doi.org/10.1103/PhysRevLett.70.406

[19] R. Taïeb, V. Véniard, J. Wassaf, and A. Maquet. *Roles of resonances and recollisions in strong-field atomic phenomena. II. High-order harmonic generation*. Physical Review A **68**(3) 033403 (2003). URL http://link.aps.org/doi/10.1103/PhysRevA.68.033403

[20] M. B. Gaarde and K. J. Schafer. *Enhancement of many high-order harmonics via a single multiphoton resonance*. Physical Review A **64**(1) 013820 (2001). URL https://doi.org/10.1103/PhysRevA.64.013820

[21] S. Camp, K. J. Schafer, and M. B. Gaarde. *Interplay between resonant enhancement and quantum path dynamics in harmonic generation in helium*. Physical Review A **92**(1) 013404 (2015). URL https://link.aps.org/doi/10.1103/PhysRevA.92.013404

[22] L. Plaja and L. Roso. *High-order Harmonic Generation in a Two-level Atom*. Journal of Modern Optics **40**(5) 793 (1993). URL https://doi.org/10.1080/09500349314550831

[23] A. L'Huillier, P. Balcou, and L. A. Lompré. *Coherence and resonance effects in high-order harmonic generation*. Physical Review Letters **68**(2) 166 (1992). URL https://doi.org/10.1103/PhysRevLett.68.166

[24] E. S. Toma, P. Antoine, a. D. Bohan, and H. G. Muller. *Resonance-enhanced high-harmonic generation*. Journal of Physics B: Atomic, Molecular and Optical Physics **32**(24) 5843 (1999). URL https://doi.org/10.1088/0953-4075/32/24/318

[25] M. Barkauskas, F. Brandi, F. Giammanco, D. Neshev, a. Pirri, and W. Ubachs. *A novel-type tunable and narrowband extreme ultraviolet radiation source based on high-harmonic conversion of picosecond laser pulses*. Journal of Electron Spectroscopy and Related Phenomena **144-147** 1151 (2005). URL http://linkinghub.elsevier.com/retrieve/pii/S036820480500277X

[26] R. A. Ganeev. *Generation of high-order harmonics of high-power lasers in plasmas produced under irradiation of solid target surfaces by a prepulse*. Physics-Uspekhi **52**(1) 55 (2009). URL http://stacks.iop.org/1063-7869/52/i=1/a=A03?key=crossref.339a68b9f95e635aba0282de0a774d99

[27] M. Shapiro and P. Brumer. *Quantum Control of Molecular Processes*. Wiley-VCH Verlag GmbH Co. KGaA, Weinheim, Germany (2012). URL https://doi.org/10.1002/9783527639700

[28] N. E. Karapanagioti, D. Xenakis, D. Charalambidis, and C. Fotakis. *Coherent control in four-photon excitation schemes*. Journal of Physics B: Atomic, Molecular and Optical Physics **29**(16) 3599 (1996). URL https://doi.org/10.1088/0953-4075/29/16/009

[29] D. Xenakis, N. E. Karapanagioti, C. Fotakis, and D. Charalambidis. *Control of third harmonic generation through the phase of an additional third harmonic field*. Optics Communications **152**(1-3) 83 (1998). URL https://doi.org/10.1016/S0030-4018(98)00135-7

[30] H. Münch, S. Chakrabarti, and T. Halfmann. *Coherent control of frequency conversion toward short (picosecond) vacuum-ultraviolet radiation pulses*. Physical Review A **82**(3) 033821 (2010). URL https://doi.org/10.1103/PhysRevA.82.033821

[31] C. G. Durfee, A. R. Rundquist, S. Backus, C. Herne, M. M. Murnane, and H. C. Kapteyn. *Phase Matching of High-Order Harmonics in Hollow Waveguides*. Physical Review Letters **83**(11) 2187 (1999). URL https://doi.org/10.1103/PhysRevLett.83.2187

[32] A. Rundquist. *Phase-Matched Generation of Coherent Soft X-rays*. Science **280**(5368) 1412 (1998). URL https://doi.org/10.1126/science.280.5368.1412

[33] P. S. J. Russell, P. Hölzer, W. Chang, A. Abdolvand, and J. C. Travers. *Hollow-core photonic crystal fibres for gas-based nonlinear optics*. Nature Photonics **8**(4) 278 (2014). URL http://www.nature.com/doifinder/10.1038/nphoton.2013.312

[34] R. W. Boyd. *Wave-Equation Description of Nonlinear Optical Interactions*. In *Nonlinear Optics*, 69–133. Academic Press (2008). URL https://doi.org/10.1016/B978-0-12-369470-6.00002-2

[35] R. Gans. *Fortpflanzung des Lichts durch ein inhomogenes Medium*. Annalen der Physik **352**(14) 709 (1915). URL http://doi.wiley.com/10.1002/andp.19153521402

[36] A. Spott, A. Becker, and A. Jaroń-Becker. *Transition from perturbative to nonperturbative interaction in low-order-harmonic generation*. Physical Review A **91**(2) 023402 (2015). URL https://link.aps.org/doi/10.1103/PhysRevA.91.023402

[37] R. W. Boyd. *Quantum-Mechanical Theory of the Nonlinear Optical Susceptibility*. In *Nonlinear Optics*, 135–206. Academic Press (2008). URL https://doi.org/10.1016/B978-0-12-369470-6.00003-4

[38] G. Copley and D. Camm. *Pressure broadening and shift of argon emission lines*. Journal of Quantitative Spectroscopy and Radiative Transfer **14**(9) 899 (1974). URL https://doi.org/10.1016/0022-4073(74)90017-X

[39] W. F. Chan, G. Cooper, X. Guo, G. R. Burton, and C. E. Brion. *Absolute optical oscillator strengths for the electronic excitation of atoms at high resolution. III. The photoabsorption of argon, krypton, and xenon*. Physical Review A

46(1) 149 (1992). URL https://link.aps.org/doi/10.1103/PhysRevA.46.149

[40] W. F. Chan, G. Cooper, X. Guo, G. R. Burton, and C. E. Brion. *Erratum : Absolute optical oscillator strengths for the electronic excitation of atoms* **48**(1) 858 (1993)

[41] A. Kramida, Y. Ralchenko, J. Reader, and N. A. Team. *NIST Atomic Spectra Database (version 5.5.6)* (2016). URL http://physics.nist.gov/asd

[42] S. Zahedpour, J. K. Wahlstrand, and H. M. Milchberg. *Measurement of the nonlinear refractive index of air constituents at mid-infrared wavelengths*. Optics Letters **40**(24) 5794 (2015). URL https://doi.org/10.1364/OL.40.005794

[43] D. Milam. *Review and assessment of measured values of the nonlinear refractive-index coefficient of fused silica*. Applied Optics **37**(3) 546 (1998). URL https://www.osapublishing.org/abstract.cfm?URI=ao-37-3-546

[44] E. Constant, D. Garzella, P. Breger, E. Mével, C. Dorrer, C. Le Blanc, F. Salin, and P. Agostini. *Optimizing High Harmonic Generation in Absorbing Gases: Model and Experiment*. Physical Review Letters **82**(8) 1668 (1999). URL http://link.aps.org/doi/10.1103/PhysRevLett.82.1668

[45] H. Friedrich. *Theoretical Atomic Physics*. Springer-Verlag, Berlin/Heidelberg (2006). URL http://link.springer.com/10.1007/3-540-29278-0

[46] C. J. Joachain, N. J. Kylstra, and R. M. Potvliege. *Atoms in Intense Laser Fields*. Cambridge University Press, Cambridge (2011). URL http://ebooks.cambridge.org/ref/id/CBO9780511993459

[47] M. H. Mittleman. *Introduction to the Theory of Laser-Atom Interactions*. Springer US, Boston, MA (1993). URL http://link.springer.com/10.1007/978-1-4899-2436-0

[48] L. Pan, J. H. Eberly, and L. Armstrong. *Comments on the effect of the ponderomotive potential in the above-threshold ionization processes*. Journal of the Optical Society of America B **3**(10) 1319 (1986). URL https://www.osapublishing.org/abstract.cfm?URI=josab-3-10-1319

[49] R. M. Potvliege and S. Vučić. *High-order above-threshold ionization of argon: Plateau resonances and the Floquet quasienergy spectrum*. Physical Review A **74**(2) 023412 (2006). URL https://link.aps.org/doi/10.1103/PhysRevA.74.023412

[50] E. Mede and R. M. Potvliege. *The quasienergy spectrum of argon from 400 to 800 nm*. Laser Physics Letters **4**(5) 357 (2007). URL https://doi.org/10.1002/lapl.200610130

[51] P. Ackermann, H. Münch, and T. Halfmann. *Resonantly-enhanced harmonic generation in Argon*. Optics Express **20**(13) 13824 (2012). URL https://doi.org/10.1364/OE.20.013824

[52] P. Ackermann. *Erzeugung Hoher Harmonischer mit Laserpulsen im grünen Spektralbereich*. Masters' thesis, Technische Universität Darmstadt (2011)

[53] R. Trebino. *Frequency-Resolved Optical Gating: The Measurement of Ultrashort Laser Pulses*. Springer US (2012). URL https://books.google.de/books?id=257aBwAAQBAJ

[54] R. A. Ganeev. *High-Order Harmonic Studies of the Role of Resonances on the Temporal and Efficiency Characteristics of Converted Coherent Pulses: Different Approaches*. In *Resonance Enhancement in Laser-Produced Plasmas*, chapter 1, 1–15. John Wiley Sons, Inc., Hoboken, NJ, USA (2018). URL https://doi.org/10.1002/9781119472346.ch1

[55] F. Ehlotzky. *Atomic phenomena in bichromatic laser fields*. Physics Reports **345**(4) 175 (2001). URL http://www.sciencedirect.com/science/article/pii/S0370157300001009

[56] P. Brumer and M. Shapiro. *Control of unimolecular reactions using coherent light*. Chemical Physics Letters **126**(6) 541 (1986). URL http://linkinghub.elsevier.com/retrieve/pii/S0009261486801713

[57] M. Förster, T. Paschen, M. Krüger, C. Lemell, G. Wachter, F. Libisch, T. Madlener, J. Burgdörfer, and P. Hommelhoff. *Two-Color Coherent Control of Femtosecond Above-Threshold Photoemission from a Tungsten Nanotip*. Physical Review Letters **117**(21) 217601 (2016). URL https://doi.org/10.1103/PhysRevLett.117.217601

[58] T. Paschen, M. Förster, M. Krüger, C. Lemell, G. Wachter, F. Libisch, T. Madlener, J. Burgdörfer, and P. Hommelhoff. *High visibility in two-color above-threshold photoemission from tungsten nanotips in a coherent control scheme*. Journal of Modern Optics **64**(10-11) 1054 (2017). URL https://www.tandfonline.com/doi/full/10.1080/09500340.2017.1281453

[59] C. Kealhofer. *An Ultrafast Switch for Electron Emission*. Physics **9**(November) 132 (2016). URL https:/doi.org/10.1103/Physics.9.132

[60] P. Ackermann, A. Scharf, and T. Halfmann. *Strong quantum interferences in frequency up-conversion towards short vacuum-ultraviolet radiation pulses*. Physical Review A **89**(6) (2014). URL https://doi.org/10.1103/PhysRevA.89.063804

[61] M. Aymar and M. Coulombe. *Theoretical transition probabilities and lifetimes in Kr I and Xe I spectra*. Atomic Data and Nuclear Data Tables **21**(6) 537 (1978). URL http://linkinghub.elsevier.com/retrieve/pii/0092640X78900074

[62] C. J. Humphreys and E. Paul. *Interferometric Wavelength Determinations in the First Spectrum of ' 36 Xe*. J. Opt. Soc. Am. **60**(10) 1302 (1970)

[63] S. Chakrabarti, H. Muench, and T. Halfmann. *Adiabatically driven frequency conversion towards short extreme-ultraviolet radiation pulses*. Physical Review A **82**(6) 063817 (2010). URL https://link.aps.org/doi/10.1103/PhysRevA.82.063817

[64] T. Halfmann, T. Rickes, N. Vitanov, and K. Bergmann. *Lineshapes in coherent two-photon excitation*. Optics Communications **220**(4-6) 353 (2003). URL http://linkinghub.elsevier.com/retrieve/pii/S0030401803013683

[65] N. Vitanov, B. Shore, L. Yatsenko, K. Böhmer, T. Halfmann, T. Rickes, and K. Bergmann. *Power broadening revisited: theory and experiment*. Optics Communications **199**(1-4) 117 (2001). URL http://linkinghub.elsevier.com/retrieve/pii/S003040180101495X

[66] E. Papastathopoulos, D. Xenakis, and D. Charalambidis. *Phase-sensitive ionization through multiphoton-excitation schemes involving even numbers of photons*. Physical Review A **59**(6) 4840 (1999). URL http://link.aps.org/doi/10.1103/PhysRevA.59.4840

[67] M. Gunawardena and D. Elliott. *Weak signal detection using coherent control*. Physical Review A **76**(3) 033412 (2007). URL http://link.aps.org/doi/10.1103/PhysRevA.76.033412

[68] T. Adachi, K. Kondo, and S. Watanabe. *Gas density measurement of pulsed gas jets using XeF four-photon fluorescence induced by a KrF laser*. Applied Physics B Photophysics and Laser Chemistry **55**(4) 323 (1992). URL http://link.springer.com/10.1007/BF00333074

[69] T. Namioka. *Theory of the Concave Grating III Seya-Namioka Monochromator*. Journal of the Optical Society of America **49**(10) 951 (1959). URL https://www.osapublishing.org/abstract.cfm?URI=josa-49-10-951

[70] P. E. Ciddor. *Refractive index of air: new equations for the visible and near infrared*. Applied Optics **35**(9) 1566 (1996). URL https://www.osapublishing.org/abstract.cfm?URI=ao-35-9-1566

[71] P. A. Bromiley. *Products and Convolutions of Gaussian Distributions*. Technical report, Imaging Science and Biomedical Engineering Division, Medical School, University of Manchester, Manchester (2003). URL http://tina.wiau.man.ac.uk/docs/memos/2003-003.pdf

[72] E. A. J. Marcatili and R. A. Schmeltzer. *Hollow Metallic and Dielectric Waveguides for Long Distance Optical Transmission and Lasers*. Bell System Technical Journal **43**(4) 1783 (1964). URL http://ieeexplore.ieee.org/lpdocs/epic03/wrapper.htm?arnumber=6773550

[73] C. G. Durfee, S. Backus, M. M. Murnane, and H. C. Kapteyn. *Ultrabroadband phase-matched optical parametric generation in the ultraviolet by use of guided waves*. Optics Letters **22**(20) 1565 (1997). URL https://doi.org/10.1364/OL.22.001565

[74] L. Misoguti, S. Backus, C. G. Durfee, R. Bartels, M. M. Murnane, and H. C. Kapteyn. *Generation of Broadband VUV Light Using Third-Order Cascaded Processes*. Physical Review Letters **87**(1) 013601 (2001). URL https://link.aps.org/doi/10.1103/PhysRevLett.87.013601

[75] R. Friedberg, S. R. Hartmann, and J. T. Manassah. *Optimizing third harmonic generation in gases*. Journal of Physics B: Atomic, Molecular and Optical Physics **24**(12) 2883 (1991). URL https://doi.org/10.1088/0953-4075/24/12/011

[76] P. Ackermann, X. Laforgue, M. Hilbig, M. Schilder, and T. Halfmann. *Phase-matched harmonic generation in gas-filled waveguides in the vicinity of a multiphoton resonance*. Journal of the Optical Society of America B **35**(2) 468 (2018). URL https://www.osapublishing.org/abstract.cfm?URI=josab-35-2-468

[77] R. K. Nubling. *Launch conditions and mode coupling in hollow-glass waveguides*. Optical Engineering **37**(9) 2454 (1998). URL http://opticalengineering.spiedigitallibrary.org/article.aspx?doi=10.1117/1.601768

[78] F. Tani, J. C. Travers, and P. St.J. Russell. *Multimode ultrafast nonlinear optics in optical waveguides: numerical modeling and experiments in kagomé photonic-crystal fiber*. Journal of the Optical Society of America B **31**(2) 311 (2014). URL https://doi.org/10.1364/JOSAB.31.000311

[79] A. W. Snyder and J. D. Love. *Illumination, tilts and offsets*. In *Optical Waveguide Theory*, chapter 20, 420–441. Springer US, Boston, MA (1984). URL http://link.springer.com/10.1007/978-1-4613-2813-1

[80] A. Bideau-Mehu, Y. Guern, R. Abjean, and A. Johannin-Gilles. *Measurement of refractive indices of neon, argon, krypton and xenon in the 253.7–140.4 nm wavelength range. Dispersion relations and estimated oscillator strengths of the resonance lines*. Journal of Quantitative Spectroscopy and Radiative Transfer **25**(5) 395 (1981). URL http://linkinghub.elsevier.com/retrieve/pii/0022407381900571

[81] P. Gill and D. W. O. Heddle. *Determination of the Refractive Indices of Gases in the Vacuum Ultraviolet II The Rayleigh Scattering Method*. Journal of the Optical Society of America **53**(7) 847 (1963). URL https://www.osapublishing.org/abstract.cfm?URI=josa-53-7-847

[82] T. Larsen. *Beitrag zur Dispersion der Edelgase*. Zeitschrift für Physik **88**(5-6) 389 (1934). URL http://link.springer.com/10.1007/BF01343498

[83] Y. Clergent, C. Durou, and M. Laurens. *Refractive Index Variations for Argon, Nitrogen, and Carbon Dioxide at λ = 632.8 nm (HeNe Laser Light) in the Range 288.15 K < T < 323.15 K, 0 < p < 110 kPa*. Journal of Chemical Engineering Data **44**(2) 197 (1999). URL http://pubs.acs.org/doi/abs/10.1021/je980133o

[84] J. Zhang, Z. H. Lu, and L. J. Wang. *Precision refractive index measurements of air, N2, O2, Ar, and CO2 with a frequency comb*. Applied Optics **47**(17) 3143 (2008). URL https://doi.org/10.1364/AO.47.003143

[85] S. L. Wu, Z. P. Zhong, R. F. Feng, S. L. Xing, B. X. Yang, and K. Z. Xu. *Electron-impact study in valence and autoionization resonance regions of argon*. Physical Review A **51**(6) 4494 (1995). URL https://doi.org/10.1103/PhysRevA.51.4494

[86] A. L. Lytle. *Phase Matching and Coherence of High-Order Harmonic Generation in Hollow Waveguides*. Phd thesis, University of Colorado (2008)

[87] M. Hermans. *Selective, Laser-Induced Etching of Fused Silica at High Scan-Speeds Using KOH*. Journal of Laser Micro/Nanoengineering **9**(2) 126 (2014). URL https://doi.org/10.2961/jlmn.2014.02.0009

[88] B. Dromey, M. Zepf, M. Landreman, and S. M. Hooker. *Quasi-phasematching of harmonic generation via multimode beating in waveguides.* Optics Express **15**(13) 7894 (2007)

[89] H. Ren, A. Nazarkin, J. Nold, and P. S. Russell. *Quasi-phase-matched high harmonic generation in hollow core photonic crystal fibers*. Optics Express **16**(21) 17052 (2008). URL https://doi.org/10.1364/OE.16.017052

[90] T. Diskin, O. Kfir, A. Fleischer, and O. Cohen. *Phase modulation in polarization beating quasi-phase-matching of high-order-harmonic generation*. Physical Review A **92**(3) 033807 (2015). URL https://doi.org/10.1103/PhysRevA.92.033807

[91] L. Z. Liu, K. O'Keeffe, and S. M. Hooker. *Quasi-phase-matching of high-order-harmonic generation using multimode polarization beating*. Physical Review A **87**(2) 023810 (2013). URL https://doi.org/10.1103/PhysRevA.87.023810

[92] C. G. Durfee, L. Misoguti, S. Backus, H. C. Kapteyn, and M. M. Murnane. *Phase matching in cascaded third-order processes*. Journal of the Optical Society of America B **19**(4) 822 (2002). URL https://doi.org/10.1364/JOSAB.19.000822

[93] A. M. Weiner. *Femtosecond pulse shaping using spatial light modulators*. Review of Scientific Instruments **71**(5) 1929 (2000). URL http://aip.scitation.org/doi/10.1063/1.1150614

[94] X. Yuan, P. Wei, C. Liu, Z. Zeng, Y. Zheng, J. Jiang, X. Ge, and R. Li. *Enhanced high-order harmonic generation from excited argon*. Applied Physics Letters **107**(4) 041110 (2015). URL http://aip.scitation.org/doi/10.1063/1.4927662

[95] I. Rau, F. Kajzar, J. Luc, B. Sahraoui, and G. Boudebs. *Comparison of Z-scan and THG derived nonlinear index of refraction in selected organic solvents*. Journal of the Optical Society of America B **25**(10) 1738 (2008)

[96] W. T. Lotshaw, D. McMorrow, C. Kalpouzos, and G. A. Kenney-Wallace. *Femtosecond dynamics of the optical kerr effect in liquid nitrobenzene and chlorobenzene*. Chemical Physics Letters **136**(3-4) 323 (1987)

[97] HORIBA Scientific. *H20-UVL Brochure*. online, accessed: 2018-11-25. URL http://www.horiba.com/fileadmin/uploads/Scientific/Documents/VUV_Spectroscopy/Brochure_H20-UVL_LR2.pdf

[98] W. R. Hunter, J. F. Osantowski, and G. Hass. *Reflectance of Aluminum Overcoated with MgF and LiF in the Wavelength Region from 1600 Å to 300 Å at Various Angles of Incidence*. Applied Optics **10**(3) 540 (1971). URL http://www.ncbi.nlm.nih.gov/pubmed/20094487

[99] R. J. Carman, D. J. Little, and D. M. Kane. *Optical emission spectroscopy system operating in the vacuum-ultraviolet spectral range $\lambda < 100$ nm - a semi-empirical determination of sensitivity*. Measurement Science and Technology **26**(8) 085203 (2015). URL https.//doi.org/10.1088/0957-0233/26/8/085203

[100] A. M. Tyutikov. *ELECTRON MULTIPLIERS OF THE OPEN TYPE*. Sov. Phys. Usp. **13**(2) 204 (1970)

[101] Hamamatsu Photonics. *PHOTOMULTIPLIER TUBES Basics and Applications THIRD EDITION (Edition 3a)*. Hamamatsu Photonics K.K., Electron Tube Division, 3a edition (2007). URL https://www.hamamatsu.com/resources/pdf/etd/PMT_handbook_v3aE.pdf

[102] Hamamatsu Photonics. *ELECTRON MULTIPLIERS*. online, accessed: 2018-11-07. URL https://www.hamamatsu.com/resources/pdf/etd/EMT_TPMH1354E.pdf

[103] W. Ettoumi, Y. Petit, J. Kasparian, and J.-P. Wolf. *Generalized Miller Formula*. Optics Express **18**(7) 6613 (2010). URL https://doi.org/10.1364/OE.18.006613

[104] M. Tarazkar, D. A. Romanov, and R. J. Levis. *Higher-order nonlinearity of refractive index: The case of argon*. The Journal of Chemical Physics **140**(21) 214316 (2014). URL http://aip.scitation.org/doi/10.1063/1.4880716

[105] V. Loriot, E. Hertz, O. Faucher, and B. Lavorel. *Measurement of high order Kerr refractive index of major air components*. Optics Express **17**(16) 13429 (2009). URL https://doi.org/10.1364/OE.17.013429

[106] V. Loriot, E. Hertz, O. Faucher, and B. Lavorel. *Measurement of high order Kerr refractive index of major air components: erratum*. Optics Express **18**(3) 3011 (2010). URL https://doi.org/10.1364/OE.18.003011

[107] J. K. Wahlstrand, Y.-H. Cheng, and H. M. Milchberg. *High Field Optical Nonlinearity and the Kramers-Kronig Relations*. Physical Review Letters **109**(11) 113904 (2012). URL https://doi.org/10.1103/PhysRevLett.109.113904

[108] D. L. Weerawarne, X. Gao, A. L. Gaeta, and B. Shim. *Higher-Order Nonlinearities Revisited and Their Effect on Harmonic Generation*. Physical Review Letters **114**(9) 093901 (2015). URL https://link.aps.org/doi/10.1103/PhysRevLett.114.093901

[109] P. Béjot, J. Kasparian, S. Henin, V. Loriot, T. Vieillard, E. Hertz, O. Faucher, B. Lavorel, and J.-P. Wolf. *Higher-Order Kerr Terms Allow Ionization-Free Filamentation in Gases*. Physical Review Letters **104**(10) 103903 (2010). URL https://link.aps.org/doi/10.1103/PhysRevLett.104.103903

[110] D. Wang, Y. Leng, and Z. Xu. *Measurement of nonlinear refractive index coefficient of inert gases with hollow-core fiber*. Applied Physics B **111**(3) 447 (2013). URL http://link.springer.com/10.1007/s00340-013-5354-0

[111] A. Agrawal. *A Comprehensive Review on Gas Flow in Microchannels*. International Journal of Micro-Nano Scale Transport **2**(1) 1 (2011). URL http://multi-science.atypon.com/doi/10.1260/1759-3093.2.1.1

[112] Z. Yang and S. V. Garimella. *Rarefied gas flow in microtubes at different inlet-outlet pressure ratios*. Physics of Fluids **21**(5) 052005 (2009). URL http://aip.scitation.org/doi/10.1063/1.3139310

[113] V. Varade, A. Agrawal, and A. M. Pradeep. *Experimental study of rarefied gas flow near sudden contraction junction of a tube*. Physics of Fluids **26**(6) 062002 (2014). URL http://aip.scitation.org/doi/10.1063/1.4881940

[114] V. Varade, A. Agrawal, S. Prabhu, and A. Pradeep. *Early onset of flow separation with rarefied gas flowing in a 90° bend tube*. Experimental Thermal and Fluid Science **66** 221 (2015). URL https://doi.org/10.1016/j.expthermflusci.2015.03.029

Publications and contribution to conferences

Publications in peer-reviewed journals

- P. Ackermann, H. Münch, and T. Halfmann
  Resonantly-enhanced harmonic generation in Argon
  Optics Express **20** (13) 13824 (2012)
- P. Ackermann, A. Scharf, and T. Halfmann
  Strong quantum interferences in frequency up-conversion towards short vacuum-ultraviolet radiation pulses
  Physical Review A **89**, 063804 (2014)
- P. Ackermann, X. Laforgue, M. Hilbig, M. Schilder, and T. Halfmann
  Phase- matched harmonic generation in gas-filled waveguides in the vicinity of a multiphoton resonance
  Journal of the Optical Society of America B **35** (2) 468 (2018)

Talks at national and international conferences

- P. Ackermann, A. Scharf, and T. Halfmann
  Strong quantum interferences in frequency conversion
  Workshop on Control of Quantum Dynamics of Atoms, Molecules and Ensembles by Light (CAMEL 9) - Nessebar (Bulgaria) 2013
- P. Ackermann, and T. Halfmann
  Strong quantum interferences in frequency conversion towards short vacuum-ultraviolet radiation pulses
  Frühjahrstagung der Deutschen Physikalischen Gesellschaft – Heidelberg (Germany) 2015
- P. Ackermann
  Strong quantum interferences in frequency conversion towards short vacuum-ultraviolet radiation pulses
  Basic concepts of high-intensity light-matter interactions (HICONO summer school 2016) - Darmstadt (Germany) 2016

Posters at national and international conferences

- P. Ackermann, and T. Halfmann
  Quantum Interference in frequency conversion towards ultra-short vacuum-ultraviolet light pulses
  High harmonic spectroscopy (523. WE Heraeus-Seminar) - Bad Honnef (Germany) 2013

Supervisions and contributions to teaching

Master Thesis

[M1] Alexander Scharf, *Kohärente Kontrolle der Frequenzkonversion zu ultrakurzen vakuum-ultravioletten Laserpulsen,* Technische Universität Darmstadt, 2012

[M2] Jan Bachmann, *Aufbau eines Puls-Chirpers für ultraschnelle kohärente Anregungen,* Technische Universität Darmstadt, 2013

[M3] Nico Neumann, *Untersuchungen zur adiabatischen Frequenzkonversion in den XUV Spektralbereich,* Technische Universität Darmstadt, 2014

[M4] Maximilian Schilder, *Aufbau eines Hohlkern-Wellenleiters zur Frequenzkonversion ultrakurzer Laserpulse in Edelgasen,* Technische Universität Darmstadt, 2015

[M5] Fabian Cipura, *Regenerative Verstärkung von gechirpten ps-Laserpulsen,* Technische Universität Darmstadt, 2016

[M6] Mario Hilbig, *Optimierung der Frequenzkonversion ultrakurzer Laserpulse in gasgefüllten Hohlkernwellenleitern*, Technische Universität Darmstadt[14] / Hochschule Rhein-Main

Bachelor Thesis

[B1] Ann-Kathrin Gansmann, *Vermessung dünner transparenter Schichten mit chromatisch konfokaler Weißlichtmikroskopie,* Technische Universität Darmstadt, 2012

[B2] Maximilian Schilder, *Aufbau eines chromatisch-konfokalen Mikroskops mit Mehrfach-Punktabbildung,* Technische Universität Darmstadt, 2013

[B3] Thomas Albrecht, *Aufbau eines Dreikanal-Autokorrelators für ps-Laserpulse,* Technische Universität Darmstadt, 2014

[B4] Fabian Cipura, *Nichtlineare Spektroskopie von Stark-Verschiebungen an Mehrphotonen-Übergängen in Xenon*, Technische Universität Darmstadt, 2014

[14] Laboratory and experimental supervisor

[B5] Sören Link, *Charakterisierung von Pikosekunden-Laserpulsen mit Hilfe eines FROG-Algorithmus,* Technische Universität Darmstadt, 2015

Internships and laboratory courses

- Supervision of laboratory internships “Miniforschung”:
  - Maximilian Schilder, *Vermessung ultrakurzer Laserpulse mit einem Autokorrelator,* Technische Universität Darmstadt, 2013
  - Christian Klos, *Erzeugung und Charakterisierung eines supergaußschen Laserfokus,* Technische Universität Darmstadt, 2013
  - Thomas Albrecht, *Entwicklung eines rauscharmen Photodetektors für schwache Autokorrelationssignale*, Technische Universität Darmstadt, 2014
- Supervision of the advanced lab course “Laser-Resonator” (10/2012 - 9/2015)

Contributions to teaching

- Supervision of student exercises: *Experimentalphysik I* (10/2015 - 3/2016)
- Supervision of student seminar presentations:
  - “Messung ultra-kurzer (ps, fs) Laserpulse” (2012)
  - “Erzeugung höchst-intensiver, ultra-kurzer Lichtpulse ” (2015)

Acknowledgments

Thomas, schon in meiner ersten Vorlesung bei dir, könntest du mich durch deine Begeisterung für die nichtlineare Optik und Quantenoptik und deinem Engagement mitreißen. Schon während meiner Bachelor- und Master-Arbeit war deine Tür immer offen, dein Interesse und die wissenschaftliche Diskussion sehr motivierend. Ich danke dir für dein Vertrauen, die Unterstützung und die angenehme Atmosphäre in einem tollen Team. Ich wünsche dir für die Zukunft nur das Beste!

Professor Walther, ich danke Ihnen für die Übernahme des Zweitgutachtens für meine Dissertation. In freundlichen und unkomplizierten Gesprächen fand sich selbst im prall gefüllten Terminkalender am Ende des Semesters noch die Möglichkeit für die Erstellung des Gutachtens und die Prüfung. Für Ihr Interesse an meiner Arbeit bedanke ich mich herzlich!

Bruce, Leonid and Nikolay, I appreciate fruitful discussions and valuable advise of all of you. In several "theory summers" we concerned several aspects of my work. You, **Leonid**, often put my explanations and results to a hard test. This gently pushed my towards realizing important connections in the theoretical description of laser atom interaction. Together with **Bruce**'s and **Nicolay**'s comprehensive and intuitive framework of quantum optics, it was a joy to gather exciting new insights even beyond my work. Thank you for your support and interest. It was a pleasure meeting all of you.

Xavier, on the last project of my PhD we teamed up to understand the manifold of interesting effects occurring in a tiny glass tube. I thank you for the important contribution of the numeric code, that enabled multi-mode, multi-color propagation for my waveguide model. Especially for your patience to include more and more parameters that we identified as important, But also for the introduction in Matlab's different universe. As a colleague I appreciated your company, fruitful theoretical discussions and funny private conversations.

The ultrafast buddies, ohne euch wäre es ziemlich einsam im Labor. Es war großartig, mit motivierten, interessierten und netten Menschen arbeiten zu dürfen. Die Diskussion mit euch und die Gemeinschaft haben mich bei der Lösung von vielen Problemen unterstützt und über so manchen Rückschlag hinweg getragen. **Holger**, dir möchte ich vor allem für die Betreuung meiner Bachelor- und Master-Arbeit danken. Zusammen mit Thomas hast mir die Grundfertigkeiten beigebracht, die diese Arbeit erst ermöglicht haben. Dir, **Uwe**, danke ich für die Betreuung in der Schreibphase meiner Masterarbeit und die darauffolgende Zeit

als stets gutgelaunter Kollege. **Christian**, nicht nur mit den “schnelleren” Pulsen, sondern auch mit deinem “ultrafast appetite” warst du sowohl im Labor, als auch mir gegenüber am Schreibtisch stets für “Hirnbetankung” in Form von diversen Leckereien zu haben, bei denen nicht selten durch einen anderen Blickwinkel auch eine neue Idee entstand. Auch im Labor war mit dir “immer was los”. **Jan Frederik,** auch deine Gesellschaft habe ich sehr geschätzt. Du bereicherst das Labor nicht nur mit deiner freundlichen, aber zurückhaltenden Art, sondern hast unser Spektrum zudem mit den untersten beiden Oktaven der Laserfrequenz komplettiert. Für deine Arbeit mit dem mid-IR wünsche ich dir alles Gute! **Fabian**, “the ultrafast runner”, schon als Bachelor- und Master-Student durfte ich in dir einen stets motivierten und wissbegierigen Menschen kennen und schätzen lernen. Ich bin glücklich, dass du mein “Erbe angenommen hast” und das ps-Projekt so erfolgreich weiterführst. Für deine warmherzige aber ehrliche Art und dein stets offenes Ohr als kompetenter Kollege in den letzten zwei Jahren danke ich dir herzlich. Ich hoffe, dass unser Lasersystem dir weiterhin gute Dienste leistet und “die Diva” dir stets wohlgesonnen ist.

Kaloyan, I enjoyed your hospitality and found your interest and motivation quite stimulating. Our scientific discussions and the personal chat with a loving father passionate tinker enriched my experience. All the best for you and your family.

Mein besonderer Dank gilt meinen **Miniforschern, Bachelor- und Master-Studenten**. Eure Arbeit ist Grundlage für diese Dissertation. Ich war froh, euch bei den ersten Experimenten unterstützen zu dürfen und mit euch zusammen als Team zu Lernen und zu Wachsen. Ich ich bin glücklich und dankbar über jedes einzele kleine Puzzlestück (materiell und ideell), das Ihr mir zum Erreichen des großen Ganzen hinterlassen habt, aber auch für die stets gute und motivierte Stimmung im ps-Team. Einige von euch durfte ich sogar auf meherern Stationen Ihres Studiums begleiten. Eure Treue bedeutet mir viel und ich wünsche euch allen nur das Beste auf eurem weiteren Lebensweg.

Die Arbeitsgruppe Halfmann werde ich noch lange in guter Erinnerung behalten. Nicht nur die tägliche Runde am Kaffetisch, sondern auch die Gruppenausflüge und Aktivitäten mit einem tollen Team haben die letzten Jahre zu einer wunderbaren Zeit gemacht.
Neben den Master- und Bachelor-Studenten möchte ich hier insbesondere **Thorsten**, **Genko** und den Mitdoktoranden **Marcel**, **Thomas** und **Alexander**, sowie den “ehemaligen” **Frank**, **Simon** und **Daniel**, **Georg, Fabian** und **Lachezar** danken. Als gute Seele der AG möchte ich auch **Damaris**, nicht vergessen. Ohne dich würde nicht einmal der kleinste Spiegel im Labor ankommen oder wir überhaupt ins Labor hinein kommen würden. Auch die privaten Gespräche und deine Gartenpartys habe ich sehr genossen. Zwar oft im Hintergrund aber immer da - Vielen Dank.

Selbst die besten Ideen sind nichts ohne eine handwerkliche Umsetzung. An

dieser Stelle möchte ich dem gesamten **Team der Feinmechanischen Werkstatt** unter Leitung von **Herrn Weick** für eine tolle Umsetzung meiner anspruchsvollen Konstruktionsprojekte und viele lehrreiche Einblicke in die Welt der Feinmechanik danken. Besonders **Herrn Jeretzki** bewundere ich für seine Ideen und sein Engangement immer noch ein Quäntchen mehr Genauigkeit herauszuquetschen als eigentlich möglich. Auch dem **Team der E-Werkstatt** habe ich die ein oder andere Spezialanfertigung und Wiederbelebung eines wichitgen Gerätes zu verdanken.

Nicht vergessen möchte ich auch die Laserbearbeitung und Tests im Target-Labor der **AG Laser- und Plasmaphysik** (Danke **Nico**, **Thorsten** und **Gabriel**), und im **FabLab Darmstadt**.

Liebe **Freunde**, bei Sport, Urlaub und Musik, aber auch den einfachen, gemeinsamen Stunden mit euch konnte ich immer Entspannung, Glück und Rückhalt finden. Dieser Ausgleich ist unentbehrlich für mich und damit für das Zustandekommen dieser Arbeit.

Liebe **Familie**, ohne eure Unterstützung und Motivation und Verständnis auch in schwierigen Zeiten wäre ich nicht dort, wo ich heute stehe - und doch liebt ihr mich nicht für das, was ich bin, sondern als der, der ich bin. Dafür danke ich euch, **Andrea**, **Klaus**, **Cora** und **Katrin** von ganzem Herzen.

Patric Ackermann

Fischbachtal, im Januar 2019